Connecting the esophagus to the brain – examining the role of Prox2 and Runx3 vagal sensory neurons in swallowing

A dissertation

submitted in partial fulfilment of the requirements for the degree of

Doctor rerum naturalium (Dr. rer. nat.)

submitted to the Department of Biology, Chemistry, Pharmacy

of Freie Universität Berlin

by

ELIJAH DAVID LOWENSTEIN

Berlin, 2023

The following work was carried out in the research group of Carmen Birchmeier between November 2016 and December 2022 at the Max Delbrück Center for Molecular Medicine in the Helmholtz Association in Berlin.

1st reviewer:	Prof. Dr. Carmen Birchmeier Department of Disorders of the Nervous System Max-Delbrück Center for Molecular Medicine Berlin
2nd reviewer:	Prof. Dr. Robin Hiesinger Institute of Biology, Neurobiology Freie Universität Berlin
Defense date:	15.02.2023

Declaration of Independence

I hereby declare that I wrote my dissertation independently, and did not use any resources or receive any help other than what is stated herein.

Dedication

To my favorite people Sarah and Effie.

Acknowledgements

I would like to first thank Prof. Dr. Carmen Birchmeier for giving me the opportunity to pursue my PhD in her laboratory and allowing me to tackle this exciting and challenging project. I would also like to thank my thesis committee members Prof. Dr. Gary Lewin and Dr. Niccolò Zampieri for their support and scientific discussions. In particular I would like to thank Niccolò for allowing me to join his lab meetings and giving me support during my postdoctoral search. I also want to thank Prof. Dr. Robin Hiesinger for being my thesis advisor and evaluating my thesis.

I am incredibly indebted to many fantastic lab members that taught me so much in the lab, but also how to think critically and move a project forward. Thank you Prof. Dr. Fritz Rathjen, for being my Saturday morning lab buddy, laughing about the "novelty", "mechanisms" and "descriptive nature" of our experiments, and discussing all aspects of science from what constitutes a proper control to why reviewer #2 is always a pain. I am grateful for the time we shared together! I am also grateful to have learned under two fantastic postdocs in the lab: Dr. Luis Hernandez-Miranda and Dr. Pierre-Louis Ruffault. Luis trained me from when I barely knew how to hold a pipette as a new master's student and took me under his wing teaching me how to do everything from dissections to putting figures together with photoshop. Muchisimas gracias por todo! Tu paciencia y apoyo me han convertido en el científico que soy hoy en día, y no hubiera logrado nada de todo lo que hice sin ti. Pierre-Louis has the amazing quality of being able to read a protocol from a paper as he gets in to the lab and get it up and running before lunch. I hope that at least some of your curiosity and inventiveness has rubbed off on me! You always had time for a coffee, a walk around campus or a midday pep talk and brightened my days.

Dr. Lever, when I first walked into your lab at the University of Missouri, I did not know what to expect. But I definitely did not expect to meet one of the most kind and supportive mentors

that I've had during my short scientific career. Thank you for your endless energy and infectious enthusiasm, for going after the tough questions and never taking no as an answer. It was truly a joy to spend those two months in your lab together with Kate and Rebecca!

I also learned a lot by watching Dr. Minchul Kim and Dr. Kun Song. Thanks for always having time to answer my questions, talk me through your latest experiments and sharing your journeys with me! You both blazed a trail that made my path a little easier.

Where would I be without my MDC Lunch crew? To Lena, Stephan and Xun – you all made my time here so much brighter. From all of the highs and lows, the lunches and the coffees, the gossips, the bets and the laughs, it wouldn't have been the same without you! I'm happy that we all got to work together, from chromosomes to lightsheet and liver histology, but I'm happier still for the times we shared together.

The mark of a great teacher is one who can take a difficult topic and explain it to you in a way that makes sense. Aristotelis – thank you for your endless patience with my incessant bioinformatics questions, and for giving me some semblance of comfort around computational data. I'll always remember our first official meeting as collaborators (what are *you* doing here??), and remain convinced that the best collaborations are between friends.

I would also like to thank two amazing technicians in the lab, Sven Buchert and Bettina Brandt, and our great animal caretaker, Petra Stallerow, for all their help and putting up with my German (or lack thereof). I also enjoyed sharing an office for these last years with Dr. Thomas Müller, who was always happy to lend his critical eye to an experiment or text.

Dime con quién andas, y te diré quién eres. I'm beyond grateful to have found such an amazing group of friends during my time in Berlin. Dr. Maarten Rikken – from that first German class to today, what a ride the past eight years have been. Although we will always have our

differences (kindle vs. paperback), I'm happier for all that we shared, from boxing to cycling, and watching your beloved Socceroos lose to the Albiceleste. To my GOATs Hany and Bence, I wouldn't trade the weekends we spent together for anything! From basketball games, to coffee dates, international adventures, Altered Soul Experiment(s), marriages (three of them), and births (two of them!). So grateful to have you three superstars in my corner.

Me gustaría agradecer a mis padres, María y Pedro, por todo su apoyo y amor. No sé si puedo hacerle justicia a todo lo que me han dado durante estos años – los aprecio un montón! Tengo muchísima suerte de tenerlos a ustedes como padres, quién más podría entender tan íntimamente lo que es hacer un doctorado y apoyarme justo tal y cómo lo necesitaba.

To Sarah – thank you for everything. I couldn't have done it without your constant love and support!

Table of Contents

List of Figures

List of Tables

Abbreviations

3D	Three-dimensional
AP	Area postrema
Asic1	Acid Sensing Ion Channel Subunit 1
Asic2	Acid Sensing Ion Channel Subunit 2
ATP	Adenosine triphosphate
AVI	Audio video interleaved
BSA	Bovine serum albumin
C	Celsius
c-Fos	Fos Proto-Oncogene, AP-1 Transcription Factor Subunit
c-Kit	KIT Proto-Oncogene, Receptor Tyrosine Kinase
Calca	Calcitonin Related Polypeptide Alpha
CCK	Cholecystokinin
CEL-Seq2	Cell Expression by Linear amplification and Sequencing
ChAT	Choline acetyltransferase
Ck8	Keratin 8
CRISPR	Clustered regularly interspaced short palindromic repeats
CTb	Cholera toxin B subunit
CUBIC	Clear, Unobstructed Brain/Body Imaging Cocktails
Cy	Cyanin
DAPI	4′,6-diamidino-2-phenylindole
DCC	Deleted In Colorectal Carcinoma
DMV	Dorsal motor nucleus of the vagus
DT	Diphtheria toxin
DTR	Diphtheria toxin receptor
DTT	Dithiothreitol
E	Embryonic day
EDTA	Ethylenediaminetetraacetic acid
ENS	Enteric nervous system
ErbB	Epidermal growth factor receptor

Eya1	Eyes Absent Homolog 1
FACS	Fluorescently activated cell sorting
FHS	Fetal horse serum
FlpO	Flippase optimized
Fw	Forward
Gabra1	Gamma-aminobutyric acid type A receptor subunit alpha1
GDNF	Glial Cell Derived Neurotrophic Factor
Gfrα1	GDNF family receptor alpha-1
GLP1	Glucagon-like peptide-1
Glp1r	Glucagon-like peptide-1 receptor
Gpr65	G protein-coupled receptor 65
Grm5	Glutamate Metabotropic Receptor 5
HBEGF	Heparin Binding EGF Like Growth Factor
HF	High fidelity
HRP	Horseradish peroxidase
Hz	Hertz
ICC	Interstitial Cell of Cajal
IGLE	Intraganglionic laminar ending
IMA	Intramuscular array
Kcnk2	Potassium Two Pore Domain Channel Subfamily K Member 2
MC	Meta-analysis chemosensory-like subtype
MJ	Meta-analysis jugular subtype
MM	Meta-analysis mechanosensory-like subtype
NA	Nucleus ambiguus
nGFP	Nuclear green fluorescent protein
Nos	Nitric Oxide Synthase
NPW	Neuropeptide W
Npy2r	Neuropeptide Y Receptor Y2
Nrg1	Neuregulin 1
NTS	Nucleus of the solitary tract

ON	Overnight
Oxtr	Oxytocin receptor
P	Postnatal day
PBS	Phosphate-buffered saline
PBX	Phosphate-buffered saline with triton x-100
PCR	Polymerase chain reaction
PFA	Paraformaldehyde
Phox2a	Paired Like Homeobox 2A
Phox2b	Paired Like Homeobox 2B
Piezo2	Piezo Type Mechanosensitive Ion Channel Component 2
Pou3f1	POU Class 3 Homeobox 1
Prox2	Prospero Homeobox 2
Prrxl1	Dorsal Root Ganglia Homeobox
PYY	Peptide YY
Rbp4	Retinol Binding Protein 4
RNA	Ribonucleic acid
Robo	Roundabout Guidance Receptor
RPM	Revolutions per minute
Runx3	Runt-Related Transcription Factor 3
Rv	Reverse
scRNA-seq	Single cell ribonucleic acid sequencing
SDS	Sodium dodecyl sulfate
Six1	Sine oculis homeobox homolog 1
Slit2	Slit Guidance Ligand 2
smFISH	Single molecule fluorescent in situ hybridization
SSII	SuperScript II Reverse Transcriptase
TH	Tyrosine hydroxylase
TrkB	Tyrosine receptor kinase B
Trpv1	Transient receptor potential cation channel subfamily V member 1
TSA	Tyramide Signal Amplification

UMAP	Uniform manifold and projection
UMI	Unique molecular identifier
Uts2b	Urotensin 2B
VFSS	Videofluoroscopy swallow study
VGlut2	Vesicular glutamate transporter 2
Vip	Vasoactive Intestinal Peptide
Wnt	Wingless-Type MMTV Integration Site Family
WT	Wild type

Summary

Sensory neurons of the vagus nerve monitor distention, stretch and nutrients in the gastrointestinal tract, and major efforts are underway to assign physiological functions to the many distinct subtypes of vagal sensory neurons. Here, we used genetically guided anatomical tracing, optogenetics and electrophysiology to identify and characterize three vagal sensory neuronal subtypes expressing Prox2 and Runx3 in mice. We show that these neuronal subtypes function as putative mechanoreceptors. They innervate the esophagus and stomach where they display regionalized innervation patterns, as well as other organs. The electrophysiological analysis of Prox2/Runx3 neurons innervating the esophagus showed that they are all low threshold mechanoreceptors, but possess different adaptation properties. Lastly, genetic ablation of Prox2 and Runx3 neurons demonstrated their essential roles for esophageal peristalsis and swallowing in freely behaving mice. Our work reveals the identity and function of the vagal neurons that provide mechanosensory feedback from the esophagus to the brain, and might lead to better understanding and treatment of esophageal motility disorders.

Zusammenfassung

Sensorische Neurone des Nervus vagus kontrollieren unter anderem in vielfältiger Weise die Motilität des Ösophagus und des Magen-Darm-Traktes. Ziel gegenwärtiger neurobiologischer Forschung ist es, den Subpopulationen im Ganglion nodosum, das neben dem Ganglion jugulare die sensorischen Zellkörper des Nervus vagus enthält, spezifische physiologische Funktionen zu zuweisen. In dieser Arbeit haben wir mittels genetischer Techniken, anatomischer Markierungen, Optogenetik, und Elektrophysiologie, drei sensorische Subtypen, die die Transkriptionsfaktoren Prox2 und Runx3 exprimieren, in der Maus charakterisiert. Wir zeigen, dass diese neuronalen Subtypen als Mechanorezeptoren fungieren. Sie innervieren die Speiseröhre und den Magen, sowie andere Organe, in denen sie spezifische Innervationsmuster aufweisen. Die elektrophysiologische Analyse von Prox2/Runx3-positiven Neuronen, die den Ösophagus innervieren, zeigte, dass es sich um niederschwellige Mechanorezeptoren mit unterschiedlichen Anpassungseigenschaften handelt. Schließlich zeigte die genetische Ablation, dass Prox2- und Runx3-positive Neurone eine zentrale Rolle in der Ösophagus-Peristaltik und bei dem Schlucken in frei-beweglichen Mäusen spielen. Zusammenfassend lässt sich feststellen, dass durch unsere Arbeit die Identität und Funktion von vagalen neuronalen Subpopulationen, die eine

mechanosensorische Rückkopplung der Speiseröhre zum Gehirn ermöglichen, charakterisiert wurde. Unsere Ergebnisse könnte somit zu einem besseren Verständnis von Motilitätsstörungen der Speiserohre beitragen.

1. Introduction

While all animals exist in, and interact with their external environment, they must also maintain homeostasis within their internal environment to ensure their survival. These interactions between an animal and its environment are orchestrated by the nervous system. The peripheral nervous system, which includes all neurons found outside of the brain and spinal cord, can be divided broadly speaking into sensory and motor nerves (Bear et al., 2015; Kandel et al., 2013). The somatosensory system senses the external world through specialized nerve endings in the skin, passing conscious information about temperature, texture and pain centrally through the spinal cord to the brain (Koch et al., 2018). On the other hand, the viscerosensory system is responsible for sensing an animal's internal world. Viscerosensory, or interoceptive, neurons located largely in the vagal ganglia innervate all major organ systems, including the cardiovascular, respiratory and digestive organs, where they sense diverse stimuli such as metabolites, mechanical stretch, pH, pathogens and temperature (Janig, 1996; Prescott and Liberles, 2022; Undem and Weinreich, 2005). Somato- and viscerosensory information is processed centrally, where motor output generates movement both externally as the animal moves towards a mate or away from a predator, and internally as the digestive tract mechanically breaks down food and the lungs expand and contract.

Viscerosensory neurons are pseudounipolar, with one arm coursing along the vagus nerve to innervate distal organ targets, while the other projects centrally to second order sensory neurons residing in the nucleus of the solitary tract in the hindbrain (Prescott and Liberles, 2022; Undem and Weinreich, 2005). Nucleus of the solitary tract neurons in turn project to vagal motor efferents located in two parasympathetic hindbrain nuclei, the dorsal motor nucleus of the vagus and the nucleus ambiguus, which form the descending vagal motor output necessary to maintain bodily homeostasis (Travagli et al., 2006). Most research concerning the sensory nervous system deals with somatosensation, or the conscious sensations arising from the external world. Due to the low numbers and vast heterogeneity of interoceptive neurons, their study lagged behind that of their somatosensory counterparts (Prescott and Liberles, 2022). The exact molecular identity and function of many interoceptive neurons that maintain bodily homeostasis remains unclear.

1.1. Vagal neuron anatomy

The peripheral nervous system contains 12 pairs of cranial nerves, some of which are purely motor (III, IV, VI, XII), purely sensory (I, II, VIII), or contain both motor and sensory fibers (V, VII, IX, X, XI) (Cordes, 2001; Guthrie, 2007). Viscerosensory neurons in the geniculate, petrose and nodose ganglia send projections to diverse targets in the periphery through the facial (VII), glossopharyngeal (IX) and vagal (X) nerves, respectively (Vermeiren et al., 2020). The Xth cranial nerve is also known as the vagus nerve, which in latin means wandering and describes the meandering path that the longest cranial nerve takes as it innervates all the major organ systems (Figure 1) (Prescott and Liberles, 2022; Undem and Weinreich, 2005).

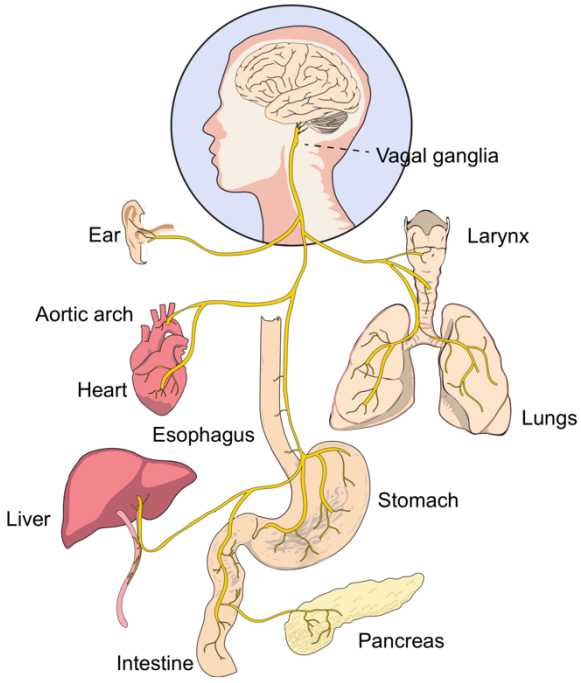

Figure 1. The vagus nerve innervates all major organ systems. Adapted from (Prescott and Liberles, 2022).

In mice, the viscerosensory nodose ganglia, also known as the inferior vagal ganglia, sits outside the jugular foramen where they are fused with the sensory jugular ganglia, also known as the superior vagal ganglia (Han and de Araujo, 2021; Haring et al., 2020). Neurons in the inferior vagal are pseudounipolar, extending a single axon that bifurcates and projects both to distant targets in the periphery as well as to the nucleus of the solitary tract (NTS) in the hindbrain (Undem and Weinreich, 2005). The vagus nerve mostly carries sensory afferents from the inferior and superior vagal ganglia, although 20% of the fibers are motor efferents from two parasympathetic

brainstem nuclei located in the medulla, the dorsal motor nucleus of the vagus (DMV) and the nucleus ambiguus (NA) (Prechtl and Powley, 1990).

First order vagal sensory neurons sense distinct modalities in the periphery, and transmit this information to second order sensory neurons in the NTS. These neurons participate in simple reflexes, and in turn project to preganglionic motor neurons in the DMV and NA that send instructions to motor neurons embedded in the viscera that control autonomic functions (Kubin et al., 2006; Powley, 2021; Travagli and Anselmi, 2016; Travagli *et al.*, 2006). These minimum reflex circuits additionally pass information to and are impinged upon by higher order brain regions such as the hypothalamus (Browning and Travagli, 2014; Rinaman, 2010).

In mice the bilateral vagal ganglia consist of approximately 10,000 neurons (5,000 per vagal ganglion), and innervate the respiratory, cardiovascular and digestive systems (Ichikawa et al., 2006; Mazzone and Undem, 2016; Prescott and Liberles, 2022; Zhao et al., 2022). In addition to neurons, the vagal ganglia contain glial cells, including satellite glia, non-myelinating and myelinating Schwann cells, and endothelial and immune cells (Kupari et al., 2019; Waise et al., 2018). All of these resident cell types must work in concert for vagal neurons to be able to undertake their key bodily functions. Mice only have one pair of viscerosensory vagal ganglia, compared to the 31 pairs of somatosensory spinal afferents located in the dorsal root ganglia. The extremely low number of vagal neurons is buttressed by their incredible heterogeneity. Recent single cell RNA sequencing (scRNA-seq) studies have uncovered around 30 vagal neuron transcriptomic subtypes with between 20-200 neurons per subtype (Bai et al., 2019; Buchanan et al., 2022; Kupari *et al.*, 2019; Liu et al., 2021; Prescott et al., 2020; Zhao *et al.*, 2022). Thus, specific viscerosensory modalities may be mediated by an extremely small number of neurons innervating a particular organ. What the viscerosensory system lacks in sheer numbers, it more than makes up for in the immense diversity of cell types. Although the function of a few molecular vagal subtypes has been uncovered, the physiological roles of the vast majority of subtypes are still unknown.

1.2. Vagal neuron development

While both glial and neuronal cells in most sensory ganglia, including the somatosensory dorsal root ganglia and jugular ganglia, derive from the neural crest, glial cells and neurons in the nodose ganglia have distinct embryonic origins (Rao and Jacobson, 2005; Undem and Weinreich,

2005). Nodose glial cells derive from the cranial neural crest while nodose neurons derive from the epibranchial placode (Vermeiren *et al.*, 2020). The differential contributions of the crest and placode were elucidated by a series of seminal quail-chick transplantation studies where isotropic and isochronic grafts of quail crest or placode were transplanted into a chick host (Ayer-Le Lievre and Le Douarin, 1982; D'Amico-Martel and Noden, 1983; Fontaine-Perus et al., 1988; Narayanan and Narayanan, 1980). These quail-chick chimeras were used to follow the cellular derivatives from the grafted quail tissue, which could be distinguished from the resident chick cells (Le Douarin, 1986).

With the advent of molecular biology and the development of genetic lineage tracing, the transcriptional programs necessary for peripheral glial cell and neuron development were uncovered. All peripheral glial cells derive from the neural crest, a transient embryonic cell type that depends on the Wnt signaling pathway for its generation (Dorsky et al., 1998; Jessen and Mirsky, 2005; Kastriti and Adameyko, 2017). Wnt signaling has been implicated in many different stages of neural crest development, from induction of the neural crest to terminal differentiation (Bronner-Fraser, 2002; Garcia-Castro et al., 2002; Ikeya et al., 1997; Lee et al., 2004). The successful differentiation of neural crest cells into the full complement of peripheral glial cells relies on the transcription factor *Sox10*, whose ablation precludes the generation of Schwann and satellite glial cells (Britsch et al., 2001; Kuhlbrodt et al., 1998).

In contrast to the transcriptional cascade necessary for the generation and maturation of crest-derived cells, placodally-derived neurons depend on a different sequence of gene expression (Begbie et al., 2002; Schlosser, 2006; Vermeiren *et al.*, 2020). Placodal progenitors, which generate nodose neurons, depend on the homeobox transcription factor *Six1*, and its upstream transcriptional co-activator *Eya1* (Zou et al., 2004). Neurogenesis in the epibranchial placode was completely abrogated by the mutation of *Eya1*, while the mutation of *Six1* markedly reduced neurogenesis. Mutation of these genes in placodal epibranchial progenitors precludes the correct expression of *Neurogenin1/2*, *Phox2a* and *Phox2b,* which are critical determinants of nodose neuron development and maintenance (Zou *et al.*, 2004). While nodose ganglia are reduced in size in *Neurogenin1* and *Neurogenin2* mutants, they are completely absent in *Neurogenin1/2* knockouts. This suggests that *Neurogenin1 and Neurogenin2* can at least partly rescue the function of the other, and play somewhat redundant roles in nodose neuron development (Fode et al., 1998; Ma et al., 1998).

The related homeobox transcription factors *Phox2a* and *Phox2b* are necessary for the development and maintenance of the autonomic nervous system, including cranial sensory, sympathetic, parasympathetic and enteric neurons (Morin et al., 1997; Pattyn et al., 1997; 1999). *Phox2a* is expressed in the epibranchial placodes, delaminating neuroblasts and the newly formed nodose ganglia, although its expression decreases shortly thereafter (Morin *et al.*, 1997). In contrast, *Phox2b* expression is initiated in neurons as the nodose ganglia are being formed, and its expression is maintained throughout life (Pattyn *et al.*, 1999). While the mutation of *Phox2a* causes a massive reduction in the number of nodose neurons, the mutation of *Phox2b* causes a fate shift, and viscerosensory nodose neurons adopt a more somatosensory fate (D'Autreaux et al., 2011; Morin *et al.*, 1997).

Although the transcriptional cascade described above applies broadly to nodose neurons, the exact developmental programs that give rise to specific subtypes of nodose neurons are unknown. Recent work has used scRNA-seq to show that the major somatosensory neuronal types of the dorsal root ganglia arise from a series of bi-potent intermediate states, whereby neurons express first competing fate programs before choosing a cell fate (Faure et al., 2020; Soldatov et al., 2019). The development of subtypes of nodose neuron is almost completely unknown, but it is tempting to hypothesize that they might also form via bi-potent intermediates.

1.2.1. Development of the enteric nervous system

The enteric nervous system (ENS) populates the entire rostro-caudal axis of the digestive tract from the esophagus to the colon with resident sensory, motor and interneurons (Spencer and Hu, 2020). The ENS begins to develop from E9.5 in mice, and derives from both the cervical and sacral neural crest, as well as from Schwann cell precursors, i.e. neural-crest like cells that migrate along developing axonal tracts (Espinosa-Medina et al., 2017; Uesaka et al., 2016). The neural crest and Schwann cell precursors colonize the digestive tract in a rostral to caudal manner, first populating the myenteric ganglia, and by E14.5 Phox2b+ enteric progenitors have reached the entire gut (Niu et al., 2020; Uesaka *et al.*, 2016). A few days after settling in the myenteric ganglia, some cells migrate radially to form the submucosal ganglia. The arrival and differentiation of enteric neurons depends on transcription factors such as *Phox2a* and *Phox2b*, as well as ErbB/Nrg1 and Gfrα1/GDNF signaling, among others (Espinosa-Medina *et al.*, 2017; Uesaka *et al.*, 2016). The ENS continues to differentiate and expand until ~P21, although a recent study claims that

there is a rapid turnover rate of enteric neurons and that neurogenesis in the ENS persists throughout life (Kulkarni et al., 2017).

1.2.2. Development of extrinsic vagal innervation of the gastrointestinal tract

Nodose neurons begin to coalesce in the nodose anlage and express *Phox2b* around E9.5 in the mouse (Morin *et al.*, 1997). A recent study mapped the development of nodose innervation of the gastrointestinal tract using *VGlut2^{Cre};R26^{Tomato}* mice and whole mount immunohistology (Niu *et al.*, 2020). They found that by E10.5 axons had entered the esophagus, by E11.5 they reached the stomach, by E12.5 they had split into two branches: a gastric branch that continued innervating the stomach and a celiac branch that turned to innervate the intestine. By E14.5, the rostral portion of the intestine was innervated, and by E16.5 the entire gastrointestinal tract was innervated by nodose tdTomato+ axons (Niu *et al.*, 2020). This timeline of vagal afferent innervation of the digestive system matched older work performed using histological and tracing techniques (Baetge and Gershon, 1989; Ratcliffe et al., 2006).

It was previously shown that viscerosensory afferents in the head innervate their targets before viscerosensory efferents, and therefore provide an axonal scaffold that is required for parasympathetic efferent innervation (Coppola et al., 2010). Niu and Liu and colleagues wanted to test whether the same heterotypic axonal interactions that are required for proper innervation of the head also occur in the digestive tract. They found that after the ablation of 70% of vagal afferents, gut innervation by parasympathetic efferents arising from the dorsal motor nucleus of the vagus was severly affected. Thus, the nervous system relies on the wiring of afferent neurons to guide efferent neurons, but the mechanisms that guide afferent neurons to their correct targets is still unknown. Many guidance molecules released by enteric neurons, vasculature, and the gut wall are thought to play a role in guiding vagal neurons to their targets in the digestive tract, among them Netrin/DCC, Slit/Robo, Semaphorin/Neuropilin, and neurotrophin/tyrosine kinase receptor (Ratcliffe et al., 2011a; Ratcliffe et al., 2011b; Uesaka *et al.*, 2016). Diffusible morphogens such as retinoic acid and bone morphogenetic proteins may also play a role in guiding vagal afferents to the gut (Ratcliffe *et al.*, 2011b). More work is needed to discover the precise mechanisms by which vagal afferent neurons find their targets in the digestive tract, and how this process goes awry in diseases such as in Hirschsprung's disease.

1.3. Vagal afferent neurons innervating the digestive tract

The vagal afferents that innervate the gastrointestinal tract are not homogenous, but display unique electrophysiological and morphological properties (Brookes et al., 2013). Intraganglionic laminar endings (IGLEs), intramuscular arrays (IMAs) and mucosal endings describe three types of vagal afferents named after their end organ morphologies (Wang et al., 2020). These ending types contact distinct cells within the digestive tract, and recent evidence indicates that subtypes of vagal afferents that innervate the gut possess distinct transcriptomic signatures (Bai *et al.*, 2019; Williams et al., 2016). Gastrointestinal vagal afferents can be chemosensory, mechanosensory, or polymodal and will be discussed in more detail below.

1.3.1. Vagal afferents that innervate the mucosa

Afferents that target the mucosal layer have been detected in the lamina propria of the esophagus, stomach and intestine and are generally thought to be chemosensory or polymodal in nature (Berthoud et al., 2004; Berthoud et al., 1995; Wang *et al.*, 2020; Wank and Neuhuber, 2001). These mucosal afferents have been shown to form direct synaptic contacts with neuropods, a type of enteroendocrine cell that detects sugars and sweeteners in the intestinal lumen (Kaelberer et al., 2020). Enteroendocrine cells in the intestinal epithelium perform most nutrient sensing in the intestine, and can secrete many hormones that modulate the animals metabolic state (via vagus dependent and independent mechanisms) such as CCK, GLP1, Ghrelin, PYY, Orexin A, NPW and Secretin (Waise *et al.*, 2018). Nodose mucosal afferents express metabotropic G protein-coupled receptors that can detect and respond to these hormones (Waise *et al.*, 2018). While sugar drove glutamate release from neuropods, sweetener caused ATP release and thus purinergic neurotransmission to the mucosal afferent. By choosing which neurotransmitter they release neuropods communicate differential information about nutrient contents in the gut to vagal afferents and thus connect the gut to the brain in one synapse (Buchanan *et al.*, 2022; Kaelberer et al., 2018).

Recent efforts have identified numerous molecular subtypes of vagal neurons that innervate the mucosal layer in the digestive tract. For instance, Gpr65+ mucosal afferents were found to innervate villi in the proximal small intestine and respond to infusion of liquid food (Williams *et al.*, 2016; Zhao *et al.*, 2022). Others have found mucosal afferents innervating the non-glandular stomach (Calca+) and small intestine (Vip+, Uts2b+ and Glp1r+) (Bai *et al.*, 2019; Zhao *et al.*,

2022). The optogenetic activation of either Gpr65+ or Vip+ intestinal mucosal afferents had no effect on food intake during a fasting and re-feed test, and the precise roles of these mucosal afferents are still open (Bai *et al.*, 2019). Lastly it should be mentioned that some mucosal afferents have also been shown to respond to gentle mucosal stroking in an *in vitro* preparation, and are thus polymodal (Li et al., 2018; Page and Blackshaw, 1998; Page et al., 2002).

1.3.2. Vagal afferents that innervate the muscle layers

The vagal afferents that end in the muscle layers in the digestive tract terminate either within the longitudinal or circular muscle layers as IMAs or between them as IGLEs (Kim et al., 2022; Mercado-Perez and Beyder, 2022). IMAs form long terminal arrays parallel to both the muscle fibers and to interstial cells of Cajal (ICCs) (Figure 2) (Powley et al., 2016; Powley and Phillips, 2011; Powley et al., 2008). ICCs are mesenchymal cells that function as pacemakers to drive gut motility (Sanders et al., 2006; Sanders and Ward, 2006). They also form gap junctions with smooth muscle cells and make synaptic contacts with IMAs, thus creating a functional connection between the smooth muscle of the gastrointestinal tract and the nervous system (Powley *et al.*, 2008).

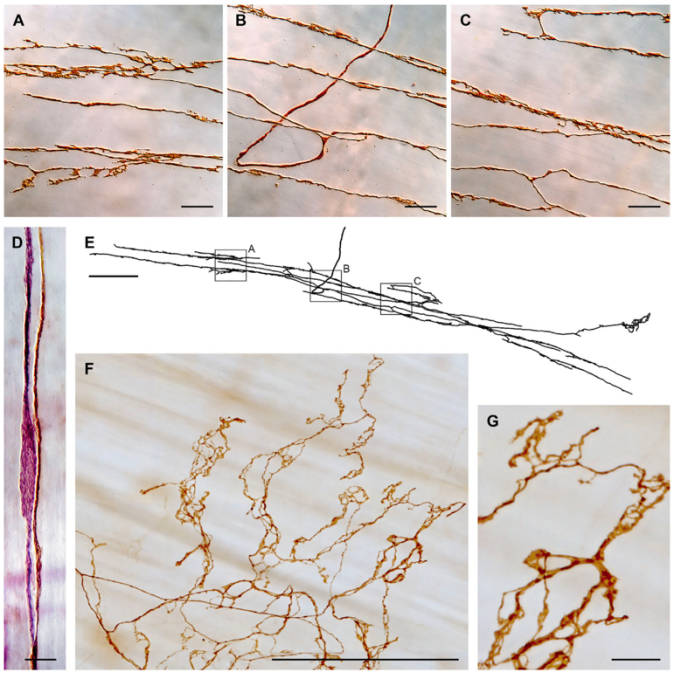

Figure 2. Intramuscular array histology. (A-C) Magnifications of the IMA shown in E. **(D)** IMAs (brown) contact ICCs (purple) in the muscle layer. **(E)** Digital rendering of an IMA. **(F)** 'Web ending' variant of an IMA. **(G)** Magnification of F. Adapted from (Powley et al., 2019).

Fox and colleagues generated a mutant mouse that lacked ICCs and found that IMAs, but not IGLEs, were severely reduced in number, suggesting that ICCs are required for the development and maintenance of IMAs (Fox et al., 2001). IMAs are not found uniformly throughout the digestive tract, but instead densely innervate the sphincter regions, including the lower esophageal sphincter and pyloric sphincter, but can also be found in the non-glandular stomach (Powley et al., 2014; Powley *et al.*, 2016). The complex formed between the vagal IMA and the ICC is organized similar to that of a proprioceptive sensory neuron and a muscle spindle, leading to the hypothesis that vagal IMAs might detect stretch in the muscle wall (Phillips and Powley, 2000; Powley and Phillips, 2011). The molecular identity and physiological role of vagal IMAs that innervate the sphincters and non-glandular stomach is currently unknown. However, esophageal IMAs were defined in recent work as Piezo2+Grm5+Slit2+ neurons that respond to stretch (Zhao *et al.*, 2022).

The second type of vagal afferents that terminate on enteric neurons located between the muscle layers of the digestive tract are IGLEs. They form terminal plates of lamellar puncta and contain leafy structures that intercalate between enteric neurons (Figure 3) (Umans and Liberles, 2018; Wang *et al.*, 2020).

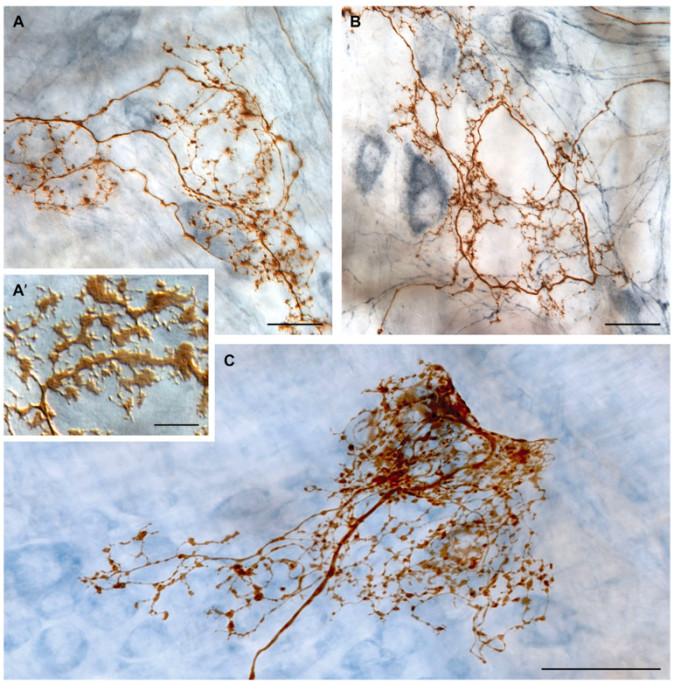

Figure 3. Intraganglionic laminar ending histology. (A-C) Examples of IGLEs showing the typical flattened lamelliform puncta morphology. Adapted from (Powley *et al.*, 2019).

These vagal afferents were first described in the dog esophagus almost 100 years ago (Lawrentjew, 1929; Nonidez, 1946), and were later termed IGLEs by Jose Rodrigo (Rodrigo et al., 1975). Rodrigo examined the esophagus of the cat and found that the main IGLE axon was myelinated, but that the terminal processes that contacted enteric neurons were unmyelinated. Later studies found IGLEs throughout the digestive tract including in the esophagus, but also in the stomach and intestine of many different species (Bai *et al.*, 2019; Kim *et al.*, 2022; Mercado-Perez and Beyder, 2022; Wang *et al.*, 2020; Williams *et al.*, 2016; Zhao *et al.*, 2022). A careful examination of IGLEs throughout the gastrointestinal tract in mice found that they were ubiquitous throughout but decreased in concentration along the rostral to caudal axis (highest concentration found rostrally) (Berthoud and Patterson, 1996; Fox et al., 2000; Zhao *et al.*, 2022). Tracing from single vagal afferent axons suggested that they can terminate in multiple enteric ganglia as IGLEs, and in some rare cases the same parent axon might have distinct end organ morphologies (i.e. the same axon generates both IGLE and IMA endings) (Berthoud and Powley, 1992; Phillips and Powley, 2000). Iggo described IGLEs as "in series tension receptors", a description that is reminiscent of Golgi tendon organs in the skeletal muscle (Iggo, 1955; Phillips and Powley, 2000).

Vagal neurons that form IGLEs, are pseudounipolar vagal afferents, and thus it was a surprise when an electron microscopy study found presynaptic contacts from IGLEs onto enteric neurons (Neuhuber, 1987). Further immunohistological experiments found that VGlut2 and Synaptophysin 1 (presynaptic markers) co-localized together with the IGLE in the rat esophagus (Raab and Neuhuber, 2003). Although IGLEs seem to be presynaptically connected to enteric neurons based on electron microscopy and immunohistological data, electrical stimulation of vagal afferents only elicited limited c-Fos expression in enteric neurons (Zheng et al., 1997). Whether vagal IGLEs also play a local effector role, or communicate with other cell types located in the myenteric plexus, or simply use enteric neurons as a developmental scaffold is an open question.

Due to the vast heterogeneity of vagal sensory neurons, their molecular characteristics were only recently defined with scRNA-seq (Bai *et al.*, 2019; Buchanan *et al.*, 2022; Kupari *et al.*, 2019; Liu *et al.*, 2021; Prescott *et al.*, 2020; Zhao *et al.*, 2022). Further, work over the past few years has begun to characterize the properties of some subtypes of neurons important for digestion using molecular and genetic tools. For example, two subtypes of vagal neurons that form IGLEs contacting intestinal and stomach enteric ganglia express *Oxtr* and *Glp1r*, respectively (Bai *et al.*, 2019; Williams *et al.*, 2016). The activation of Oxtr+ neurons forming intestinal IGLEs potently

inhibits feeding, whereas Glp1r+ neurons that form stomach IGLEs detect stretch (Bai *et al.*, 2019; Williams *et al.*, 2016). The molecular signature and function of neurons that form esophageal IGLEs was unknown. In my thesis, I characterized this vagal neuronal subtype.

1.4. Mechanosensation in the digestive tract

As food and liquid pass through the digestive tract they apply force against, and generate shear forces within, the gut wall. The gut responds not as an inert hollow tube, but in fact generates mechanical forces of its own by actively distending and contracting to physically push the food or liquid bolus through the alimentary canal in a process known as peristalsis (Mercado-Perez and Beyder, 2022). For the proper coordination of digestive behaviors, the nervous system must be able to survey the mechanical state of the gastrointestinal tract (Kim *et al.*, 2022). This is accomplished via a dedicated set of specialized sensory neurons called mechanoreceptors. Although resident enteric neurons and spinal afferents also contain mechanoreceptors, many of these specialized cells are in fact the vagal afferents described in the previous section, namely IMAs and IGLEs (Brookes *et al.*, 2013). Based on their morphology and anatomical location, IMAs have been proposed to detect stretch, while IGLEs detect tension (Phillips and Powley, 2000). Stretch can be defined as the force required for muscle extension, while tension is the force required to maintain muscle length (Phillips and Powley, 2000; Wang *et al.*, 2020). It is technically challenging to separate stretch and tension experimentally, because most *in vitro* or *in vivo* setups will manipulate both of these forces simultaneously.

Mechanosensitive vagal afferents innervating the digestive tract were first recorded in the cat (Paintal, 1954) and the goat (Iggo, 1955). Their vagal nature was determined after vagatomy causes the degeneration and subsequent loss of IGLEs (Castelucci et al., 2003; Rodrigo et al., 1982). As *in vitro* electrophysiological preparations improved it became possible to dissect out the attached esophagus and stomach together with the vagus nerve and perform recordings. These experiments revealed that vagal afferents were largely slowly adapting, low-threshold mechanoreceptors (Page and Blackshaw, 1998; Page *et al.*, 2002). Later experiments combined *in vitro* electrophysiology with morphological analysis to identify the vagal mechanosensory ending. After identifying mechanosensory transduction sites in the guinea pig esophagus, stomach and small intestine researchers applied a dye to the area and found that the labeled sensory endings all displayed IGLE morphology (Tassicker et al., 1999; Zagorodnyuk and Brookes, 2000;

Zagorodnyuk et al., 2001; Zagorodnyuk et al., 2003). Based on the speed with which the vagal fiber responded to the mechanical stimulus, and that the vagal response persisted in spite of blocking synaptic transmission, led to the conclusion that the vagal afferent itself is mechanosensory, and does not rely on the local enteric neurons to detect mechanical information. Although some IGLE subtypes and their functional roles have been described (see Glp1r+ and Oxtr+ IGLEs above in 1.3.2.), the molecular identity and physiological role of esophageal IGLEs is currently unknown.

1.5. The physiological role of vagal mechanosensory afferents in the esophagus

Swallowing (or deglutition) is an active process that transports food and liquid from the mouth to the stomach via the esophagus. The esophageal phase of swallowing requires peristaltic movements of the esophageal wall, which are controlled by reflexes that are executed by vagal motor neurons in the hindbrain (DMV or NA), and the enteric ganglia in the esophagus (Ertekin and Aydogdu, 2003; Goyal and Chaudhury, 2008). Esophageal motility disorders are characterized by dysphagia, and are frequent comorbidities of aging and age-related neurological disease (Aslam and Vaezi, 2013; Aziz et al., 2016; Suttrup and Warnecke, 2016). The etiology underlying dysphagia is mostly unknown, due in large part to the lack of knowledge about the sensorimotor circuits involved (Kloepper et al., 2020). The first studies of esophageal physiology were undertaken in the late 19th century, and for the following decades it was debated whether the activity of hindbrain swallowing centers (i.e. hindbrain vagal motor nuclei and the nucleus of the solitary tract) suffices to generate esophageal peristalsis, or if vagal sensory feedback is also required (Janssens et al., 1976; Jean, 1984; Kronecker H., 1883). Several lines of evidence subsequently demonstrated the importance of peripheral feedback for esophageal function, but the exact vagal subtype that provides this feedback is unknown (Falempin et al., 1986; Frazure et al., 2021; Lang, 2009). Classical studies often relied on blunt dissection of the vagus nerve and therefore affected both sensory and motor vagal fibers. Furthermore, the majority of these studies analyzed swallowing under anesthesia, which is known to affect esophageal peristalsis (Lang, 2009). Deglutition in awake, freely behaving rodents can be observed using videofluoroscopic swallowing studies (VFSS) (Haney et al., 2019; Hinkel et al., 2016; Lever et al., 2015). Thus, ablation of specific vagal sensory neurons that innervate the esophagus, and subsequent analysis

using VFSS, can conclusively demonstrate the extent to which sensory feedback regulates esophageal peristalsis and define the responsible vagal sensory neuronal subtype.

1.6 The physiological role of vagal mechanosensory afferents in the stomach

The stomach can be divided into two parts, based on their anatomy and distinct physiological roles, i.e. the non-glandular and glandular stomach. These portions of the stomach have different functional roles during digestion, with the non-glandular stomach playing a role in gastric accommodation, and the glandular stomach playing a role in gastric emptying (Janssen et al., 2011; Umans and Liberles, 2018). During feeding, the ingested material collects in the non-glandular stomach that acts as a food reservoir and slowly expands in a process known as gastric accommodation (Umans and Liberles, 2018). Tonic contractions in the non-glandular stomach then push the material to the glandular stomach, where it is mixed with juice and subjected to peristaltic contractions that break down the ingested material and push it through the pyloric sphincter (Janssen *et al.*, 2011). Both gastric emptying and accommodation rely on the mechanical distension, stretching and contraction of the stomach wall, and it has been shown that vagotomy alters many aspects of gastric function. Whether these changes can be assigned to vagal afferents or the motor efferents is unclear (Powley, 2021). Recent work discovered that Glp1r+ vagal afferents form stomach IGLEs, and respond to acute stretch such as when the stomach receives a meal (Williams *et al.*, 2016). However, it is known that there is heterogeneity in the responses of Glp1r+ vagal neurons to stomach stretch, raising the possibility of further subtypes of Glp1r+ neurons that perhaps play differential roles in stomach physiology.

2. Aims

i) Define vagal neuron heterogeneity using scRNA-seq.

ii) Generate a novel transgenic mouse strain to further study specific subtypes of vagal sensory neurons.

iii) Use intersectional genetic tools to uncover the projection patterns and physiological roles of specific subtypes of vagal sensory neurons.

3. Materials and Methods

3.1 Mouse lines

All experiments were conducted according to regulations established by the Max Delbrück Centre for Molecular Medicine, LAGeSo (Landesamt für Gesundheit und Soziales), and the institutional animal care and use committee at the University of Missouri. B6.Cg-*Gt(ROSA)26Sor*$^{tm14(CAG-tdTomato)Hze}$/J (referred to as *Ai14,* #007914), B6;129S-*Gt(ROSA)26Sor*$^{tm65.1(CAG-tdTomato)Hze}$/J (referred to as *Ai65,* #021875), B6.Cg-*Gt(ROSA)26Sor*$^{tm80.1(CAG-COP4*L132C/EYFP)Hze}$/J (referred to as *Ai80,* #025109), *Slc17a6*$^{tm2(cre)Lowl}$/J (referred to as *VGlut2*^{Cre}, #016963) mice were obtained from the Jackson Laboratory (Daigle et al., 2018; Madisen et al., 2015; Madisen et al., 2010; Vong et al., 2011). B6D2-Tg(Phox2b-cre)1Jbr/CB (referred to as *Phox2b*^{Cre}, (D'Autreaux *et al.*, 2011)) and *R26*^{FTLG} (Dempsey et al., 2021) mice were provided by Jean-François Brunet (Institut de Biologie de l'ENS, Paris, France). *Mapt*$^{tm1(lacZ,HBEGF/EGFP)Gld}$/CB (referred to as *Tau*$^{ds-DTR}$, (Britz et al., 2015)) mice were a kind gift from Martyn Goulding (Salk Institute, CA, USA). *Runx3*$^{tm6(EGFP/cre)Yg}$/CB (referred to as *Runx3*^{Cre} mice were a kind gift from Yoram Groner (Weizmann Insitute, Rehovot, Israel) (Levanon et al., 2011). *Gt(ROSA)26Sor*$^{tm2.1Sia}$/CB mice were kindly provided by Shinichi Aizawa (RIKEN Center for Developmental Biology, Kobe, Japan); referred to as *R26*^{nGFP} (Abe et al., 2011). *Prox2*^{FlpO} mice were generated as part of this PhD thesis (see Results). Mice were housed at room temperature (23°C), humidity (56%), and with a 12-hour light-dark cycle.

3.2. Genotyping

Tail biopsies were digested in 50 µl of tail lysis buffer (100 mM Tris pH 8.5 (Roth), 5 mM EDTA pH 8 (Roth), 0.2% SDS (Serva), Proteinase K 100 µg/ml (Sigma)) at 55°C overnight (ON). The digestion was terminated the following day by heat inactivating Proteinase K at 95°C for 10 mins. Tail biopsies were diluted with 300 µl Milli-Q H_2O. 1 µl of the diluted tail biopsies was added to the following genotyping mix: 1.5 mM $MgCl_2$, 3.5% DMSO, 0.0935% β-mercaptoethanol, 0.5 mM dNTPs (Invitek), 12.5% sucrose, 0.146% $(NH_4)_2SO_4$, 0.0042% Cresol Red, 4 µM forward primer, 4 µM reverse primer, and 0.22 µl Taq polymerase (Invitrogen) for a total of 20 µl per genotyping reaction. Individual primer sequences and the PCR program can be

found below. The PCR product was loaded on a 1.5% agarose gel with ethidium bromide and electrophoresis was performed at 170 V for 15 minutes. Bands were visualized under a UV lamp.

3.2.1. Primer sequences

Mouse line	Primer	Sequence (5' - 3')	Fragment size (bp)
Ai14	Ai14_Fw	CTGTTCCTGTACGGCATGG	196
	Ai14_Rv	GGCATTAAAGCAGCGTATCC	
Ai65	Ai65_Fw	GCAATAGCATCACAAATTTCAC	190
	Ai65_Rv	TCTAGCTTGGGCTGCAGGT	
Ai80	Ai80_Fw	CGAGTTTAAGAACCCGTCCA	244
	Ai80_Rv	ACCCAGGCAGAAGAAGATGA	
VGlut2^{Cre}	VGlut2^{Cre}_Fw	AAGAAGGTGCGCAAGACG	124
	VGlut2^{Cre}_Rv	ACACCGGCCTTATTCCAAG	
Phox2b^{Cre}	Phox2b^{Cre}_Fw	GGCCGGTCATTTTTATGATC	~300
	Phox2b^{Cre}_Rv	GAAATCAGTGCGTTCGAACGCTAG	
R26^{FTLG}	R26^{FTLG}_Fw	TAAAGTCGACTCGGGGACAC	221
	R26^{FTLG}_Rv	ATAACAACAACGGCGGCTAC	
Tau$^{ds\text{-}DTR}$	Tau$^{ds\text{-}DTR}$_Fw	GTCAGATCACTAGACTCAGCATCC	210
	Tau$^{ds\text{-}DTR}$_Rv	CGGCCTCGACTCTACGATAC	
Runx3^{Cre}	Runx3^{Cre}_Fw	AACATGCTTCATCGTCG	~300
	Runx3^{Cre}_Rv	TTCGGATCATCAGCTACACC	
R26^{nGFP}	R26^{nGFP}_Fw	GCACAGCATTGCGGACATGC	500
	R26^{nGFP}_Rv	GCAGAAGCGCGGCCGTCTGG	
Prox2^{FlpO}	Prox2^{FlpO}_Fw	GAGGGCAGCATCAGATACCC	555
	Prox2^{FlpO}_Rv	TGGTCTCTACTCTGGCCCTC	

3.2.2. Genotyping PCR program

Temperature (°C)	Time	
94	4 m	
95	30 s	35x
55	30 s	
72	1 m	
72	10 m	
8	∞	

3.3. Tissue preparation for histological analyses

Mice were sacrificed and perfused with PBS before organ harvesting. Dissected organs were washed in PBS before fixation in 4% PFA in PBS at 4°C (1 hour for vagal ganglia, 4 hours for digestive organs and 6 hours for brains). Pregnant dams were staged using the presence of a vaginal plug. The day that a vaginal plug was visible was designated as embryonic (E) day 0.5. Embryos were delivered by cesarean section and fixed for 3 hours in 4% PFA in PBS at 4°C. After fixation, organs and embryos were washed in PBS, cryopreserved in 15% sucrose overnight (ON) at 4°C, and then in 30% sucrose ON at 4°C. Organs were embedded in plastic molds with Tissue-Tek O.C.T Compound (Sakura) and stored at -80°C. Vagal ganglia were cryosectioned at 16 µm, embryos were cryosectioned at 20 µm, whereas digestive organs and brains were cryosectioned at 30 µm. Sections were stored at -80°C.

3.4. Immunofluorescence

Sections were thawed at 37°C for 30 minutes, briefly washed in PBS and PBX (PBS with 0.2% Triton X-100), and then blocked (PBS with 0.2% Triton X-100 and 5% normal horse serum) for 1 hour at room temperature. The primary antibody was diluted in blocking solution and incubated for 1-2 days at room temperature. Sections were washed in PBS before being incubated with the secondary antibody diluted in blocking solution for 1 hour at room temperature. Sections were again washed in PBS, and mounted with Immu-Mount (ThermoFisher). The following primary antibodies were used: goat anti-Phox2b (R&D Systems, AF4940, 1:200), rabbit anti-RFP

(Rockland, 600-401-379-RTU, 1:500), chicken anti-GFP (Aves Labs, GFP-1020, 1:500), rat anti-GFP (Nacalai Tesque, GF090R, 1:1000), goat anti-CD117 (R&D Systems, AF1356, 1:400), sheep anti-nNos (Millipore, AB1529, 1:250), goat anti-ChAT (Millipore, AB144P, 1:200), rabbit anti-Pou3f1 (Abcam, ab126746, 1:500), rabbit anti-Synapsin 1 (Abcam, AB1543, 1:500), guinea pig anti-VGlut2 (Synaptic Systems, 135 404, 1:500), rabbit anti-Tubulin β-3 (BioLegend, Poly18020, 1:1000), goat anti-CTb (List Labs, 703, 1:2000) and sheep anti-TH (Millipore, AB1542, 1:1000). We used species specific secondary antibodies coupled to Cy2-, Cy3- or Cy5 (Jackson ImmunoResearch, 1:500).

After immunostaining or smFISH, tissue sections were imaged using an LSM 700 confocal microscope (Carl-Zeiss) with 10x, 20x or 40x objectives and ZEN 2012 software.

3.5. Single molecule fluorescent *in situ* hybridization (RNAscope)

In situ fluorescent hybridization was performed using the RNAscope Multiplex Fluorescent Reagent Kit V2 from ACDbio according to the manufacturer's instructions. Briefly, vagal ganglia sections were thawed at 37°C for 20 minutes, and post-fixed in 4% PFA in PBS for 15 minutes before washing in PBS and dehydrating the tissue in 50%, 70% and 100% EtOH for 5 minutes each. The slides were allowed to completely dry before applying a hydrophobic barrier around the tissue. Next, the tissue was washed for 15 minutes in H_2O_2 (ACDBio) in the dark before washing in PBS. For combining immunohistology with RNAscope we incubated the tissue at 4°C ON with the primary antibody (goat anti-CTb (List Labs, 703, 1:2000)) diluted in Co-Detection Antibody Diluent (ACDBio). The next day sections were washed in PBS and then incubated in Protease III for 30 minutes. The sections were washed in PBS followed by hybridization with the RNAscope probes for 2 hours at 37°C. The C1 probe was heated at 40°C for 10 minutes, and the C2 / C3 probes were then diluted in the C1 probe 1:50. We used the following probes in this study: Prox2 (593331-C3), Runx3 (451271 and 451271-C2), Piezo2 (400191-C2 and 400191-C3), Trpv1 (313331), Prrxl1 (446631), Calb1 (428431-C3), Adra2a (425341-C3), Slc18a3 (448771-C3), Slc17a6 (319171-C3), Phox2b (407861-C2 and 407861-C3), Rbp4 (508501-C2), Gata3 (403321), Grm5 (423631-C2), Lamp5 (451071-C2), Mc4r (319181), Gabrg1 (501401-C3), Gpr65 (431431), Oxtr (412171) and Glp1r (418851). After the hybridization, sections were washed in wash buffer (ACDBio) and then signal amplification was performed with AMP1, AMP2, and AMP3 for 30 minutes each at 40°C. In between each amplification step sections were washed with wash buffer.

Probes were coupled to fluorophores in the following manner: sections were incubated with probe specific HRP (HRP-C1, HRP-C2, HRP-C3) for 15 minutes, followed by incubation with a TSA coupled fluorophore (TSA Plus 405, Opal 520 Reagent, TSA Plus Cy3, TSA Plus Cy5) diluted 1:1000 in RNAscope TSA buffer (ACDBio) for 30 minutes, followed by HRP blocking for 15 minutes. Sections were washed in wash buffer between each step, and each step was performed at 40°C. Each probe was coupled to a different fluorophore following the same steps as above. Sections were washed in wash buffer and incubated with the secondary antibody for 1 hour at room temperature in blocking solution (PBS with 0.2% Triton X-100 and 5% normal horse serum). Finally, sections were washed in PBS and mounted with ProLong Gold Antifade mountant (ThermoFisher).

If RNAscope was being performed without immunofluorescence then the protocol above was followed except for the incubation steps with primary and secondary antibodies.

3.6. Vagal neuron isolation for downstream single cell RNA sequencing

Vagal ganglia were dissected from 15 *VGlut2^{Cre};R26^{nGFP}* mice (9 males and 6 females) at P4 under a fluorescence dissecting microscope. Excess nerve, muscle and vascular tissue was removed, and ganglia were placed in a 1.5 ml Eppendorf tube with warm F12/FHS (F12 with 10% fetal horse serum). Neurons were isolated essentially as described (Lechner and Lewin, 2009). In short, ganglia were digested in F12/FHS solution containing 0.125% collagenase, incubated at 37°C for 1 hour, washed 3x in PBS, and then incubated in PBS with 0.25% trypsin at 37°C for 15 minutes. Ganglia were dissociated using fire-polished Pasteur pipettes of decreasing diameter. The solution was transferred on top of a 2 ml BSA cushion (F12/FHS solution with 15% bovine serum albumin) and spun for 10 minutes at 900 RPM. The cell pellet was resuspended in 500 µl of HBSS without calcium or magnesium, strained twice through a 70 µm filter (Sysmex), and DAPI (Sigma) was added to a final concentration of 300 nM to label dead cells before sorting. nGFP-positive / DAPI-negative neurons were sorted into 96-well plates using ARIA Sorter III (BD) and BD FACSDiva software 8.0.1.

3.7. Primary vagal neuron culture

Coverslips were sterilized, placed in the center of a 6-well plate, covered with 500µl of laminin-1 (1 µg/ml) and incubated at 37°C for 1 hour. Excess solution was removed, and coverslips

were allowed to dry. After vagal ganglia were dissociated as described above ~5,000 nGFP-positive and ~5,000 nGFP-negative cells were sorted into 1.5ml Eppendorf tubes containing 500 µl supplemented neurobasal media (Sterile Neurobasal (Gibco) with Penicillin (100 units/mL) and Streptomycin (Corning, 100 µg/mL), L-Glutamine (200 µM), B-27 (Gibco, 2%), nerve growth factor (NGF, Life Technology, 50 ng/mL), Glial cell line-derived neurotrophic factor (GDNF, Peprotech, 2 ng/mL). Cells were cultured as described previously (Wang et al., 2022). The 500 µl solutions containing either nGFP-positive or nGFP-negative cells were gently pipetted on top of separate coverslips in separate wells, and incubated at 37°C overnight. The next day the media was gently removed from the corner of the coverslip, and the well was gently filled with 2 ml of supplemented neurobasal media. After four days of culture, the cells were imaged using a brightfield microscope (Nikon DS-L3), then fixed in 4% PFA in PBS for 15 minutes before being processed for immunohistology.

3.8. Single cell RNA sequencing of vagal neurons using the CEL-Seq2 protocol

3.8.1. 96-well plate preparation

In order to prepare a master mix for 10 96-well plates mix 26.4 µl of 10% Triton X-100, 44 µl of 25 mM dNTPs, 11 µl of 1:10,000 ERCC spike-in (ERCC spike-in/cell is 1 µl (1:1,000,000 dilution), and 1018.6 µl of H_2O for a total of 1100 µl. Add 10 µl per well into a master mix 96-well plate, and then add 2 µl of the barcoded primer (1 µM, 25 ng/µl) into the corresponding well. Spin down the plate at 4°C, gently vortex, and spin down again at 4°C. Carefully pipette 1.2 µl form each well of the master mix 96-well plate into the corresponding wells of the 96-well plates, spin down at 4°C and store at -80°C.

3.8.2. RNA amplification

RNA amplification was done following the CEL-Seq2 protocol (Hashimshony et al., 2016). Briefly, following reverse transcription (0.4 µl first strand buffer (5x), 0.2 µl of 0.1M DTT, 0.1 µl RNaseOUT, 0.1 µl SSII per well) and second strand synthesis (7 µl H_2O, 2.31 µl second strand buffer, 0.23 µl of 10mM dNTPs, 0.08 µl E. coli DNA ligase, 0.3 µl E. coli DNA polymerase I, 0.08 µl RNase H per well) we pooled the contents of each well per 96-well plate into one 1.5 ml Eppendorf tube and performed bead purification with AMPure XP beads (Beckman Coulter). Next

we performed *in vitro* transcription (Ambion), aRNA fragmentation (New England Biolabs), bead purification with RNAClean XP beads (Beckman Coulter) and eluted in 7 µl H_2O. We confirmed the amount and quality of our aRNA by analyzing 1 µl of our aRNA from each 96-well plate on an RNA Pico chip with a Bioanalyzer (Agilent).

3.8.3. cDNA library generation

Briefly, we used the Bioanalyzer results from the RNA amplification to calculate the volume needed to obtain 5 ng aRNA from each 96-well plate, and adjusted the volume to 5 µl with H_2O. Next we primed the samples (1 µl Random HEX RT Primer CS2, 0.5 µl of 10 mM dNTPs per sample, and incubated the samples for 5 minutes at 65°C), before performing reverse transcription (2 µl first strand buffer (5x), 1 µl of 0.1 M DTT, 0.1 µl RNaseOUT, 0.1 µl SSII per well), followed by library PCR (10 µl Phusion HF buffer (5x), 1 µl of 10 mM dNTPs, 2 µl of RPI1 primer (Ilumina), 2 µl of RPIX primer (Ilumina), 0.5 µl Phusion DNA polymerase, 24.5 µl H_2O per sample) and bead purification with AMPure XP beads (Beckman Coulter) and eluted in 13 µl H_2O. cDNA concentration was measured using a Qubit 4 Fluorometer (ThermoFisher) and fragment length was measured using a high sensitivity DNA chip with a Bioanalyzer (Agilent). Libraries for 8 plates were then pooled together and adjusted to 2 nM.

3.8.4. Sequencing

Two libraries (1.3 ml at a concentration of 1.6 pM) were sequenced on high output flow cells using a NextSeq 500 (Ilumina) in two separate runs by the Next Generation Sequencing facility of the Max-Delbrück Center for Molecular Medicine. Due to the CEL-Seq2 protocol, we sequenced 16 base pairs (bp) in read 1, 8 bp in the index, and 51 bp in read 2 using the paired-sequencing mode.

3.9. Clearing and whole organ immunohistology

Mice were sacrificed, perfused with PBS to remove the blood and then perfused with 4% PFA in PBS. Vagal ganglia and digestive organs were dissected and fixed ON at 4°C in 4% PFA in PBS. Tissue was cleared using the CUBIC protocol (Susaki et al., 2015). Briefly, tissue was first washed ON at room temperature in PBS and then immersed in Sca*l*eCUBIC-1 (a mixture of 25% urea, 25% Quadrol, 15% Triton X-100 and 35% MQ-H_2O) diluted 1:1 with Milli-Q H_2O ON

in a 37°C water bath. The tissue was then placed in Sca*l*eCUBIC-1 in a 37°C water bath until the tissue became transparent (1/2 a day for vagal ganglia and 2-4 days for digestive organs). The solution was exchanged every 2 days. Once the organs were sufficiently cleared, they were washed ON at room temperature in PBS + 0.2% Triton X-100. Next, we incubated the organs with the primary antibodies diluted in modified blocking solution (PBS with 10% Triton X-100, 5% normal horse serum and 300 mM NaCl) for 10 days on a shaker at 37°C, refreshing the antibodies after 5 days. Organs were washed ON in PBS with 0.2% Triton X-100, incubated with the secondary antibodies and DAPI in modified blocking solution for 8 days on a shaker at 37°C, refreshing the antibodies after 4 days. The tissue was then immersed in EasyIndex RI = 1.46 (LifeCanvas Technologies) diluted 1:1 with Milli-Q H_2O ON in a 37°C water bath, before being transferred to EasyIndex RI = 1.46 ON for the final refraction index matching. Once the tissue was cleared, stained and refractive index matched it was placed into a square plastic mold filled with a 2% low melting point agarose prepared with EasyIndex RI = 1.46.

Cleared ganglia were imaged using a Zeiss lightsheet 7 microscope, while cleared digestive organs were imaged using a custom built mesoSPIM microscope (Voigt et al., 2019). Cleared, stained and embedded digestive organs were immersed in EasyIndex RI = 1.46 inside a small quartz glass cuvette (45 x 12.5 x 22.5 mm Portmann Instruments AG, UQ-205, quartz glass), which was placed inside a larger chamber (40 x 40 x 100 mm, Portmann Instruments AG, UQ-753-H100) filled with RI-matching liquid for fused silica (RI=1.46, Cargille Cat. #19569). The lightsheet illumination was delivered sequentially from the left and right sides, resulting in two different stacks per view, which were registered and fused into a single stack using BigStitcher (Horl et al., 2019) for each channel. The excitation laser line (Hübner Photonics C-Flex: 561 nm) was used with the corresponding detection filter (Chroma ET590/50m). The esophagus/stomach from an adult (3 months of age) *Prox2^{FlpO};Phox2b^{Cre};Ai65* mouse was acquired with a 1 x 3 tile scan at 1x zoom, while the esophagus/stomach from an adult (3 months of age) *Runx3^{Cre};Prox2^{FlpO};Ai65* mouse was acquired with a 2 x 6 tile scan at 2x zoom (Olympus 1x MVPLAPO1x). The images displayed in Figure 21A are maximum intensity Z-projections of the final fused images.

Vagal neuron counts at P4 were performed with Imaris v9.9 on the entire cleared and stained vagal ganglia.

3.10. Retrograde tracing of vagal sensory neurons innervating the upper digestive tract

WT adult mice (~3 month of age) were anesthetized with an intraperitoneal injection of ketamine/xylazine (80 mg/kg body weight ketamine (WDT) and 10 mg/kg body weight xylazine (Bayer)). The abdomen was shaved and betadine was applied to the abdominal skin. Ophthalmic ointment was applied to the eyes to prevent them from drying out during the procedure. A small transverse laparotomy was made below the sternum and fire polished glass Pasteur pipettes were used to position the organs prior to injection. Glass injection needles were prepared with a DMZ universal electrode puller (Zeitz-Instruments) and were filled with 0.5% CTb solution (ThermoFisher) in 0.9% NaCl. We added 0.2% Fast Green (Sigma) in order to visualize the injection site and confirm a successful injection. For glandular and non-glandular stomach injections a total of 2 µl was injected, while for abdominal esophagus 1 µl was injected, due to the smaller size of the target region. The injections were performed using a Nanoject III Programmable Nanoliter Injector (Drummond Scientific Company), with a volume of 250 nl and a speed of 50 nl/s per injection. In all cases, the needle was carefully placed into the muscle layer of the target regions and allowed to remain in place for 10 s before and after each injection. After the injections we performed layered wound closure, suturing the abdominal muscle layer first, followed by suturing the skin. Post-surgery mice were given a subcutaneous injection of Carprofen (5 mg/kg body weight, zoetis) and received Metamizol (ratiopharm) 1 ml/100 ml drinking water for analgesia. Mice were monitored twice daily to ensure that they were recovering properly, then were euthanized 4-5 days following surgery for vagal ganglia harvesting.

3.11. Ablation of Prox2 and Runx3 neurons

We generated *Prox2/Runx3*$^{ds\text{-}DTR}$ (*Prox2*^{FlpO};*Phox2b*^{Cre};*Tau*$^{ds\text{-}DTR}$) mice in which all cells with a history of Phox2b and Prox2 expression expressed the human diphtheria toxin receptor. We ablated *Prox2* and *Runx3* vagal neurons in adult mice (~6 months of age) by i.p. injection of Diphtheria toxin (DT, Sigma). DT was reconstituted in 0.9% NaCl, and injected at a concentration of 40 ng per gram bodyweight. After the ablation mice were monitored twice daily. If their weight dropped below 10% of their starting weight, they received a 0.5 ml i.p. injection of 0.9% NaCl and were given access to a nutritionally fortified water gel (DietGel Recovery, ClearH_2O). One male mouse continued to lose weight after the ablation and was euthanized before it could undergo endline testing. All other mice stabilized between 5-7 days post ablation.

3.12. *In vivo* analysis of swallowing behavior

Videofluoroscopy experiments to measure *in vivo* swallowing function were performed as previously described (Lever *et al.*, 2015; Welby et al., 2020). Briefly, mice (n=15, 8M and 7F, genotype: $Prox2^{FlpO};Phox2b^{Cre};Tau^{ds\text{-}DTR}$, 6 months of age) underwent videofluoroscopy swallow study (VFSS) at the University of Missouri using customized equipment and analysis software. The mice were shipped from the Max Delbrück Center in Berlin, Germany to the University of Missouri in MO, USA and were placed in quarantine for 3 weeks. During this time the mice were behaviorally conditioned with the VFSS chamber and oral contrast solution in order to familiarize them with the experimental set up and facilitate drinking during VFSS testing. Following release from quarantine, the mice were water restricted ON for 12 hours in order to increase their motivation to drink during testing the following morning. During the water restriction period, a VFSS chamber was placed in each home cage. Mice were each tested in their respective home cage chambers the following morning. VFSS testing was performed individually using a miniaturized, low energy (30 kV, 0.2 mA) fluoroscope (The LabScope, Glenbrook Technologies, Newark, NJ, USA) and videos were captured at 30 frames per second (fps). Mice were gently placed into the VFSS chamber and enclosed using two end-caps. One end-cap had a small bowl attached through which the liquid contrast agent (Omnipaque, GE Healthcare, 350 mg iodine/mL; diluted to a 25% solution with deionized water and 3% chocolate flavoring) could be administered during testing. The test chamber was then positioned within the lateral plane of the fluoroscope, and the bowl was filled with the liquid contrast agent via a custom syringe delivery device. When the mice began to drink, the fluoroscope was activated via a foot pedal. In order to minimize the radiation exposure time, the fluoroscope was turned off when the mice turned away from the bowl or initiated non-drinking behaviors. If mice did not drink, we placed them back in their home cage for ~30 mins and re-tested them. We captured drinking bouts in videos of approximately 30-60 s duration and saved them as AVI files. After baseline behavioral testing, mice underwent DT ablation of *Prox2* and *Runx3* vagal neurons. We allowed the mice to recover for 19 days after the ablation, at which point we re-tested the mice using the same VFSS protocol as above. Thus, we could compare the swallowing behavior of the same mice at baseline (pre-DT ablation) versus endline (post-DT ablation).

We imported the AVI files into Pinnacle Studio (version 24; Pinnacle Systems, Inc., Mountain View, CA) and identified drinking bouts between 2-5 s in length to obtain a total of 3-

15 s of uninterrupted drinking per mouse. The start of the drinking bouts was always at a swallow event, defined as when the liquid bolus abruptly moved from the vallecular space to the esophagus. The 2-5 s video clips were then imported into a custom VFSS analysis software (JawTrack™, University of Missouri) for subsequent frame by frame analysis. The software allows for the semi-automated extraction of many swallowing parameters such as lick rate (number of jaw open/close cycles per second, calculated for 2-5 s long video clips and then averaged), lick interval (time between successive lick cycles throughout a 2-5 s long video clip, and then averaged), swallow rate (number of swallows in each second of a 2-5 s video clip, then averaged), swallow interval (time between successive swallows throughout a 2-5 s video clip, then averaged), lick-swallow ratio (number of jaw open/close cycles between each successive swallow pair throughout a 2-5 s video clip, then averaged), pharyngeal transit time (bolus travel time through the pharynx for each swallow, then averaged), esophageal transit time (bolus travel time through the esophagus, then averaged), jaw closing velocity (speed at which the jaw closes during each jaw cycle throughout a 2-5 s video clip, then averaged) and jaw opening velocity (speed at which the jaw opens during each jaw cycle throughout a 2-5 s video clip, then averaged) (Mueller et al., 2022; Welby *et al.*, 2020).

3.13. Quantification and statistical analyses

All details regarding the number of samples and statistical tests performed can be found in the figure legends. Cell quantifications were performed in a non-blind, semi-automated manner on non-consecutive sections using FIJI/ImageJ (2.3.0/1.53q). Briefly between 3-8 images per animal were imported into ImageJ and immunofluorescent stainings were counted automatically. For the smFISH experiments a tdTomato+ cell or nGFP+ nucleus had to have at least 5 dots in order to be considered positive for a particular RNAscope probe. Cells and nuclei positive for an RNAscope probe were counted manually. All paired and unpaired t-tests were two-tailed, and no statistical test was done to predetermine sample sizes. One animal (#5697) was removed as an outlier from the Swallow interval and Lick to swallow ratio plots (Figure 38), as it failed the Grubbs' test with alpha=0.01. Significance for t-tests and ANOVAs was defined as * $p < 0.05$, ** $p < 0.01$, *** $p < 0.001$, **** $p < 0.0001$. Statistical analyses were performed using GraphPad Prism v6.0c.

4. Results

4.1. scRNA-seq of vagal sensory neurons at P4

At the time that this thesis was initiated in 2017, there was no scRNA-seq dataset of vagal neurons available, the first of which was published in 2019 (Kupari *et al.*, 2019). This was due to the low number of vagal neurons in the mouse (~5,000 per side) and the difficulty in accessing them due to their location buried in the jugular foramen at the base of the skull. In order to overcome the difficulty of dissecting the vagal ganglia in adult animals, we decided to use mice at postnatal day (P) 4. We genetically labeled all vagal neurons with a nuclear GFP reporter (*VGlut2^{Cre};R26^{nGFP}*, Figure 4A left) (Raab and Neuhuber, 2007). We cleared whole vagal ganglia, used lightsheet imaging to capture the vagal ganglia *in toto*, and detected all vagal nuclei using image analysis software (Figure 4A middle).

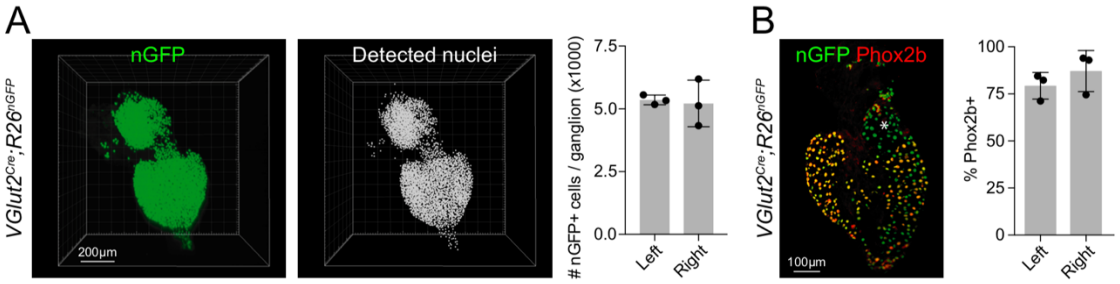

Figure 4. Each vagal ganglion contains ~4,000 nodose neurons and ~1,000 jugular neurons. (A) Lightsheet imaging (acquired with a Zeiss lightsheet 7) of a vagal ganglion from a *VGlut2^{Cre};R26^{nGFP}* mouse at postnatal day P4; GFP+ neuronal nuclei (green, left), and all detected nuclei (gray, right) are shown. Detected nuclei were quantified using IMARIS v9.9.0 (left: 5358±192 nuclei, right: 5218±929 nuclei, n=3, p=0.8118). **(B)** Immunohistological analysis of Phox2b (red) and nGFP (green) in the vagal ganglia of a *VGlut2^{Cre};R26^{nGFP}* mouse at postnatal day P4. The percentage of nodose neurons (Phox2b+nGFP+) is quantified on the right (left: 79.3±7.1%, right: 87.2±10.9%, n=3, p=0.3557). Data are represented as mean ± SD, paired two-tailed t-test.

The total number of detected vagal neurons per ganglion was ~5,000, with no differences between the left and right ganglia, which is the same number of vagal neurons found in the adult (Figure 4A right) (Ichikawa *et al.*, 2006). As a further confirmation that the vagal ganglia at P4 resemble that of the adult, we counted the number of Phox2b+nGFP+ nodose neurons (Figure 4B left). Phox2b is expressed exclusively in nodose neurons, and in the adult these account for roughly 85% of all vagal neurons (Kupari *et al.*, 2019; Pattyn *et al.*, 1999). At P4, the proportion of nodose neurons is similar, with no differences between the left and right ganglia (Figure 4B right). Thus,

at P4 the mouse vagal ganglia already contain the same number of neurons and the same proportion of nodose versus jugular neurons as the adult.

In order to obtain viable cells for scRNA-seq, we performed fluorescently activated cell sorting (FACS) on freshly dissociated vagal ganglia from *VGlut2*^{Cre};*R26*^{nGFP} mice at P4 (Figure 5A). To increase the number of sorted cells we dissociated vagal ganglia from 15 mice, including 9 males and 6 females, and performed FACS in two separate experiments. Together, we collected 16 96-well plates for a total of 1536 vagal neurons.

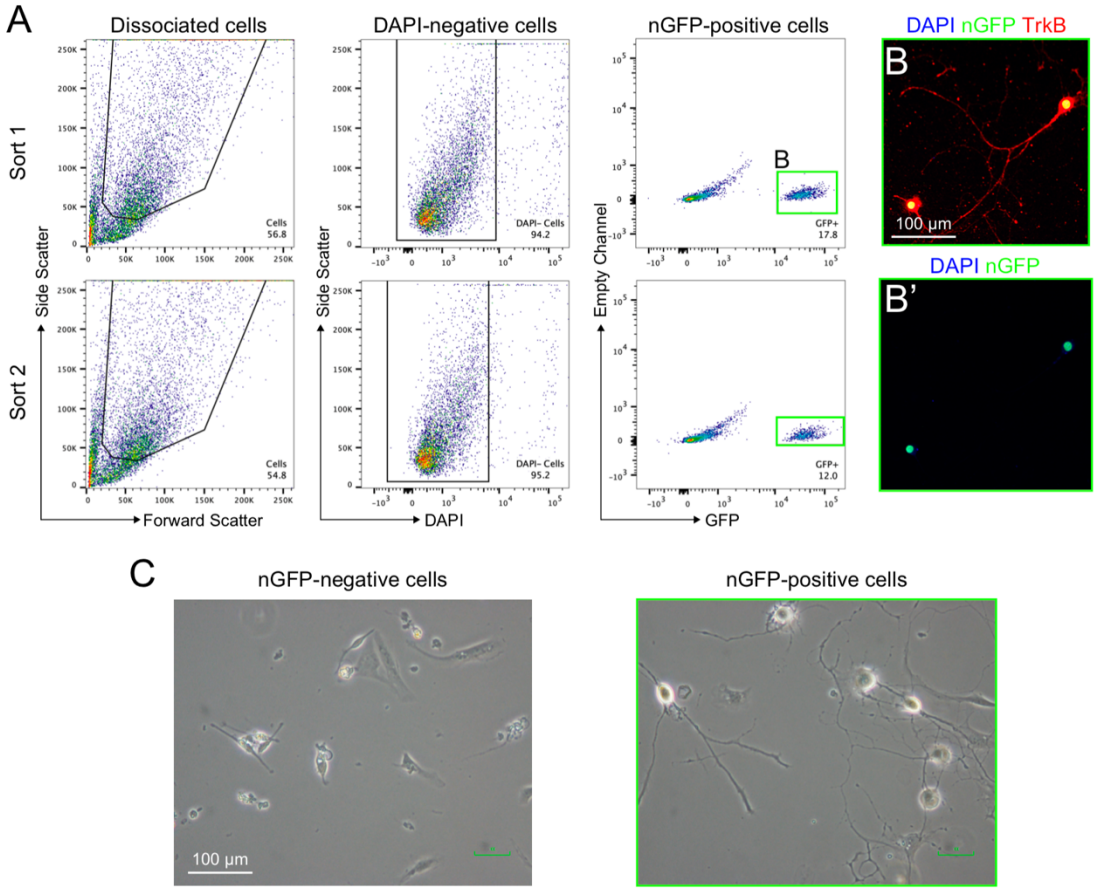

Figure 5. Sorted nGFP+ cells are vagal neurons. (A) Vagal neurons from *VGlut2*^{Cre};*R26*^{nGFP} mice were dissociated and subjected to flow cytometry at P4. Sort 1 included vagal ganglia from 5 mice, 4M and 1F, while sort 2 was from 10 mice, 5M and 5F. After large cells were selected using side and forward scatter, DAPI was used as a cell viability marker to select for DAPI-negative non-damaged cells. Finally, we sorted nGFP+ cells (green boxes) into 96-well plates, while excluding nGFP-negative cells. **(B,C)** We performed a separate experiment where we sorted vagal neurons as described above and collected all nGFP+ and nGFP-negative cells which were then cultured for 96 hours. **(B)** Immunohistological analysis of cultured nGFP+ cells shows that they are TrkB+ (red) and nGFP+ (green). **(C)** Neurites only formed in the cultured nGFP+ cells. In total we sorted 1536 nGFP+ neurons into 16 96-well plates for downstream scRNA-seq analysis.

We used DAPI as a cell viability marker and purified similar proportions of nGFP+ neurons in both experiments (compare Sort 1 and Sort 2, Figure 5A). To check whether the sorted nGFP+ cells were viable neurons we cultured sorted nGFP+ and nGFP- cells for 4 days (Figure 5B,C). Whereas nGFP- cells never displayed neuronal morphology, the nGFP+ cells displayed a clear neuronal morphology, including growing neurites and contacting neighboring neurons (Figure 5C). Immunohistology confirmed that sorted nGFP+ neurons were nGFP+ and TrkB+ (Figure 5B), indicating that our dissociation and sorting procedure enriched for viable vagal neurons.

To investigate the heterogeneity of vagal neurons at P4, we performed scRNA-seq using the plate-based CEL-Seq2 method that has high gene and mRNA detection sensitivity (Hashimshony *et al.*, 2016). We sequenced 768 vagal neurons in two separate runs, and found no differences in the number of detected genes or unique molecular identifiers (UMIs), nor in the percentage of reads that mapped to mitochondrial genes (Figure 6, top row).

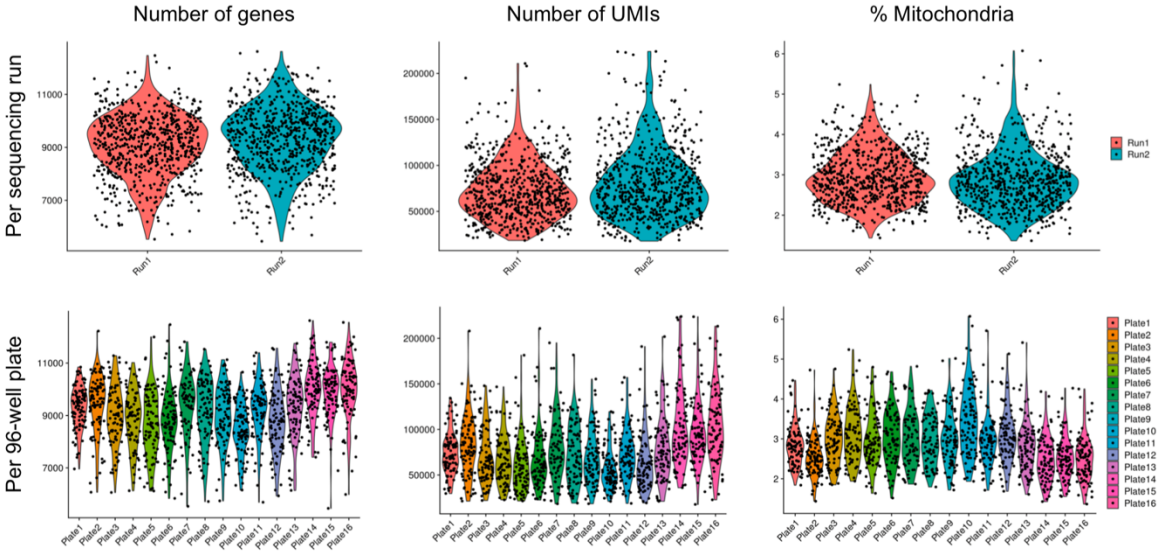

Figure 6. scRNA-seq quality control. In order to uncover possible artefacts, we plotted the number of genes **(left column)**, number of unique molecular identifiers (UMIs, **middle column**) and the % of all UMIs that mapped to mitochondrial genes **(right column)**, per sequencing run **(top row)**, and per 96-well plate **(bottom row)**. There were no major differences in these parameters due to our experimental procedures.

There were also no differences in these parameters when we looked per 96-well plate (Figure 6, bottom row), demonstrating that our scRNA-seq data did not have any technical biases due to the individual sequencing runs or FACS experiments.

After removing neurons with more than 250,000 or less than 17,000 UMIs, 1,392 neurons remained for which a median of 9,323 genes and 70,667 unique molecular identifiers per neuron were identified. The analysis of this dataset defined 22 distinct vagal neuron subtypes (C1-22, Figure 7A). The two parts of the vagal ganglia, the nodose and jugular ganglia (also known as inferior and superior vagal ganglia), derive from the epibranchial placode and cranial neural crest, respectively (Ayer-Le Lievre and Le Douarin, 1982; D'Amico-Martel and Noden, 1983; Narayanan and Narayanan, 1980).

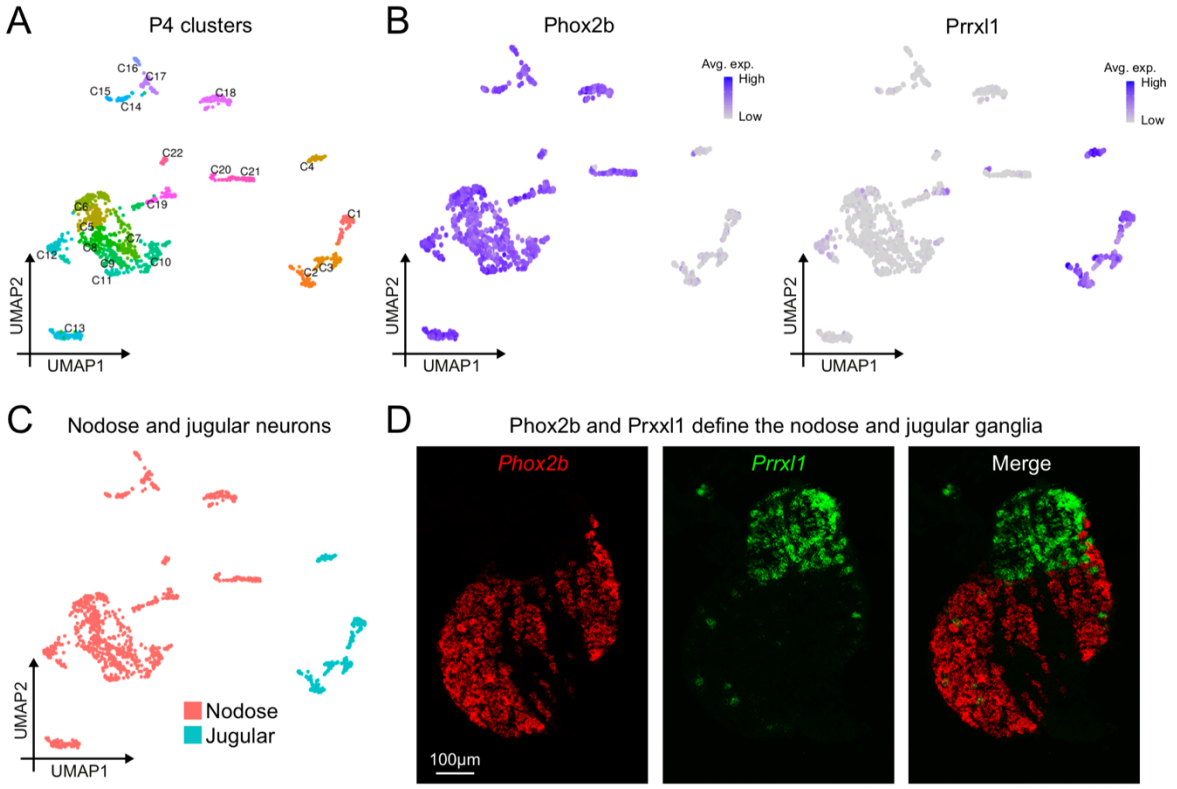

Figure 7. scRNA-seq analysis assigns a developmental origin to vagal neuron subtypes. (A) Uniform manifold approximation and projection (UMAP) plot revealed 22 subtypes of vagal neurons at P4, color coded and numbered C1-22. **(B)** UMAP plots showing the expression of the transcription factors *Phox2b* and *Prrxl1*. **(C)** UMAP plot showing the division between nodose (peach, defined as *Phox2b*+) and jugular subtypes (turquoise, defined as *Prrxl1*+). **(D)** Single molecule RNA fluorescent *in situ* hybridization (smFISH) using probes against *Phox2b* (red) and *Prrxl1* (green) differentiates between the nodose and jugular ganglia, respectively.

Whereas nodose neurons are viscerosensory and innervate the inner organs, jugular neurons are somatosensory and innervate structures in the head and neck (Prescott and Liberles, 2022). Nodose and jugular superclusters express *Phox2b* and *Prrxl1*, respectively, that are known to mark

placodally- and neural crest-derived neuronal types (D'Autreaux *et al.*, 2011; Pattyn *et al.*, 1999). Subtypes C5-22 expressed *Phox2b* and are therefore nodose neurons, while C1-4 expressed *Prrxl1* and are jugular neurons (Figure 7B). The nodose neuronal subtypes are located together on the left of the UMAP plot, while the jugular neuronal subtypes are located together on the right of the UMAP plot (Figure 7C). Single molecule fluorescent *in situ* hybridization (smFISH) against *Phox2b* and *Prrxl1* mRNA shows that these transcription factors mark the abutting inferior nodose and superior jugular ganglia, respectively (Figure 7D).

The 18 *Phox2b*+ nodose subtypes, C5-22 (Figure 8A, see also Figure 7), were subdivided in the UMAP according to their expression of two ion channels, *Trpv1* and *Piezo2*, that mark putative chemo- and mechanoreceptors, respectively (Figure 8B). *Trpv1* is activated by temperature and pain, *Piezo2* is activated by mechanical stimulation, and although these ion channels are not expressed ubiquitously in all chemo- or mechanoreceptors, we used these markers to get a preliminary overview of the putative functions of nodose neuronal subtypes (Caterina et al., 1997; Coste et al., 2010).

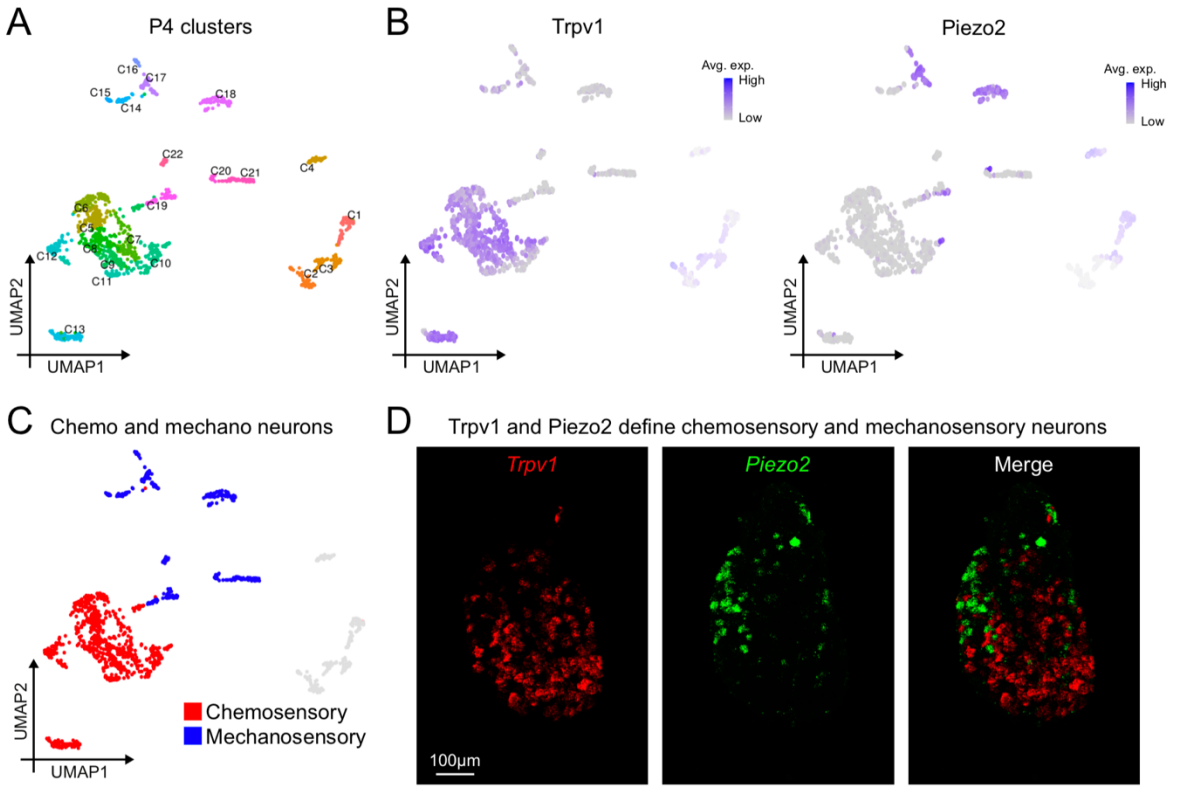

Figure 8. scRNA-seq analysis assigns a putative function to nodose neuron subtypes. (A) UMAP plot revealed 22 subtypes of vagal neurons at P4, including 18 subtypes of *Phox2b*+ nodose neurons C5-22. (See also Figure 4B) **(B)** UMAP plots showing the expression of *Trpv1* and *Piezo2* in the nodose subtypes, jugular subtypes are faded. **(C)**

UMAP plot showing the division between nodose putative chemoreceptor (red, defined as *Trpv1*+) and mechanoreceptor subtypes (blue, defined as *Piezo2*+), jugular subtypes are faded. **(D)** smFISH using probes against *Trpv1* (red) and *Piezo2* (green) differentiates between the putative chemoreceptors and mechanoreceptors, respectively.

Similarly to the division between nodose and jugular vagal neurons, chemo- and mechanoreceptive nodose subtypes are also located in distinct portions of the UMAP, with *Trpv1*+ nodose neuronal subtypes in the bottom left, and *Piezo2*+ nodose neuronal subtypes in the top right of the UMAP (Figure 8C). In contrast to the sharp division between nodose and jugular neurons (Figure 7D), putative chemo- and mechanoreceptors are distributed in a salt and pepper manner throughout the nodose ganglia (Figure 8D). In summary, the scRNA-seq analysis allowed us to subdivide vagal neuron subtypes by their embryonic origin and putative function. All bioinformatics analyses described above were performed by Aristotelis Misios in the Nikolaus Rajewsky laboratory.

4.2. Meta-analysis of vagal neurons reveals the Prox2+ and Runx3+ superclusters of putative mechanoreceptors

Shortly after we collected the scRNA-seq data described in the previous section, two scRNA-seq datasets of vagal neurons were published (Bai *et al.*, 2019; Kupari *et al.*, 2019). In the same year a computational method was published that allowed for the integration of multiple scRNA-seq datasets into a meta-analysis (Stuart et al., 2019). The integration of multiple transcriptomic datasets increases the number of analyzed cells, uncovering rare subtypes and improving subtype annotation. Therefore, we performed a meta-analysis on 4,442 vagal neurons that included 1392 neurons isolated at P4 (this project), 395 and 956 neurons isolated at P42 and between P56-84, respectively (Bai *et al.*, 2019), and 1,707 neurons isolated between P32-35 (Kupari *et al.*, 2019) (Figure 9A). UMAP analysis of the combined datasets revealed a large heterogeneity between vagal neurons and improved the resolution of their diversity. The meta-analysis indicated that the roughly 10,000 vagal neurons per mouse (Figure 4A) segregate into 27 transcriptomically distinct subtypes (Figure 9B). Cells from all datasets, including our P4 dataset, contributed to all 27 subtypes, indicating that shortly after birth all subtypes are specified (Figure 9C). The meta-analysis can be freely explored at https://shiny.mdc-berlin.de/VGIE/.

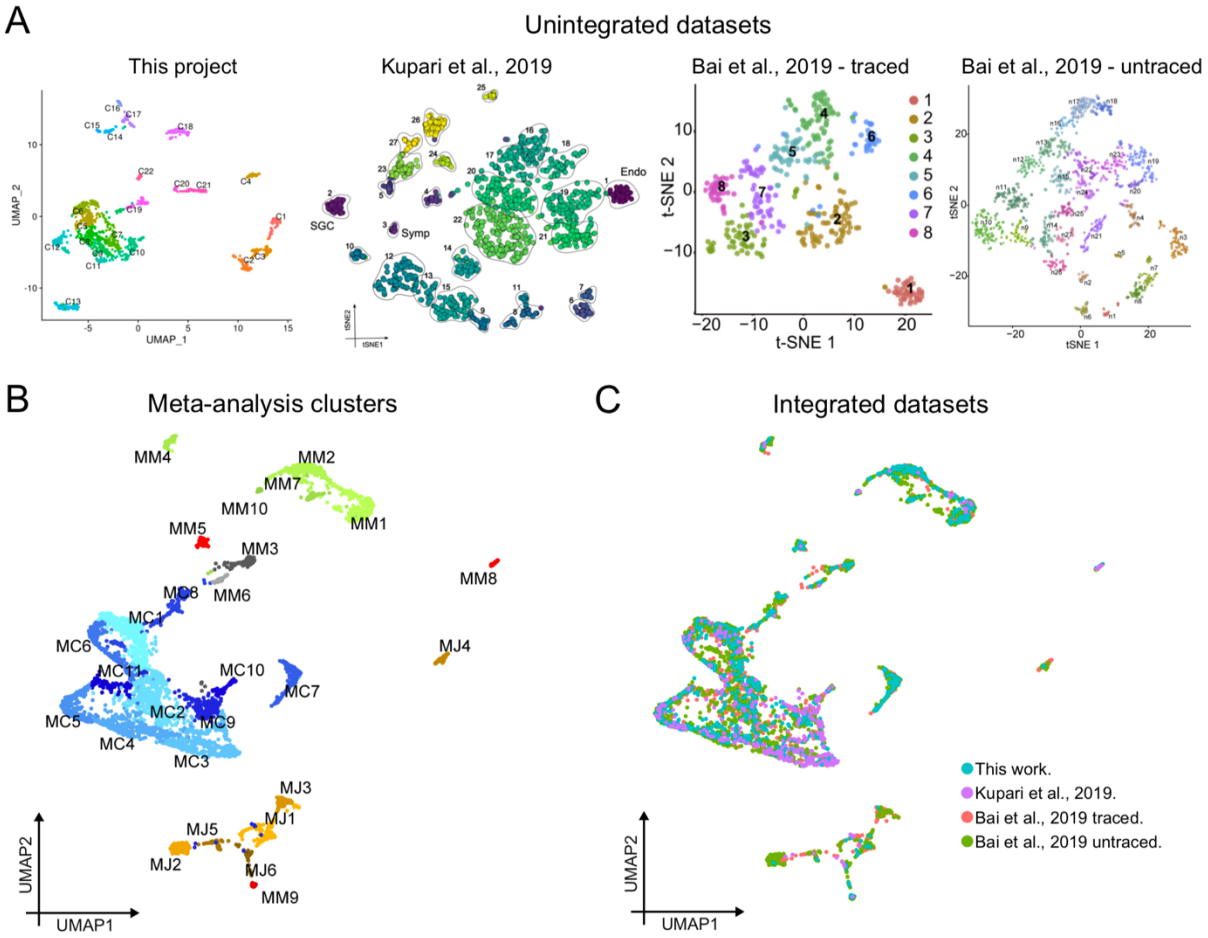

Figure 9. Meta-analysis reveals 27 vagal neuron subtypes. (A) UMAP or tSNE plots of the individual vagal neuron scRNA-seq datasets that were combined in the meta-analysis. This included data from this project, Kupari et al., 2019 and Bai et al., 2019 (traced and untraced datasets). **(B)** UMAP plot based on our meta-analysis revealed 27 subtypes (color-coded and numbered, *M*eta-*J*ugular (MJ) 1-6, *M*eta-*C*hemo (MC) 1-11, *M*eta-*M*echano (MM) 1-10). **(C)** UMAP plot based on the meta-analysis displaying cells detected in each dataset by a separate color; all datasets contributed cells to each subtype.

We applied a semi-supervised method to group the 27 vagal neuronal subtypes into broader groups that were termed 'superclusters'. The 'Jugular' supercluster expresses the homeobox transcription factor *Prrxl1*, and all jugular subtypes were located together in the bottom right of the UMAP (Figure 10A). Three superclusters of nodose neurons were grouped together in the UMAP: 'Prox2' expressing the homeodomain transcription factor *Prox2*, 'Gabra1' expressing the gene encoding the alpha-1 (α1) subunit of the GABAA receptor and 'Chemo', a putative chemoreceptor supercluster expressing *Trpv1* and *Npy2r* (Figure 10A,B). The three remaining

neuronal subtypes scattered in the UMAP, and all expressed the homeodomain transcription factor *Runx3*.

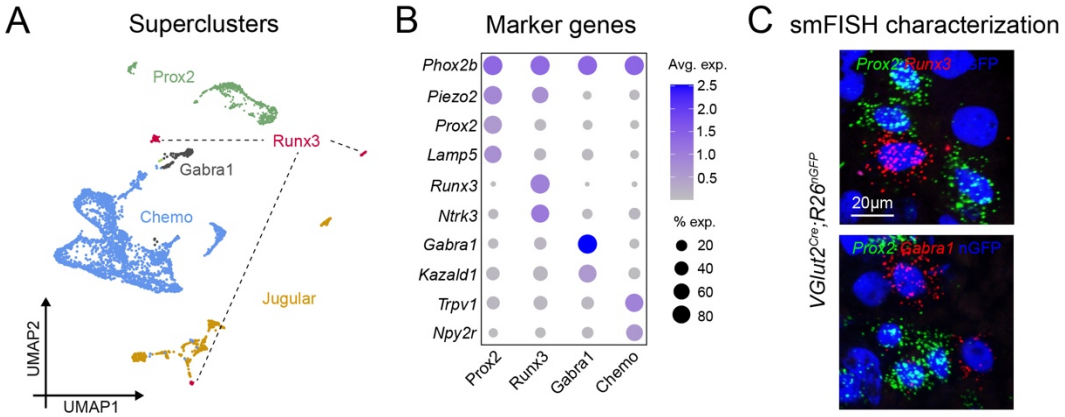

Figure 10. Meta-analysis of vagal neurons reveals four superclusters of nodose neurons. (A) UMAP plot based on a meta-analysis of scRNA-seq data from this work and two published reports (Bai et al., 2019; Kupari et al., 2019), showing five vagal neuron superclusters (Prox2, green; Runx3, red; Chemo, blue; Gabra1, dark grey; and Jugular, gold). **(B)** Dot plot showing the expression of selected genes that define the four Phox2b+ nodose superclusters (Prox2, Runx3, Gabra1 and Chemo). **(C)** Representative smFISH images showing *Prox2* (green) and *Runx3* (red) mRNA and immunohistological analysis of nGFP (blue) on vagal ganglia sections from *VGlut2*^{Cre}*;R26*^{nGFP} mice at postnatal day (P) 8.

They were merged into a fourth supercluster named 'Runx3'. smFISH against *Prox2*, *Runx3* and *Gabra1* mRNA in *VGlut2*^{Cre}*;R26*^{nGFP} mice revealed that these superclusters are largely non-overlapping at P8 (Figure 10C).

Together, the Prox2 and Runx3 superclusters contained ~84% of all nodose *Phox2b*+*Piezo2*+ neurons (Figure 11A). As Piezo2 transduces mechanical information in many neuron types (Coste *et al.*, 2010; Murthy et al., 2017), we hypothesized that the Prox2 and Runx3 superclusters were candidate vagal mechanoreceptors innervating the internal organs. The remaining nodose *Phox2b*+*Piezo2*+ neurons were assigned to the 'Chemo' supercluster and might correspond to polymodal afferents (Figure 11A). smFISH was used to examine the colocalization of *Piezo2*, *Prox2* and *Runx3* mRNA in vagal neurons (Figure 11B, left). In agreement with the sequencing data, we found that 90±3% of *Prox2*+ neurons and 63±3% of *Runx3*+ neurons co-expressed *Piezo2* (Figure 11B, middle). Prox2+ and Runx3+ subtypes express additional genes, such as *Kcnk2*, *Asic1*, and *Asic2* (Figure 11B, right) that have been implicated in mechanoreception (Ranade et al., 2015). The Prox2 and Runx3 superclusters encompass five and three

transcriptomically unique neuronal subtypes, respectively; we refer to these as *M*eta-analysis putative *M*echanoreceptors MM1, MM2, MM4, MM7, MM10 (Prox2+ subtypes) and MM5, MM8, MM9 (Runx3+ subtypes).

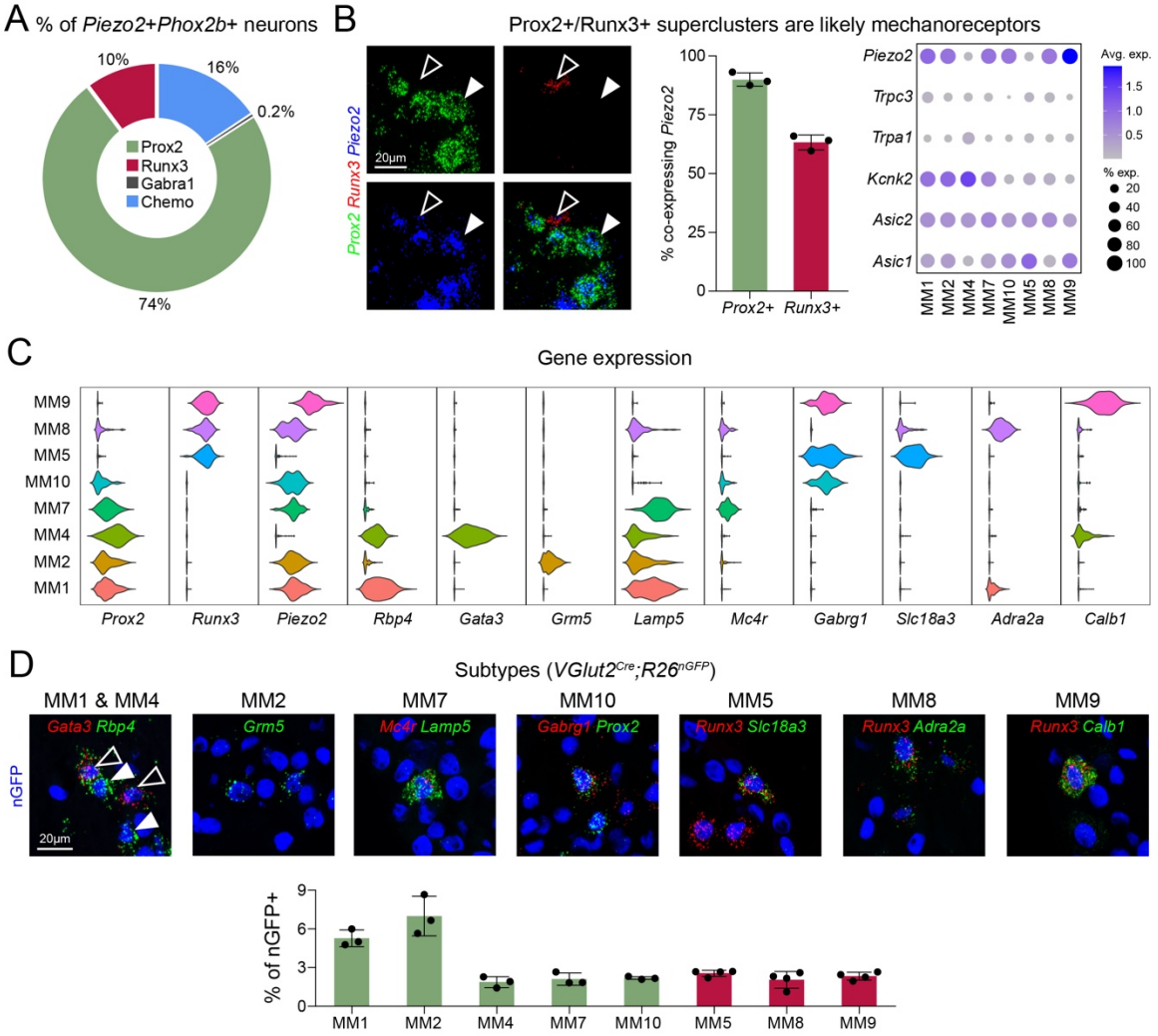

Figure 11. Meta-analysis of vagal neurons reveals the Prox2 and Runx3 superclusters of putative mechanoreceptors. (A) Donut chart showing the supercluster identity of Piezo2+Phox2b+ nodose neurons. **(B) Left**, representative smFISH images showing *Prox2* (green), *Runx3* (red) and *Piezo2* (blue) mRNA on vagal ganglia sections from wildtype mice at P8. Open arrowhead marks a *Runx3*+*Piezo2*+ neuron, while the closed arrowhead marks a *Prox2*+*Piezo2*+ neuron. **Middle**, quantifications showing that the majority of *Prox2*+ (90.0±2.8%, n=3) and *Runx3*+ (63.8±3.2%, n=3) neurons co-express *Piezo2*. **Right**, dot plot showing the expression of selected mechanosensory genes in the Prox2 and Runx3 neuronal subtypes. Note that the Prox2 MM4 and Runx3 MM5 subtypes are *Piezo2*-negative. **(C)** Violin plots showing the expression of selected marker genes that were used to identify the Prox2 and Runx3 neuronal subtypes in panel D. **(D) Above,** smFISH images identifying Prox2 neuronal subtypes MM1, MM2, MM4, MM7 and MM10 and Runx3 neuronal subtypes MM5, MM8, MM9. smFISH was performed on vagal ganglia sections from *VGlut2*^{Cre}*;R26*^{nGFP} mice at P8; vagal neuronal nuclei expressing nGFP were

identified by immunofluorescence and are shown in blue. **Below**, quantification of Prox2 and Runx3 neuronal subtypes, as a percent of all nGFP+ vagal neurons, n=3-4. Data are represented as mean ± SD.

Four and two of the Prox2+ and Runx3+ subtypes, respectively, express *Piezo2* (Figure 11B). Each individual subtype can be defined by the expression of a specific combination of marker genes (Figure 11C), which was verified using smFISH on vagal ganglia sections from *VGlut2^{Cre};R26^{nGFP}* mice at P8 (Figure 11D, top). Each subtype represents ~2-8% of all vagal neurons (Figure 11D, bottom). Our meta-analysis revealed that mouse vagal sensory neurons are highly heterogenous, and that they are already specified shortly after birth. Further, most putative mechanoreceptors belong to the Prox2 and Runx3 superclusters, which together encompass eight subtypes of vagal neurons. All bioinformatics analyses described above were performed by Aristotelis Misios in the Nikolaus Rajewsky laboratory.

4.3. Prox2 and Runx3 neurons are developmentally related

In the adult mouse, the vast majority of Prox2 and Runx3 neurons exclusively expressed one or the other of these two transcription factors (Figures 10C,11C). However, smFISH analysis in *Phox2b^{Cre};Ai14* animals during embryonic development (E11.5) revealed that *Prox2* and *Runx3* are extensively co-expressed in tdTomato+ nodose neurons (Figure 12, left).

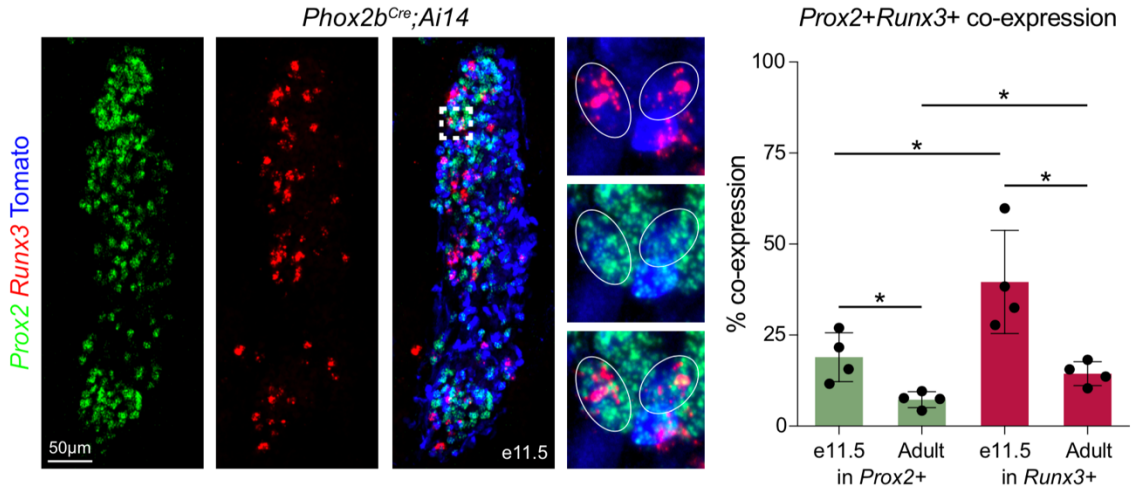

Figure 12. Prox2 and Runx3 neurons are developmentally related. Left, representative smFISH images against *Prox2* (green) and *Runx3* (red) mRNA and immunohistological analysis of tdTomato (blue) on vagal ganglia sections from *Phox2b^{Cre};Ai14* mice at embryonic (E) day 11.5. White circles mark double positive *Prox2*+*Runx3*+ neurons. **Right**, Quantification of *Prox2*+*Runx3*+ co-expression, n=4. Green bars show the percentage of *Prox2*+ neurons co-expressing *Runx3* at E11.5 (19.0±6.7%) and in the adult (7.3±2.2%), and red bars show the percentage of all Runx3+

neurons co-expressing Prox2 at E11.5 (39.6±14.2%) and in the adult (14.4±3.3%). The proportion of *Prox2*+*Runx3*+ double positive cells was greater at E11.5 than in adults both in the Prox2 population (p=0.0162) and in the Runx3 population (p=0.0134), and the proportion of *Prox2*+*Runx3*+ double positive cells was greater in the Runx3 population than in the Prox2 population both at E11.5 (p=0.0388) and in the adult (p=0.011). Data are represented as mean ± SD, *p<0.05, unpaired two-tailed t-test.

We found more *Prox2*+*Runx3*+ cells at E11.5 than in the adult in both *Prox2*+ and *Runx3*+ neurons, and that co-expression was more common in *Runx3*+ than in *Prox2*+ neurons at both analyzed stages. In particular, 40±14% of Runx3+ neurons co-expressed Prox2 at E11.5, indicating that the Prox2+ and Runx3+ superclusters are developmentally related (Figure 12, right).

4.4. Generation and characterization of the *Prox2^{FlpO}* transgenic mouse

In order to further investigate the putative vagal mechanoreceptors we generated a *Prox2^{FlpO}* knock-in transgenic mouse strain. *In situ* hybridizations from the Allen Brain Atlas showed that *Prox2* expression is restricted to the cranial ganglia during development (Figure 13A), but in the adult *Prox2* is also expressed in other cell types (Nishijima and Ohtoshi, 2006). In collaboration with the transgenic core facility at the Max Delbrück Center for Molecular Medicine we used CRISPR/Cas9 to insert a 1.5 kb fragment containing the codon-optimized FLP recombinase (FlpO) and a bovine poly(A) sequence between the 5' UTR and 1st exon of the *Prox2* gene by homology-directed repair (Wefers et al., 2017) (Figure 13B).

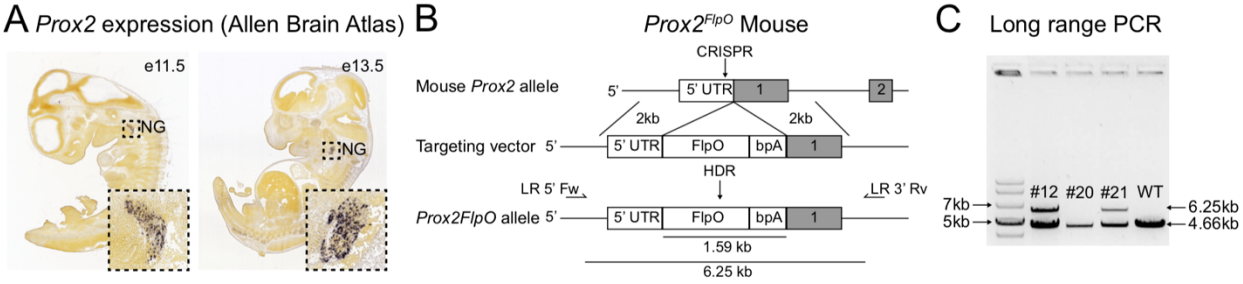

Figure 13. Generation of the *Prox2^{FlpO}* mouse. (A) *In situ* hybridizations against *Prox2* mRNA in sagittal sections of E11.5 **(left)** and E13.5 **(right)** embryos; inset shows a magnification of the nodose ganglion (NG). Pictures were obtained from the Allen Brain Atlas: Developing Mouse Brain. **(B)** Scheme showing the strategy used to generate the *Prox2^{FlpO}* allele. **(C)** Long range PCR was used to confirm the insertion of the *Prox2FlpO* targeting vector. Animals #12 and #21 were used as founders as they had the 6.25kb band signifying correct insertion of the targeting vector. The wildtype (WT) control only shows a 4.66 WT band.

The donor vector contained genomic sequences 2kb upstream (5' homology arm) and 2kb downstream (3' homology arm) of the 1st exon of the *Prox2* gene. Successful insertion of the 1.5 kb fragment was confirmed by long range PCR, with primers designed upstream (LR 5' Fw) and downstream (LR 3' Rv) of the homology arms (Figure 13B). Wildtype (WT) mice that did not harbor the 1.5 kb fragment had a single 4.66 kb band, while animals with a correctly inserted 1.5 kb fragment had both a 4.66 kb band (WT allele) and the 6.25 kb band (*Prox2*^{FlpO} allele) (Figure 13C). Mouse #12 was chosen as the founder for the *Prox2*^{FlpO} strain.

As Prox2 is expressed in other tissues we used an intersectional genetic strategy combining *Prox2*^{FlpO} and *Phox2b*^{Cre} with *Ai65,* a tdTomato expressing reporter allele*,* to specifically label Prox2+ neurons in vagal ganglia (*Prox2*^{FlpO}*;Phox2b*^{Cre}*;Ai65* animals). Indeed, analysis of tdTomato expression in adult mice showed that 95±4% of vagal *Prox2*+ neurons were recombined and expressed tdTomato (Figure 14A). However, 71±2% of vagal *Runx3*+ neurons were also recombined, reflecting the shared developmental history of Prox2+/Runx3+ neurons (Figure 14B and Figure 12). Thus, recombination in *Prox2*^{FlpO}*;Phox2b*^{Cre}*;Ai65* animals occurs in both *Prox2*+ and *Runx3*+ neurons, and we hereafter refer to these mice as *Prox2/Runx3*^{Tom}.

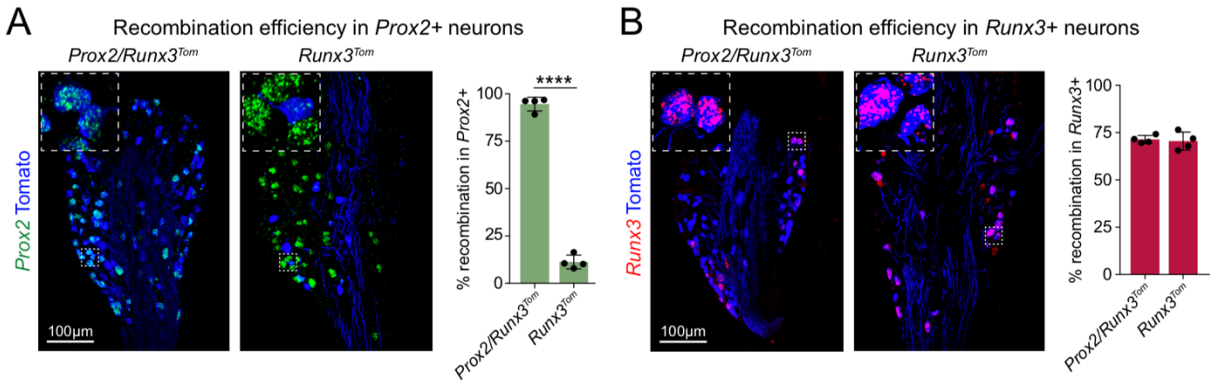

Figure 14. Characterization of the *Prox2*^{FlpO} mouse strain recombination efficiency in vagal neurons. (A) Recombination efficiency in *Prox2*+ neurons in *Prox2/Runx3*^{Tom} (*Prox2*^{FlpO}*;Phox2b*^{Cre}*;Ai65*) (left) and *Runx3*^{Tom} (*Runx3*^{Cre}*;Prox2*^{FlpO}*;Ai65*) (right) animals. Quantifications show that 94.8±3.6% and 11.3±3.6% ($p<0.0001$) of *Prox2*+ neurons (green) were recombined in *Prox2/Runx3*^{Tom} and *Runx3*^{Tom} mice, respectively, n=4. **(B)** Recombination efficiency in *Runx3*+ neurons in *Prox2/Runx3*^{Tom} (left) and *Runx3*^{Tom} (right) animals, n=4. Quantifications show that 71.4±2.1% and 70.5±4.8% ($p=0.744$) of *Runx3*+ neurons (red) were recombined in *Prox2/Runx3*^{Tom} and *Runx3*^{Tom} mice, respectively, n=4. Data are represented as mean ± SD, ****$p<0.0001$, unpaired two-tailed t-test.

To complement the histological analyses relying on the *Prox2/Runx3*^{Tom} strain, the *Runx3*^{Cre} allele was also used. Runx3 is expressed in proprioceptive dorsal root ganglia neurons and various non-neuronal cells types (Levanon et al., 2002; Shin et al., 2021). To exclude these neuronal cell types and restrict recombination, we initially analyzed *Runx3*^{Cre}*;Phox2b*^{FlpO}*;Ai65* animals. Although vagal Runx3+ neurons were recombined in these mice, we occasionally observed recombination in enteric and sympathetic ganglia (data not shown). Therefore *Runx3*^{Cre}*;Prox2*^{FlpO}*;Ai65* animals were subsequently used to label Runx3+ vagal neurons (hereafter named *Runx3*^{Tom} mice). Analysis of tdTomato expression in *Runx3*^{Tom} mice showed recombination in 70±5% of vagal *Runx3*+ neurons (Figure 14B), but only in a minor proportion of *Prox2*+ neurons (Figure 14A).

We verified that each subtype was recombined using smFISH on vagal ganglia sections from *Prox2/Runx3*^{Tom} (Figure 15A, left) and *Runx3*^{Tom} (Figure 15A, right) mice. These experiments confirm that *Prox2* is expressed during the development of Runx3+ vagal neurons (Figure 15B and Figure 12).

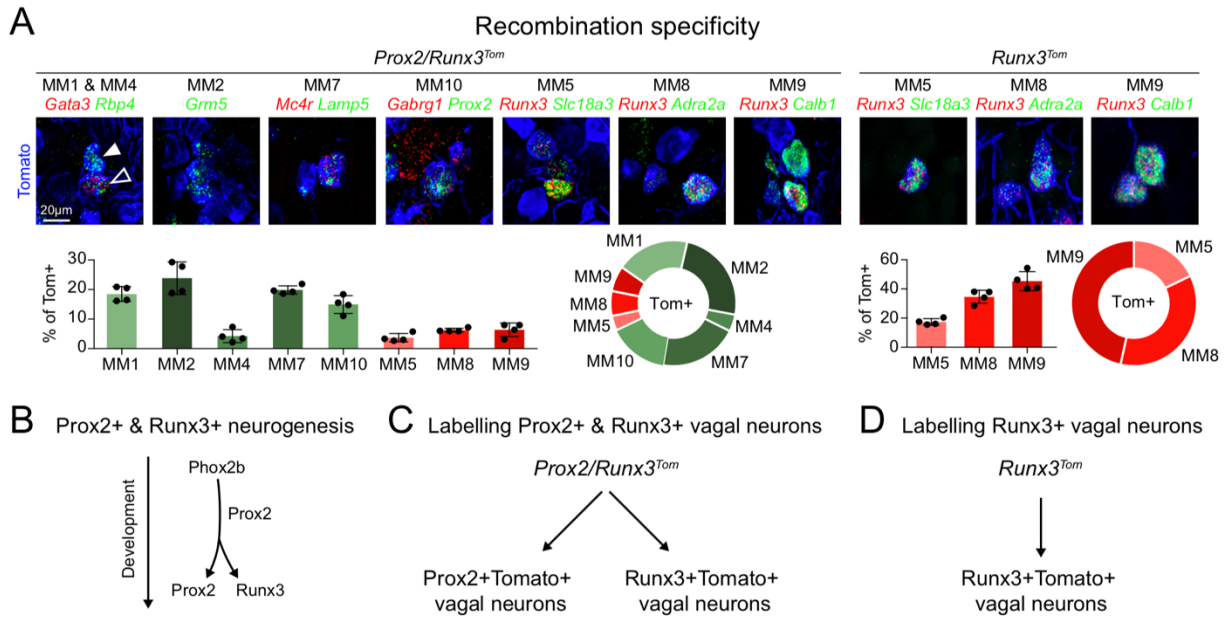

Figure 15. Characterization of the *Prox2*^{FlpO} mouse strain recombination specificity in vagal neurons. (A) Representative smFISH images from *Prox2/Runx3*^{Tom} **(left)** animals showing recombination specificity in *Prox2*+ (green) and *Runx3*+ (red) neuronal subtypes and *Runx3*^{Tom} **(right)** animals showing recombination specificity in *Runx3*+ (red) subtypes, quantified below, n=4. **(B)** Proposed lineage tree of Prox2 and Runx3 neurogenesis. Phox2b+ nodose neurons are born during early development and first express Prox2 before largely separating into Prox2 and Runx3 subtypes. Thus, Runx3 neurons have a history of Prox2 expression and can be labeled with our intersectional strategy (*Runx3*^{Cre}*;Prox2*^{FlpO}). **(C)** Labeling strategy to mark Prox2 and Runx3 vagal neurons with tdTomato using

Prox2/Runx3^{Tom} (*Prox2*^{FlpO}*;Phox2b*^{Cre}*;Ai65*) mice. **(D)** Labeling strategy to mark Runx3 vagal neurons with tdTomato using *Runx3*^{Tom} (*Runx3*^{Cre}*;Prox2*^{FlpO}*;Ai65*) mice. Data are represented as mean ± SD.

Notice that while all Prox2 and Runx3 subtypes were recombined in *Prox2/Runx3*^{Tom} animals (Figure 15C), only the Runx3 subtypes were recombined in *Runx3*^{Tom} mice (Figure 15D). In summary, the generation and subsequent characterization of the novel *Prox2*^{FlpO} transgenic mouse strain provided us with a tool with which we could further interrogate the putative Prox2 and Runx3 vagal mechanoreceptors.

4.5. Testing recombination specificity by the use of *Prox2/Runx3*^{Tom} and *Runx3*^{Tom}

Next, we searched for additional recombination sites in *Prox2/Runx3*^{Tom} and *Runx3*^{Tom} animals. No recombination in either strain was observed in Phox2b+ hindbrain visceromotor nuclei (dorsal motor nucleus of the vagus and nucleus ambiguus), the locus coeruleus, or enteric ganglia (Figure 16A-E''). Recombination in sympathetic (superior cervical, stellate or sympathetic chain) and dorsal root ganglia (across the cervical, thoracic and lumbar levels) in both *Prox2/Runx3*^{Tom} and *Runx3*^{Tom} animals was exceedingly rare (less than ~1%, Figure 16F-I'').

However, in *Prox2/Runx3*^{Tom} animals tdTomato expression was observed in 14±6% of neurons of the geniculate ganglia, compared with 4±1% tdTomato expression in *Runx3*^{Tom} animals (Figure 17A,B). As geniculate neurons are known to innervate taste buds in the tongue, we examined the circumvallate, foliate and fungiform papillae for tdTomato+ innervation. We found that all three types of taste buds, labeled with Ck8, were indeed innervated by tdTomato+ fibers that likely originate from the geniculate ganglia (Figure 17C).

Lastly, we found recombination in 15±2% of the neurons of a single sympathetic ganglion, the celiac ganglion, in *Prox2/Runx3*^{Tom}, but not *Runx3*^{Tom} animals (Figure 18A,B). Almost all recombined neurons in the celiac ganglion co-expressed tyrosine hydroxylase (TH) in both *Prox2/Runx3*^{Tom} and *Runx3*^{Tom} mice (97±1% and 100%, respectively; Figure 18B). In order to define the targets of the recombined celiac neurons, we performed immunofluorescence against tdTomato and TH in the digestive tract. Importantly, we did not find any co-labeled axons in the esophagus, sphincter or stomach, but we did find extensive double-positive projections in the

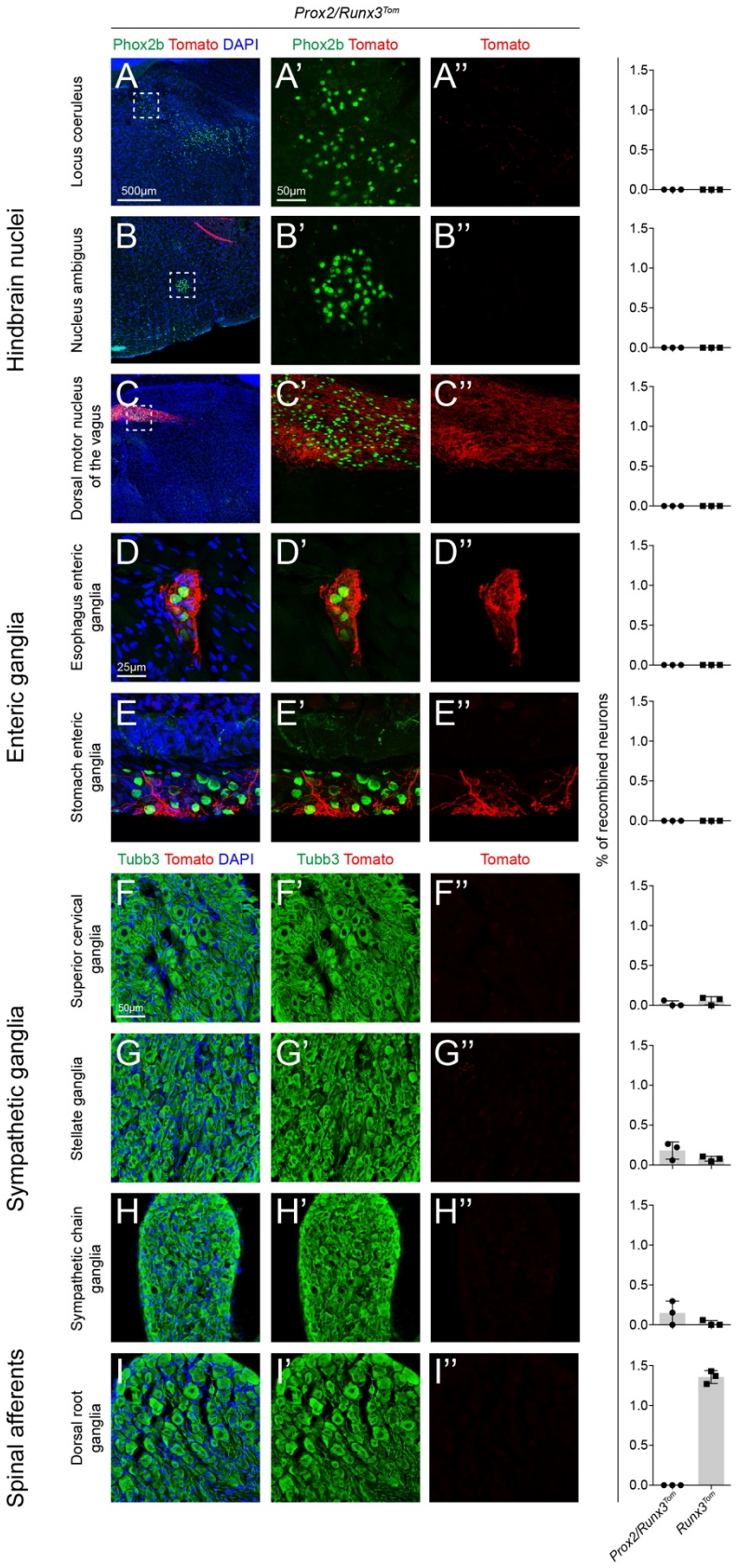
Prox2/Runx3Tom
Phox2b Tomato DAPI
Phox2b Tomato
Tomato
Hindbrain nuclei
Enteric ganglia
Sympathetic ganglia
Spinal afferents
Locus coeruleus
Nucleus ambiguus
Dorsal motor nucleus of the vagus
Esophagus enteric ganglia
Stomach enteric ganglia
Tubb3 Tomato DAPI
Tubb3 Tomato
Tomato
Superior cervical ganglia
Stellate ganglia
Sympathetic chain ganglia
Dorsal root ganglia
A
A'
A''
B
B'
B''
C
C'
C''
D
D'
D''
E
E'
E''
F
F'
F''
G
G'
G''
H
H'
H''
I
I'
I''
500µm
50µm
25µm
50µm
% of recombined neurons
1.5
1.0
0.5
0.0
Prox2/Runx3Tom
Runx3Tom

Figure 16. *Prox2/Runx3*^{Tom} and *Runx3*^{Tom} recombination specificity in hindbrain, enteric, sympathetic and dorsal root ganglia neurons. Immunohistology against Phox2b (green), tdTomato (red) and DAPI (blue) in the **(A)** locus coeruleus, **(B)** nucleus ambiguus, **(C)** dorsal motor nucleus of the vagus, **(D)** esophageal enteric ganglia and **(E)** stomach enteric ganglia in *Prox2/Runx3*^{Tom} animals. Quantifications (right) show that no Phox2b+ neurons were recombined in either *Prox2/Runx3*^{Tom} or *Runx3*^{Tom} mice, respectively, n=3. Immunohistology against Tubb3 (green), tdTomato (red) and DAPI (blue) in the **(F)** superior cervical, **(G)** stellate, **(H)** sympathetic chain and **(I)** dorsal root ganglia in *Prox2/Runx3*^{Tom} mice. Quantifications in *Prox2/Runx3*^{Tom} and *Runx3*^{Tom} mice (right) show the percentage of neurons recombined: 0.02±0.04% and 0.06±0.05% in superior cervical ganglia, 0.2±0.1% and 0.1±0.03% in stellate ganglia, 0.1±0.1% and 0.02±0.03% in sympathetic chain ganglia and 0±0% and 1.4±0.1% in dorsal root ganglia pooled from cervical, thoracic and lumbar levels, respectively, n=3. Data are represented as mean ± SD.

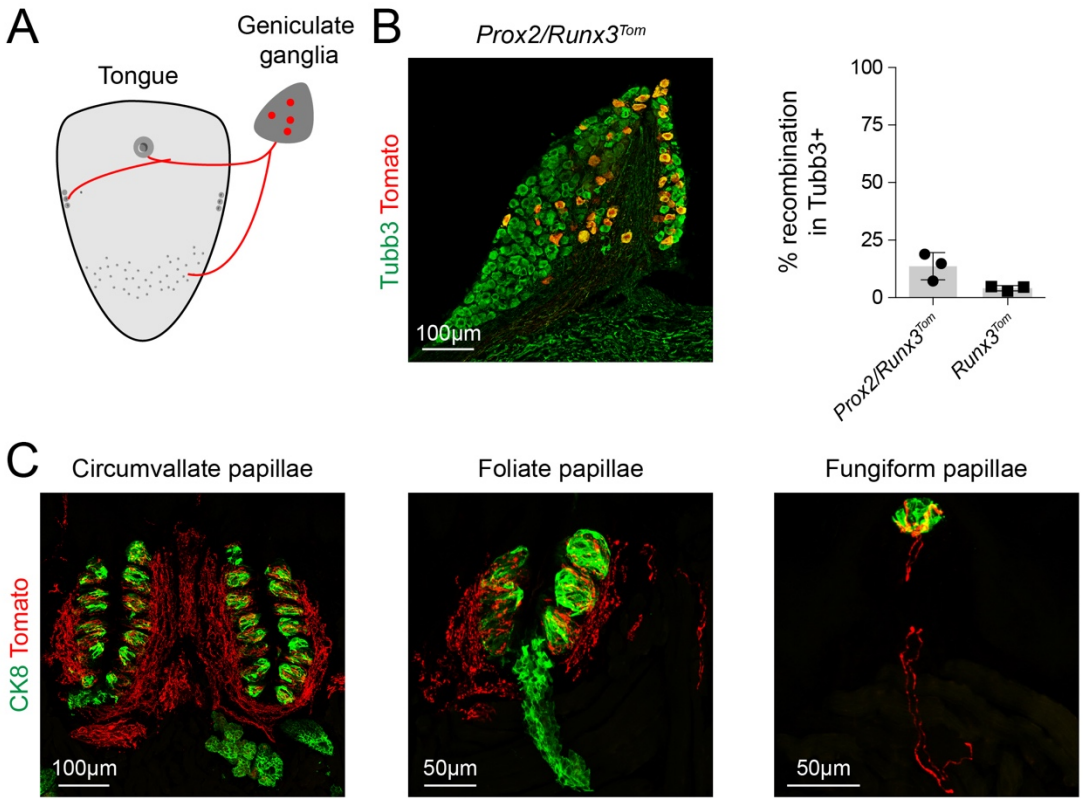

Figure 17. Prox2/Runx3 geniculate neurons innervate taste buds in the tongue. (A) Schema showing that Prox2/Runx3 geniculate neurons innervate the tongue. **(B)** Immunohistology **(left)** against tdTomato (red) and Tubb3 (green) shows recombination in geniculate neurons of a *Prox2/Runx3*^{Tom} animal. Quantifications **(right)** show that 14.1±6.1% and 4.1±1.1% of Tubb3+ neurons were recombined in *Prox2/Runx3*^{Tom} and *Runx3*^{Tom} mice, respectively, n=3. **(C)** Immunohistology against Ck8 (green) and tdTomato (red) shows tdTomato+ innervation of the cirumvallate, foliate, and fungiform papillae. Tongue illustration in A was adapted from bioicons.com (tongue, Servier) and licensed under CC-BY 3.0.

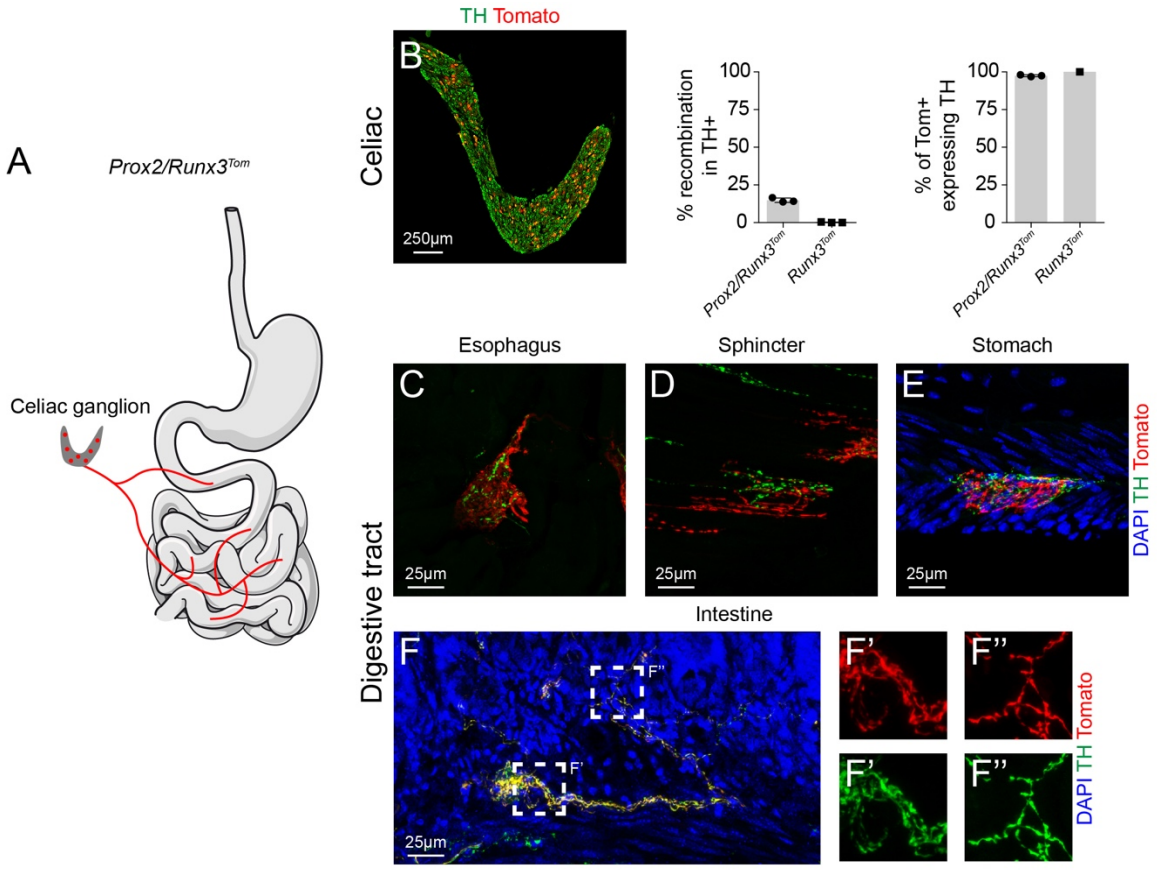

Figure 18. Prox2/Runx3 celiac neurons innervate the intestine. (A) Schema showing projections from Prox2/Runx3 celiac neurons to the intestine. **(B)** Immunohistology **(left)** against tdTomato (red) and TH (green) shows recombination in celiac neurons of a *Prox2/Runx3*^{Tom} animal. Quantifications **(right)** show that 14.9±1.5% and 0.2±0.3% of TH+ neurons were recombined in *Prox2/Runx3*^{Tom} and *Runx3*^{Tom} mice, respectively, n=3. Of the tdTomato+ recombined celiac neurons, 97.4±0.6% and 100% were TH+ in *Prox2/Runx3*^{Tom} and *Runx3*^{Tom} animals, respectively, n=3. Note that recombination was only observed in 1 out of 3 *Runx3*^{Tom} animals and all 8 recombined neurons were TH+. **(C-F)** Immunohistology against TH (green), tdTomato (red) and DAPI (blue) shows no co-localization in the **(C)** esophagus, **(D)** sphincter, or **(E)** stomach. **(F)** Immunohistology against TH (green), tdTomato (red) and DAPI (blue) shows extensive co-localization in the intestine. **(F', F'')** Magnifications of the boxed regions in F with TH (green) and tdTomato (red) shown separately. Digestive tract illustration in A was adapted from bioicons.com (digestive-system, Servier) and licensed under CC-BY 3.0.

intestine (Figure 18C-F and Table 2). Thus, the recombined celiac neurons do not innervate the esophagus, sphincter or stomach, but rather the intestine.

We checked other internal organs for tdTomato expression and found that Prox2/Runx3 vagal neurons project to the airways (Figure 19A). Prox2/Runx3 neurons (tdTomato+, red) project to the larynx, where they innervate the Ck8+ epithelial layer (green) of the quadrangular membrane

and laryngeal mucosa (Figure 19B,C). They also innervate the laryngeal taste buds (Figure 19D). Lightsheet imaging of the lung from a P8 *Prox2^{FlpO};R26^{FTLG}* animal showed that Prox2/Runx3 neurons (tdTomato+, gray) project broadly to many sites in the lung (Figure 19E). Closer inspection of lung innervation in adult *Prox2/Runx3^{Tom}* mice showed tdTomato+ innervation of smooth muscle (Figure 19F, green) and neuroepithelial bodies (Figure 19G, green).

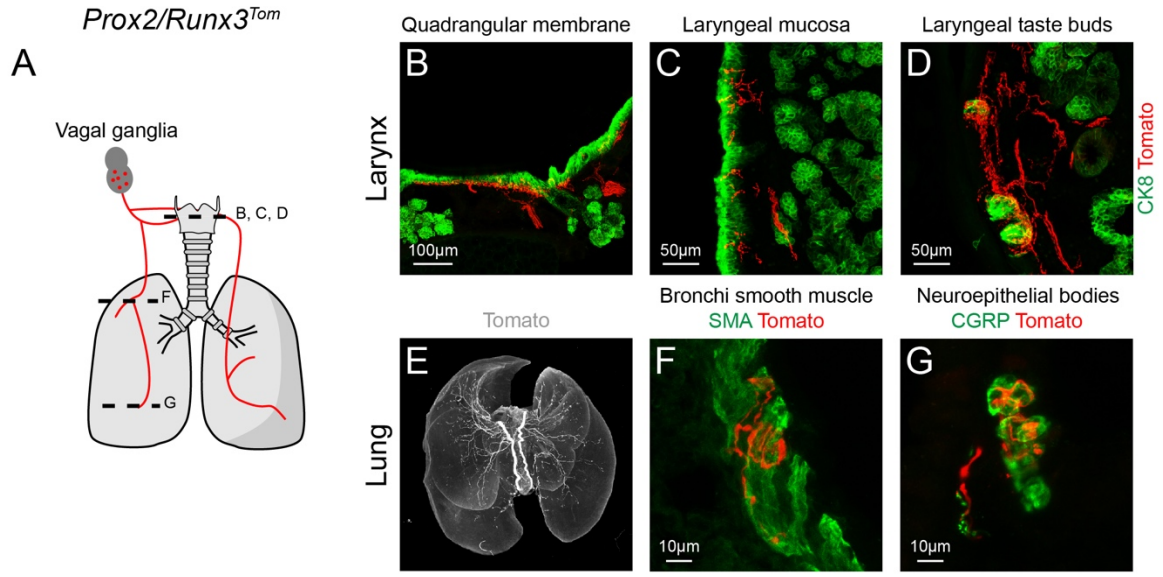

Figure 19. Prox2/Runx3 neurons project to the airways. (A) Schema showing projections from Prox2/Runx3 vagal neurons to the airways in *Prox2/Runx3^{Tom}* mice (*Prox2^{FlpO};Phox2b^{Cre};Ai65)*. **(B-D)** Immunohistology against Ck8 (green) and tdTomato (red) shows tdTomato+ innervation of the **(B)** quadrangular membrane of the larynx, **(C)** laryngeal mucosa, and **(D)** laryngeal taste buds. **(E)** Lightsheet imaging of tdTomato+ innervation of the lungs from a *Prox2^{FlpO};R26^{FTLG}* animal at P8. **(F)** Immunohistology against SMA (green) and tdTomato (red) shows tdTomato+ innervation of bronchi smooth muscle in the lung. **(G)** Immunohistology against CGRP (green) and tdTomato (red) shows tdTomato+ innervation of neuroepithelial bodies in the lung.

Examination of the heart in adult *Prox2/Runx3^{Tom}* animals showed tdTomato+ innervation of the aortic arch and aorta (Figure 20A-C).

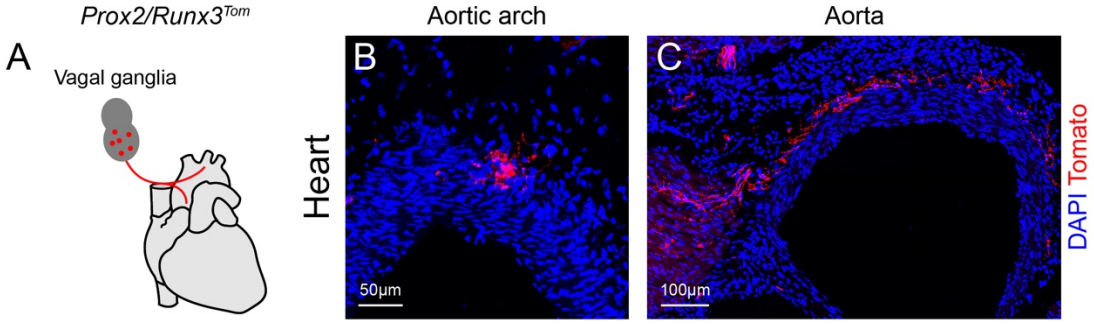

Figure 20. Prox2/Runx3 neurons project to the heart. (A) Schema showing projections from Prox2/Runx3 vagal neurons to the heart in *Prox2/Runx3^{Tom}* mice (*Prox2^{FlpO};Phox2b^{Cre};Ai65)*. **(B)** Immunohistology against tdTomato (red) and DAPI (blue) shows tdTomato+ innervation of the aortic arch. **(C)** Immunohistology against tdTomato (red) and DAPI (blue) shows tdTomato+ innervation of the aorta. Heart illustration in A was adapted from bioicons.com (heart-front, Servier) and licensed under CC-BY 3.0.

These vagal subtypes were recently characterized by others (Liu *et al.*, 2021; Min et al., 2019; Prescott *et al.*, 2020). Please see Table 1 for a summary of the recombination sites of Prox2/Runx3 neurons, and Table 2 for a summary of the innervation sites of recombined Prox2/Runx3 neurons.

4.6. Prox2/Runx3 neurons form IGLEs and rare IMAs in the upper gastrointestinal tract

We next investigated the innervation sites of Prox2/Runx3 vagal neurons in the upper gastrointestinal tract using immuno-labeling of tdTomato in *Prox2/Runx3^{Tom}* and *Runx3^{Tom}* adult mice. The esophagus and attached stomach were isolated, cleared and imaged using lightsheet microscopy (Susaki *et al.*, 2015; Voigt *et al.*, 2019). This demonstrated that the entire rostro-caudal axis of the esophagus was densely innervated by Prox2/Runx3 neurons, but only sparsely by Runx3 vagal neurons (Figure 21A). A magnification of the esophagus from the *Prox2/Runx3^{Tom}* animal showed that almost all Phox2b+ enteric ganglia were contacted by tdTomato+ fibers that displayed the morphology of IGLEs (Figure 21B). Magnifications of the glandular and non-glandular stomach also showed tdTomato+ IGLEs (Figure 21C,D), while in the non-glandular stomach tdTomato+ fibers displaying the morphology of IMAs were also found, but these were rare (Figure 21D, yellow arrowheads). Further, our lightsheet analysis of the stomach from a *Runx3^{Tom}* animal showed a higher density of innervation in the glandular than the non-glandular stomach, and also revealed non-glandular IMAs (Figure 21A).

To confirm that the endings found in the esophagus were IGLEs, we obtained thin esophageal sections from both *Prox2/Runx3^{Tom}* and *Runx3^{Tom}* adult mice and performed immunohistology to label the afferent fibers with tdTomato (red) and enteric neurons with Phox2b (green) (Figure 22A). Quantifications demonstrated that the vast majority of esophageal ganglia were contacted by tdTomato+ IGLEs in *Prox2/Runx3^{Tom}* mice, and rarely by tdTomato+ IGLEs in *Runx3^{Tom}* mice (Figure 22B). The difference in innervation was consistent across the cervical, thoracic and abdominal levels of the esophagus. Excitatory and inhibitory enteric motor neurons are defined by ChAT and Nos expression (Crist et al., 1984; Murray et al., 1991), respectively.

The tdTomato+ axons surrounded both ChAT+ excitatory and Nos+ inhibitory enteric motor neurons (Figure 22C).

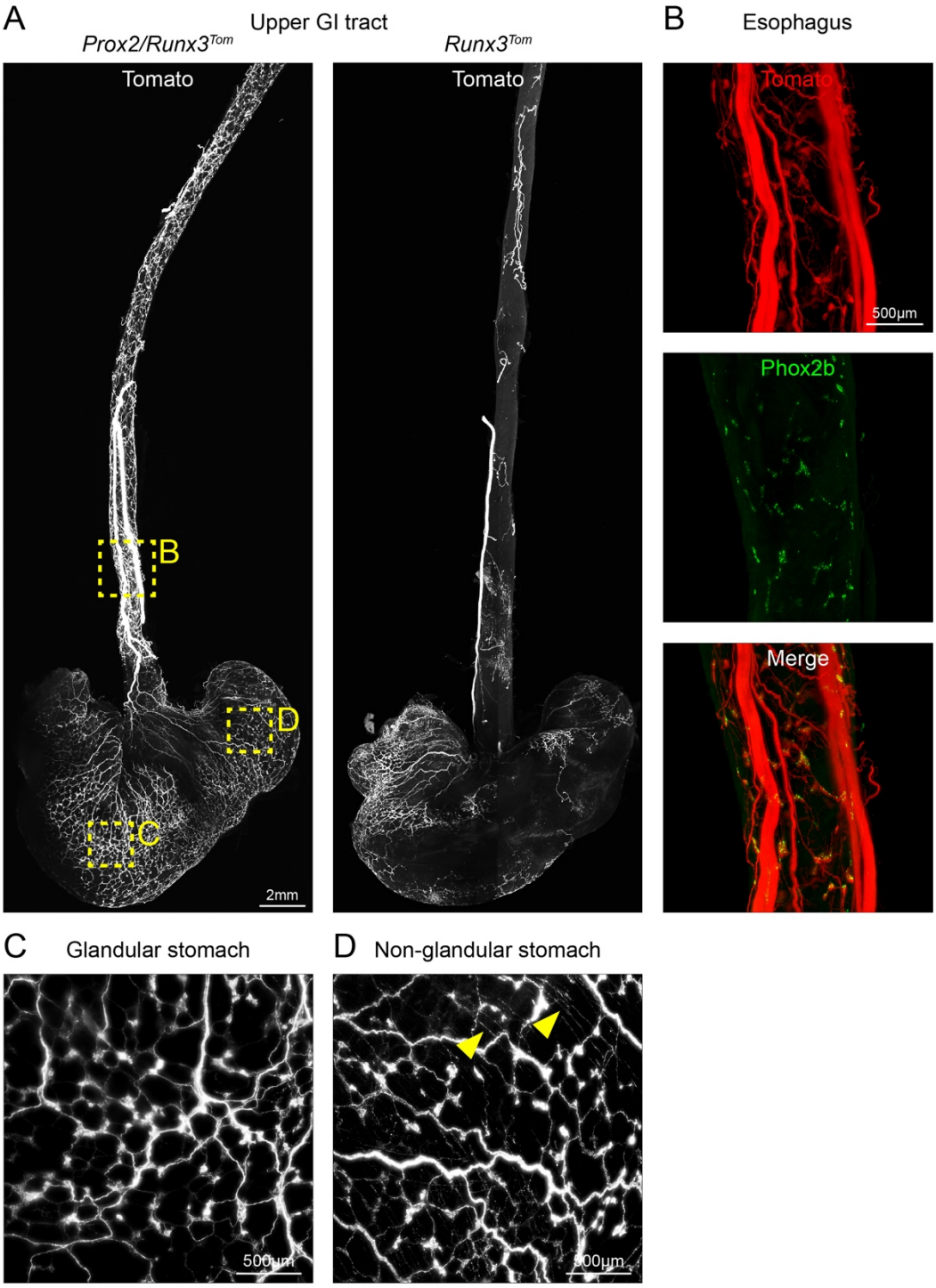

Figure 21. Lightsheet analysis reveals that Prox2/Runx3 neurons form IGLEs and IMAs in the upper gastrointestinal tract. (A) Lightsheet imaging (acquired with a mesoSPIM) of the attached esophagus and stomach from *Prox2/Runx3*^{Tom} mice (*Prox2*^{FlpO}*;Phox2b*^{Cre}*;Ai65)* **(left)** and *Runx3*^{Tom} animals (*Runx3*^{Cre}*;Prox2*^{FlpO}*;Ai65*) **(right)**

showing Tomato+ fibers (white) identified by immunohistology. **(B)** Magnification of the esophagus from the *Prox2/Runx3*^{Tom} animal shown in (A) and immunohistological analysis of Tomato+ fibers (red) and Phox2b+ enteric neurons (green). Note how all enteric neurons are contacted by Tomato+ IGLEs. **(C)** Magnification of the glandular stomach from the *Prox2/Runx3*^{Tom} animal shown in (A). **(D)** Magnification of the non-glandular stomach from the *Prox2/Runx3*^{Tom} animal shown in (A). Filled yellow arrowheads mark IMAs.

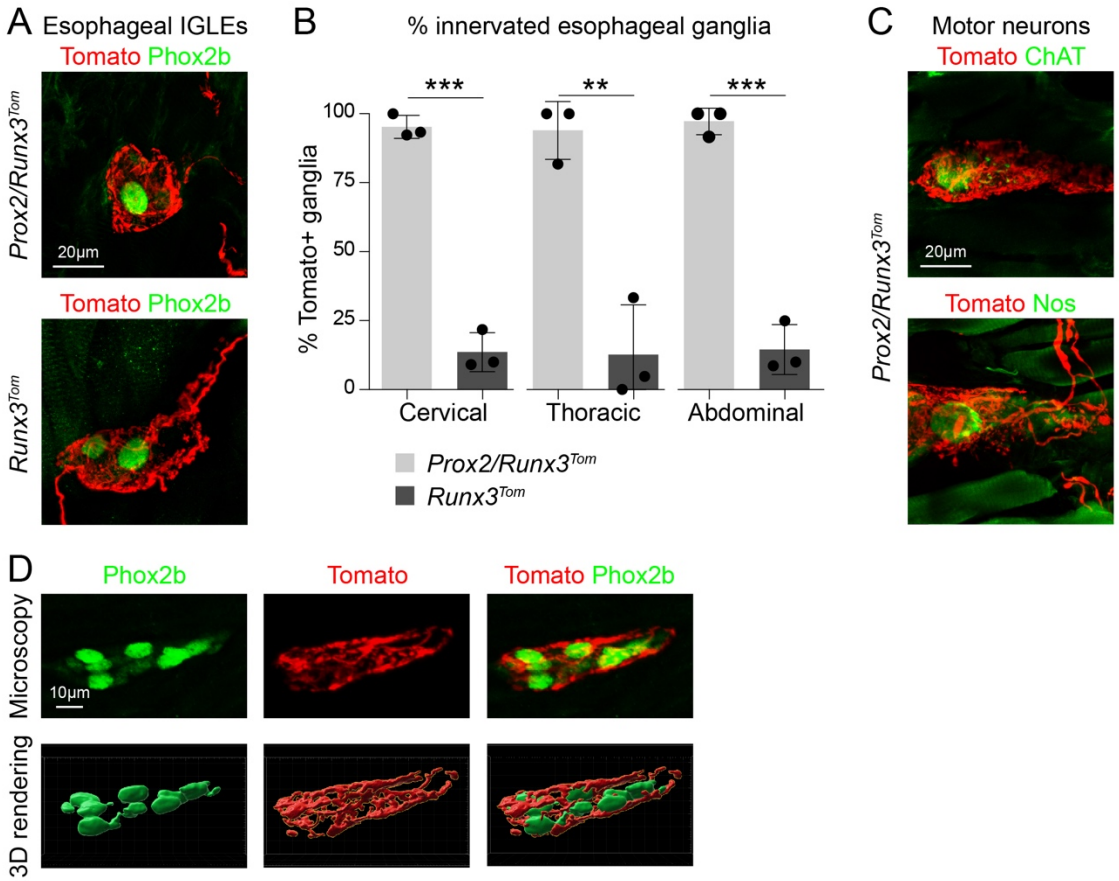

Figure 22. Prox2/Runx3 neurons form esophageal IGLEs. (A) Immunohistological analysis of esophageal IGLEs in *Prox2/Runx3*^{Tom} **(top)** and *Runx3*^{Tom} animals **(bottom)** using antibodies against tdTomato (red) and Phox2b (green). **(B)** Quantification of the proportion of esophageal enteric ganglia, identified by Phox2b immunohistology, innervated by tdTomato+ fibers in *Prox2/Runx3*^{Tom} and *Runx3*^{Tom} animals in the cervical (95.2±4.2% v. 13.6±7%, p=0.0003), thoracic (93.9±10.5% v. 12.7±18.0%, p=0.0053) and abdominal (97.2±4.8% v. 14.6±9.1%, p=0.0007) esophagus, n=3. **(C)** Immunohistological analysis of innervated excitatory **(top)** and inhibitory **(bottom)** esophageal enteric motor neurons in *Prox2/Runx3*^{Tom} animals using antibodies against tdTomato (red), ChAT (green, **top**) and nNos (green, **bottom**). **(D)** Immunohistological analysis of a tdTomato+ IGLE and Phox2b+ enteric neurons shown via confocal microscopy **(top)** and 3D rendering **(bottom)** from a *Prox2*^{FlpO}*;R26*^{FTLG} animal at P8. Data are represented as mean ± SD, **p<0.01, ***p<0.001, unpaired two-tailed t-test.

Lastly, we generated a 3D reconstruction of an IGLE and the associated Phox2b+ enteric ganglia from a *Prox2*^{FlpO};*R26*^{FTLG} animal at P8 (Figure 22D). This revealed that tdTomato+ endings formed a tight association around the enteric neurons, fully surrounding them. Thus, our histological analyses indicated that the esophagus was mainly innervated by Prox2 and, to a lesser extent, by Runx3 neurons, where they formed esophageal IGLEs.

Vagal neurons, and IGLEs, are classically thought of as pure sensory neurons that are afferent in nature (Raab and Neuhuber, 2007). The purely afferent nature of IGLEs was challenged by an electron microscopy study that found large, clear presynaptic vesicles within the IGLE opposite to esophageal enteric neurons (Neuhuber, 1987), and later studies from the same group found that IGLEs contained synaptophysin and VGlut2 (Raab and Neuhuber, 2003). We used an intersectional genetic strategy to label the synapses of Prox2/Runx3 neurons with SynaptophysinGFP using *Prox2/Runx3*^{SypGFP} (*Prox2*^{FlpO};*Phox2b*^{Cre};*R26*^{FTLG}) mice at P8 (Dempsey *et al.*, 2021). When we looked at the esophagus, we found that all GFP+ puncta co-expressed the presynaptic marker Synapsin 1, as well as VGlut2 (Figure 23).

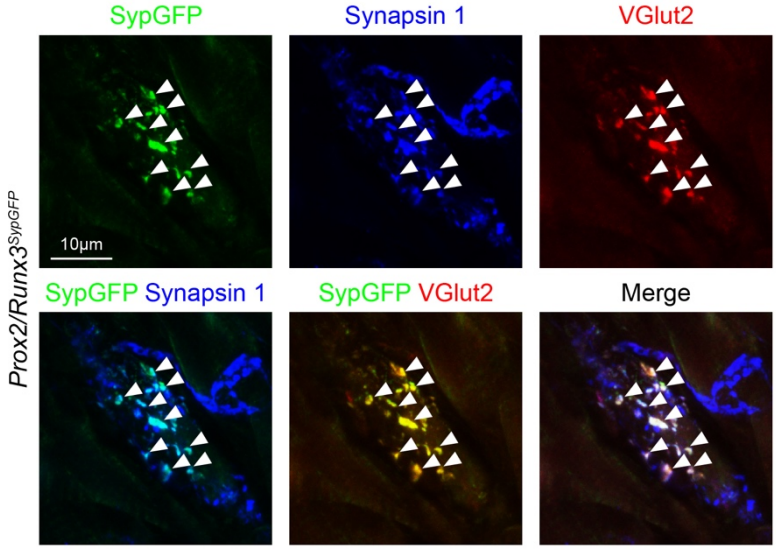

Figure 23. Prox2/Runx3 neurons contain presynaptic machinery in the esophagus. Immunohistological analysis of esophageal IGLEs in *Prox2/Runx3*^{SypGFP} mice at P8 shows SypGFP+ puncta (green) that co-localize with Synapsin 1 (blue) and VGlut2 (red). Filled white arrowheads label co-localization between the different proteins. Note that every SypGFP+ puncta expresses Synapsin 1 and VGlut2, and are thus likely presynaptic boutons.

Note that there are Synapsin1+ boutons that are neither VGlut2+ nor GFP+; these likely correspond to synapses from esophageal enteric neurons that neither express Prox2 nor use

glutamate as a neurotransmitter. Thus Prox2/Runx3 esophageal IGLEs contain presynaptic machinery, and may release glutamate from their peripheral terminals.

In order to confirm that the endings found in the stomach were IGLEs, we obtained thin stomach sections from both *Prox2/Runx3*^{Tom} and *Runx3*^{Tom} mice and performed immunohistology to label the afferent fibers with tdTomato (red) and enteric neurons with Phox2b (green) (Figure 24A).

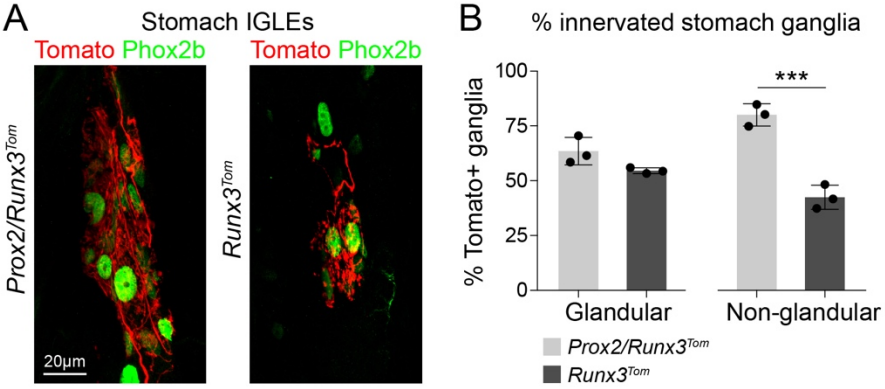

Figure 24. Prox2/Runx3 neurons form IGLEs in the stomach. (A) Immunohistological analysis of stomach IGLEs in *Prox2/Runx3*^{Tom} **(left)** and *Runx3*^{Tom} mice **(right)** using antibodies against tdTomato (red) and Phox2b (green). **(B)** Quantification of the proportion of stomach enteric ganglia, identified by Phox2b immunohistology, innervated by tdTomato+ fibers in *Prox2/Runx3*^{Tom} and *Runx3*^{Tom} animals in the glandular (63.5±6.3% v. 54.6±1.3%, p=0.127) and non-glandular (80.1±5.1% v. 42.5±5.5%, p=0.001) stomach, n=3. Data are represented as mean ± SD, ***p<0.001, unpaired two-tailed t-test.

Quantifications demonstrated that similar numbers of glandular stomach ganglia were contacted by tdTomato+ IGLEs in *Prox2/Runx3*^{Tom} and *Runx3*^{Tom} mice, but significantly more non-glandular stomach ganglia were contacted in *Prox2/Runx3*^{Tom} than in *Runx3*^{Tom} animals (Figure 24B). Thus both Prox2 and Runx3 neurons form gastric IGLEs, but Prox2 neurons preferentially innervate the non-glandular stomach and Runx3 neurons the glandular stomach. tdTomato+ axons (red) also made contacts with c-Kit+ interstitial cells of Cajal (green) in the lower esophageal sphincter of *Prox2/Runx3*^{Tom}, but not *Runx3*^{Tom} mice; these endings correspond to IMAs (Figure 25). Occasional tdTomato+ IMAs were detected in the stomachs of both *Prox2/Runx3*^{Tom} and *Runx3*^{Tom} mice, but these were rare (Figure 21A,D).

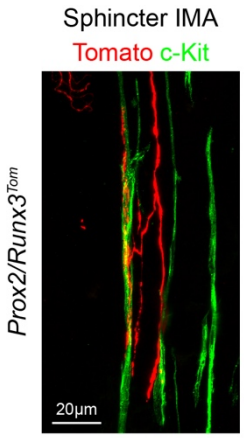

Figure 25. Prox2/Runx3 neurons form IMAs in the lower esophageal sphincter. Immunohistological analysis of IMAs in *Prox2/Runx3*^{Tom} animals showing tdTomato+ fibers (red) and c-Kit+ interstitial cells of Cajal (green).

Previous work has shown that *Oxtr* and *Glp1r* are expressed in subtypes of vagal neurons that project to the gastrointestinal tract and end as IGLEs, whereas *Gpr65* is expressed in neurons that project to the villi and detect nutrients (Bai *et al.*, 2019; Williams *et al.*, 2016).

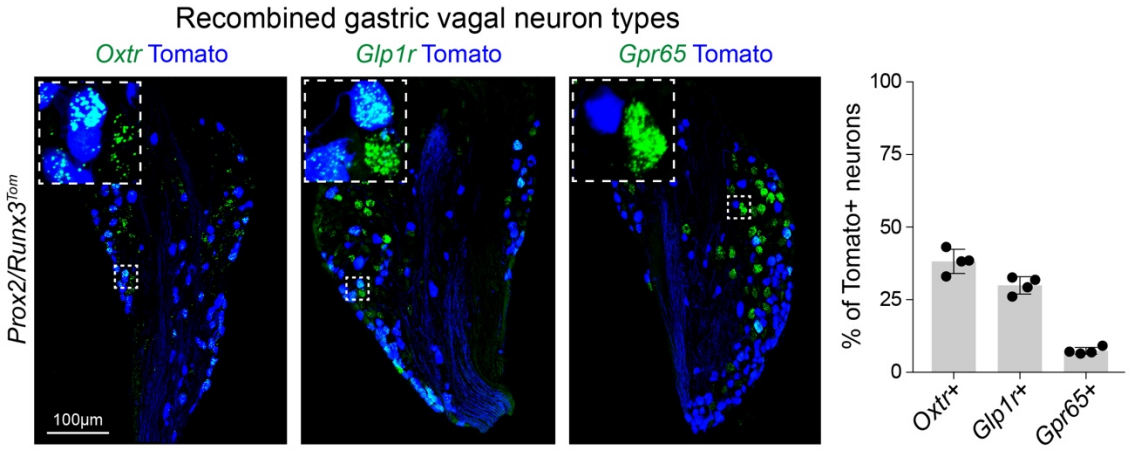

Figure 26. Prox2/Runx3 neurons express markers of vagal IGLEs. (Left) Representative images from smFISH experiments against *Oxtr*, *Glp1r* and *Gpr65* mRNA (green) and immunohistological analysis of tdTomato (blue) in *Prox2/Runx3*^{Tom} mice. **(Right)** Quantifications showing the percent of tdTomato+ neurons that express *Oxtr*, *Glp1r* and *Gpr65*, n=4. Data are represented as mean ± SD.

Using smFISH against *Oxtr*, *Glp1r* and *Gpr65* mRNA (green), combined with immunohistology against tdTomato (blue) in *Prox2/Runx3*^{Tom} animals, we found that many Prox2/Runx3 neurons co-expressed *Oxtr* and *Glp1r*, but rarely *Gpr65* (Figure 26). Therefore Prox2/Runx3 neurons express genes shown to label IGLEs, but not genes that label mucosal afferents.

4.7. Prox2/Runx3 neurons project centrally to the NTS and DMV

To define the synaptic connectivity of Prox2/Runx3 vagal neurons to second order sensory neurons in the nucleus of the solitary tract, we labeled their synapses with SynaptophysinGFP using *Prox2/Runx3*^{SypGFP} (*Prox2*^{FlpO};*Phox2b*^{Cre};*R26*^{FTLG} mice (Dempsey *et al.*, 2021); see Figure 27A for a schema of the FTLG allele). This approach revealed many GFP+ synaptic boutons on Phox2b+ neurons in the nucleus of the solitary tract (NTS) (Figure 27A).

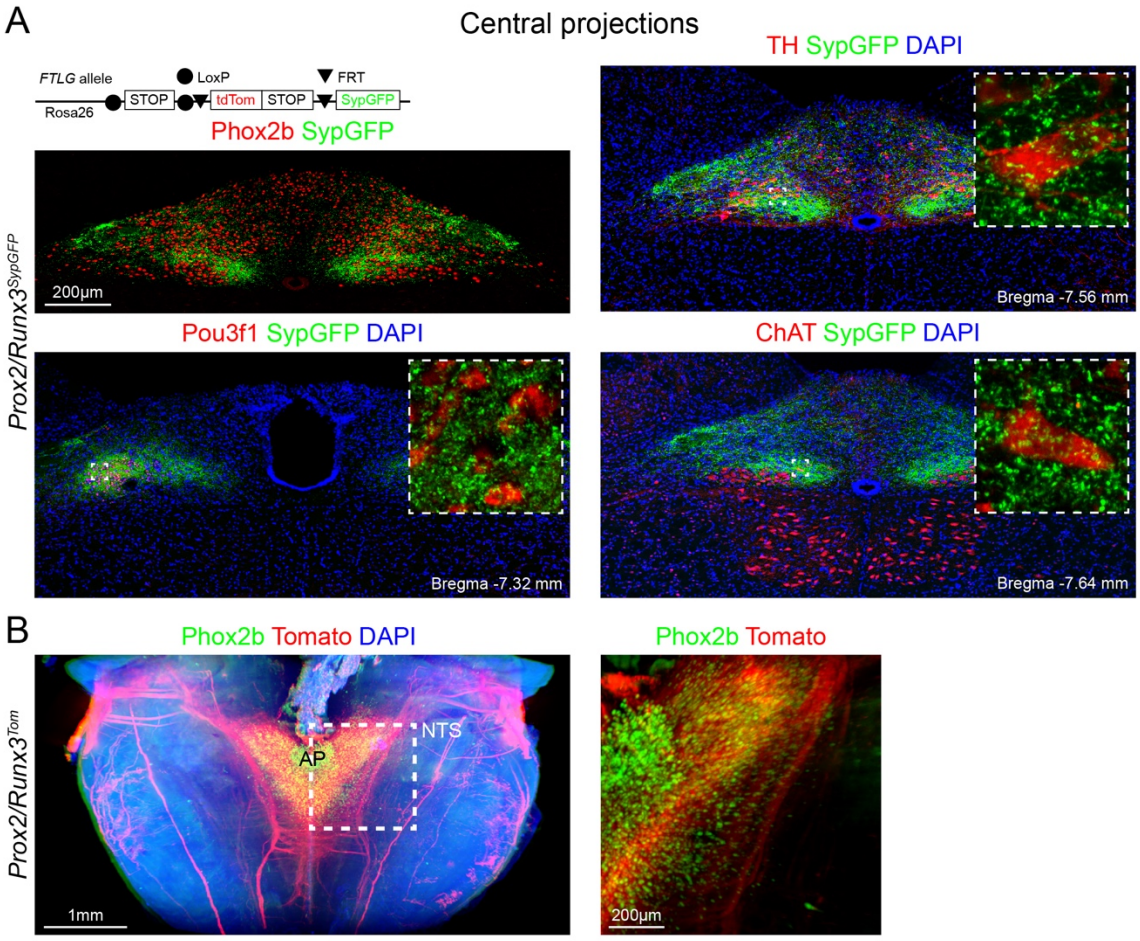

Figure 27. Prox2/Runx3 neurons project centrally to the NTS and DMV. (A) Analysis of the central synaptic connectivity of Prox2/Runx3 neurons in the nucleus of the solitary tract (NTS). Scheme **(top left)** of the intersectional *FTLG* reporter allele used to label Prox2 and Runx3 synapses with Synaptophysin-GFP in *Prox2/Runx3*^{SypGFP} (*Prox2*^{FlpO};*Phox2b*^{Cre};*R26*^{FTLG}) mice (Dempsey *et al.*, 2021). Immunohistological analysis of animals showing dense GFP+ boutons (green) in the NTS **(top left)**, on Pou3f1+ (red, **bottom left**) and TH+ (red, **top right**) NTS neuronal subtypes, as well as on ChAT+ neurons (red, **bottom right**) of the dorsal motor nucleus of the vagus (DMV). **(B)** Lightsheet imaging of a cleared hindbrain and immunohistological analysis for tdTomato (red), Phox2b (green) and DAPI (blue) in a *Prox2/Runx3*^{Tom} animal. Area postrema (AP), and nucleus of the solitary tract (NTS) are labeled. Inset shows tdTomato+ fibers innervating the NTS, but not the AP.

Pou3f1+ and TH+ neurons in the NTS represent small populations of interneurons found in the central and ventral nuclei of the NTS, respectively, that were innervated by Prox2/Runx3 vagal neurons. Interestingly, we also found GFP+ boutons on ChAT+ neurons of the dorsal motor nucleus of the vagus. Thus, Prox2/Runx3 vagal neurons project to Pou3f1+ and TH+ neurons in the NTS, and directly to ChAT+ motorneurons in the DMV. Lightsheet imaging of the hindbrain from a *Prox2/Runx3*^{Tom} animal showed that Tomato+ fibers (red) contacted Phox2b+ neurons (green) throughout the rostral-caudal axis of the NTS, but did not innervate the area postrema (AP, Figure 27B).

4.8. Prox2/Runx3 subtypes MM1, MM2 and MM8 project to the upper gastrointestinal tract

Next, we aimed to identify putative mechanoreceptive neurons that innervate the upper gastrointestinal tract. We retrogradely labeled vagal sensory neurons projecting to various sites in the esophagus and stomach (cervical, thoracic and abdominal esophagus, glandular and non-glandular stomach; shown schematically in Figure 28A) by injections of Cholera Toxin b (CTb) and Fast Blue gavage (Bentivoglio et al., 1980; Stoeckel et al., 1977), and performed smFISH against *Piezo2* mRNA (Figure 28B, left, quantified on the right). Our retrograde labeling experiment allowed us to successfully identify putative vagal esophageal mechanoreceptors.

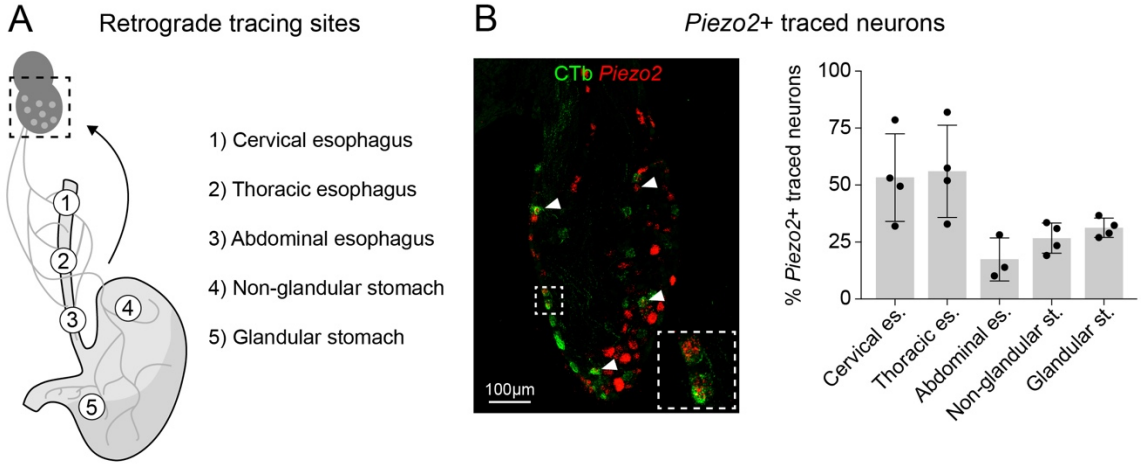

Figure 28. Retrograde tracing of *Piezo2*+ neurons from the upper gastrointestinal tract. (A) Retrograde tracing experiments; the scheme shows the five injection sites analyzed: 1 cervical esophagus, 2 thoracic esophagus, 3 abdominal esophagus, 4 non-glandular stomach, 5 glandular stomach. **(B)** smFISH **(left)** analysis using a *Piezo2* (red) probe, combined with immunohistological analysis of CTb (green) after CTb injection into the glandular stomach. **(Right)** quantification of *Piezo2*+ neurons identified after CTb or Fast Blue injection into various sites of the upper gastrointestinal tract. *Piezo2*+ neurons corresponded to 53.4±19.2%, 56.1±20.2%, 17.3±9.5%, 26.8±6.7%, and

31.3±4.3% of all neurons traced from the cervical, thoracic, abdominal esophagus, and non-glandular and glandular stomach, respectively, n=3-4. Note that neurons from the cervical and thoracic esophagus were traced using Fast Blue at P7, and neurons from the abdominal esophagus, non-glandular and glandular stomach were traced using CTb in adults. Data in are represented as mean ± SD. Retrograde tracing from the cervical and thoracic esophagus was performed by Huimin Li and Dr. Shiqi Jia at The First Affiliated Hospital, Jinan University.

Next we performed smFISH against *Piezo2* (blue), *Prox2* (green), *Runx3* (red) mRNA and immunohistology against CTB (gray) (Figure 29).

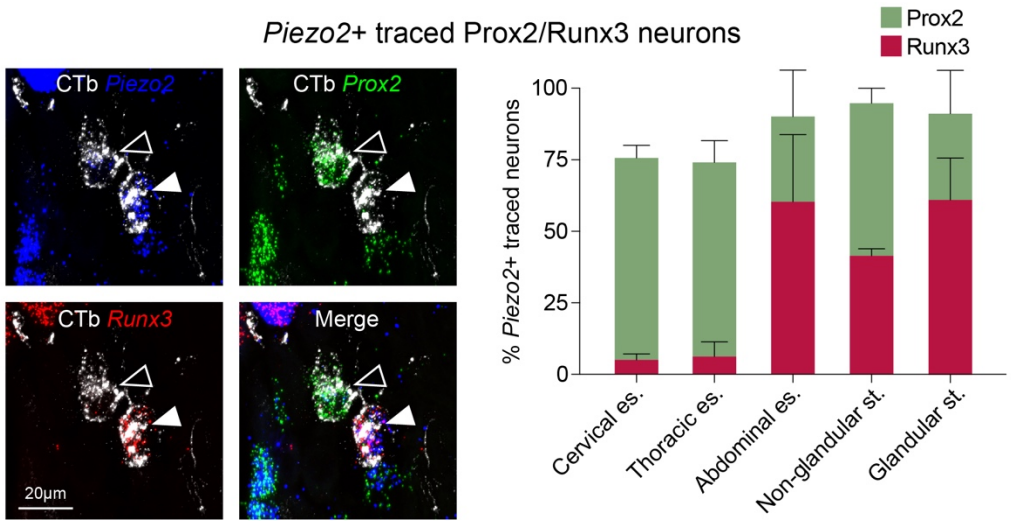

Figure 29. Most *Piezo2*+ vagal neurons that project to the upper gastrointestinal tract are Prox2/Runx3 neurons. Left, smFISH analysis of neurons after injection of CTb into the abdominal esophagus; probes used were *Prox2* (green), *Runx3* (red) and *Piezo2* (blue), which was combined with immunohistological analysis of CTb (gray). The open arrowhead marks a *Prox2*+*Piezo2*+CTb+ cell, and the filled arrowhead marks a *Runx3*+*Piezo2*+CTb+ cell. The proportions of the *Prox2*+*Piezo2*+ and *Runx3*+*Piezo2*+ neurons that were retrogradely labeled from the different injection sites are quantified on the **right**. Note that for technical reasons we used Fast Blue to trace from the cervical and thoracic esophagus in postnatal P7 mice, and CTb to trace from the abdominal esophagus and stomach in adult mice (see Methods for more details, n=3-5). *Runx3*+ neurons corresponded to 5.1±2.1%, 6.3±5.1%, 60.3±23.5%, 41.5±2.5%, and 61.1±14.6% of all *Piezo2*+ traced neurons traced from the cervical, thoracic, and abdominal esophagus, and from the non-glandular and glandular stomach, respectively. *Prox2*+ neurons corresponded to 70.6±4.4%, 67.8±7.6%, 29.8±16.2%, 53.4±5.2%, and 30.1±15.2% of all *Piezo2*+ neurons traced from the cervical, thoracic, and abdominal esophagus, and from the non-glandular and glandular stomach, respectively. Retrograde tracing from the cervical and thoracic esophagus was performed by Huimin Li and Dr. Shiqi Jia at The First Affiliated Hospital, Jinan University.

Overall, most traced *Piezo2*+ neurons from the upper gastrointestinal tract corresponded to the Prox2/Runx3 neuronal subtypes, i.e. ~75% from the cervical and thoracic esophagus and ~100% from the abdominal esophagus and stomach (Figure 29). The upper esophagus is innervated by both jugular and nodose neurons (Kwong et al., 2008), and we suggest that jugular neurons represent the remaining back-traced *Piezo2*+ cells that were both Prox2/Runx3-negative. Retrograde tracing experiments from the cervical and thoracic esophagus were performed by Huimin Li in the laboratory of Shiqi Jia at Jinan University in Guangzhou, China.

Further analysis demonstrated that the Prox2 MM1 and MM2 subtypes, as well as the Runx3 MM8 subtype correspond to the *Piezo2*+ neuronal subtypes innervating the esophagus and stomach (Figure 30A,B,C).

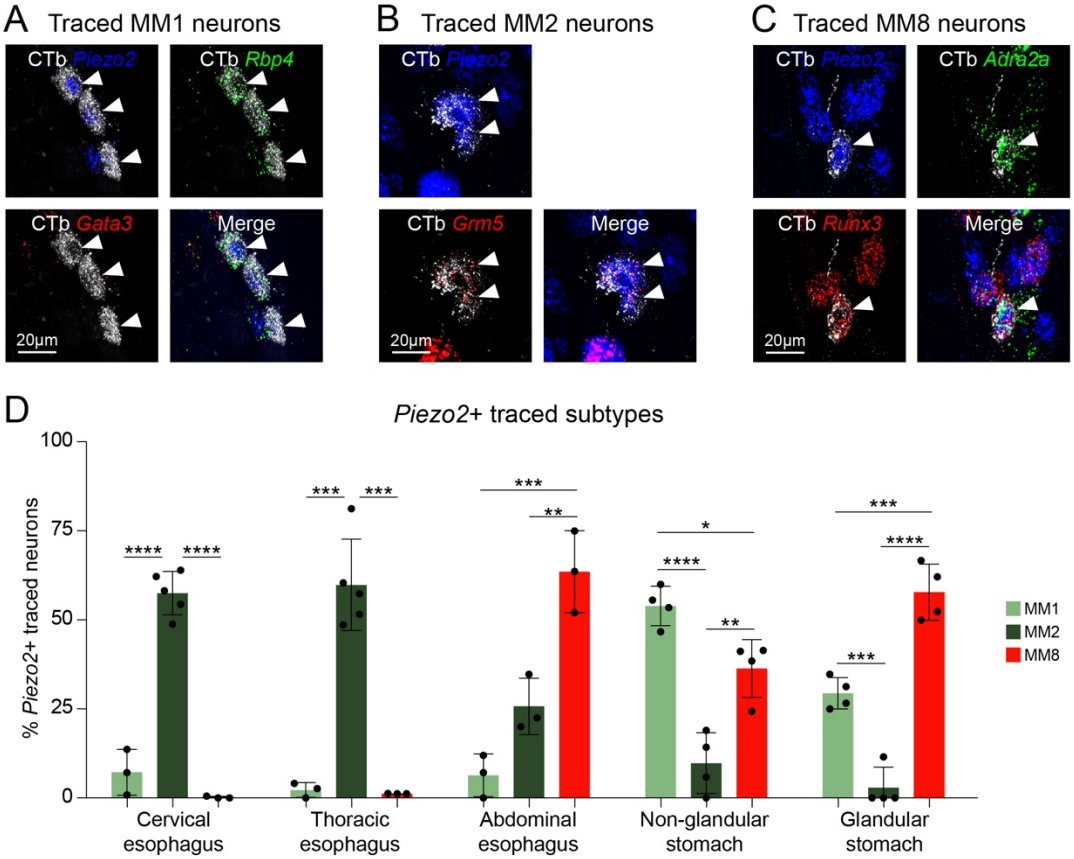

Figure 30. MM1, MM2 and MM8 neurons are the major subtypes of Prox2/Runx3 vagal neurons innervating the upper gastrointestinal tract. (A-C) smFISH analysis of traced MM1, MM2 and MM8 neurons. CTb (gray) was detected by immunohistology. For the identification of MM1 neurons **(A)**, we used probes against *Rbp4* (green), *Gata3* (red, negative marker) and *Piezo2* (blue) mRNA. To identify MM2 neurons **(B)**, we used probes against *Grm5* (green) and *Piezo2* (blue) mRNA. To identify MM8 neurons **(C)**, we used probes against *Adra2a* (green), *Runx3* (red) and *Piezo2* (blue) mRNA. **(D)** Quantification of traced MM1, MM2 and MM8 neurons from the five injection sites (n=3-

5). MM2 neurons were the dominant subtype traced from the cervical and thoracic esophagus (57.5±6.1% and 59.9±12.8%), with few MM1 (7.2±6.4% and 2.3±2.1%) and MM8 (0.2±0.3% and 1.3±0.03%) traced neurons. The abdominal esophagus was largely innervated by MM8 neurons (63.6±11.5%), with MM2 neurons contributing a substantial proportion (25.8±7.9%) and few MM1 neurons (6.4±6.0%). The non-glandular stomach was mostly innervated by MM1 neurons (53.93±5.6%), with a large contribution from MM8 neurons (36.4±8.1%) and few MM2 neurons (9.8±8.5%). The glandular stomach was largely innervated by MM8 neurons (57.8±7.9%), with a large contribution from MM1 (29.4±4.4%) and few MM2 neurons (2.9±5.8%). Data are represented as mean ± SD, *p<0.05, **p<0.01, ***p<0.001, ****p<0.0001, Ordinary one-way ANOVA with Tukey's multiple comparisons test.

These three subtypes displayed preferences in their regional innervation patterns. The cervical and thoracic esophagus was mainly innervated by the Prox2 MM2 neuronal subtype. MM2 neurons were less frequently traced from the abdominal esophagus and rarely from the stomach (Figure 30B,D). Instead, the related Prox2 neuronal subtype MM1 was more frequently traced from the stomach (Figure 30A,D). The Runx3 neuronal subtype MM8 was rarely traced from the cervical and thoracic esophagus, but more frequently from the abdominal esophagus and stomach (Figure 30C,D). We detected further regional differences in the stomach: MM8 and MM1 were more frequently traced from the glandular and non-glandular stomach, respectively (Figure 30D).

Previous work showed that *Glp1r*+ vagal neurons form gastric IGLEs (Williams *et al.*, 2016).

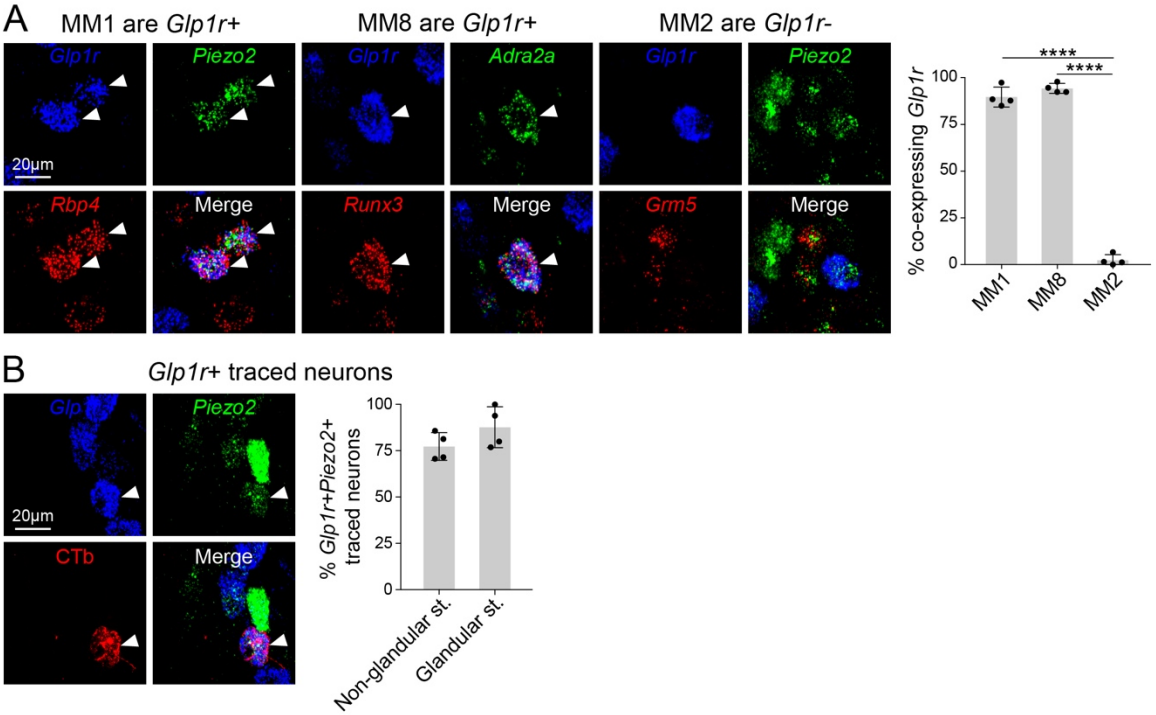

Figure 31. MM1 and MM8 are *Glp1r*+ stomach projecting neurons. (A) smFISH **(left)** analysis identifying MM1 neurons (probes: *Piezo2* in green, *Rbp4* in red, and *Glp1r* in blue) shows that 89.6±5.3% of MM1 neurons are *Glp1r*+, n=4. smFISH **(middle)** analysis identifying MM8 neurons (probes: *Adra2a* in green, *Runx3* in red, and *Glp1r* in blue) shows that 94.3±2.6% of MM8 neurons are *Glp1r*+, n=4. smFISH **(right)** for MM2 neurons (probes: *Piezo2* in green, *Grm5* in red, and *Glp1r* in blue) shows that most MM2 neurons are *Glp1r*-negative: only 2.4±3.0% of MM2 neurons expressed *Glp1r*, n=4. **(B)** smFISH analysis **(left)** of *Piezo2* (green) and *Glp1r* (blue) mRNA, combined with immunohistological analysis of CTb (red) after CTb injection into the glandular and non-glandular stomach; the quantification is shown on the **right**. *Glp1r*+ neurons corresponded to 77.3±7.4% and 87.7±11.0% of all *Piezo2*+CTb+ neurons traced from the non-glandular and glandular stomach, respectively, n=4. Data are represented as mean ± SD, ****p<0.0001, ordinary one-way ANOVA with Tukey's multiple comparisons test **(A)**, unpaired two-tailed t-test **(B).**

smFISH revealed extensive *Glp1r* expression in the stomach projecting MM1 (89.6±5.3%) and MM8 (94.3±2.6%) neurons, but the esophageal projecting MM2 neurons rarely expressed *Glp1r* (2.4±3.0%) (Figure 31A). Additionally, almost all *Piezo2*+ traced neurons from the non-glandular and glandular stomach were *Glp1r*+ (Figure 31B). In summary, retrograde tracing and histological analyses show that the MM1, MM2 and MM8 subtypes innervate the esophagus and stomach where they end as IGLEs. These subtypes display regional innervation preferences and, in particular, the esophagus is mainly innervated by the Prox2 MM2 neuronal subtype.

4.9. Prox2/Runx3 vagal neurons that project to the upper gastrointestinal tract are mechanoreceptors

We next investigated the electrophysiological properties of Prox2/Runx3 neurons using an *in vitro* open book vagus-esophagus preparation (Figure 32A) to record mechanically evoked responses from single nerve fibers that innervate the thoracic and abdominal esophagus (Page and Blackshaw, 1998; Page *et al.*, 2002).

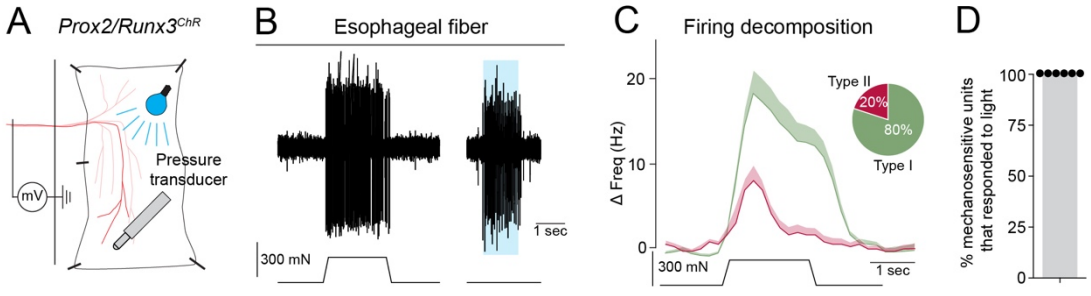

Figure 32. Prox2/Runx3 vagal neurons are esophageal mechanoreceptors. (A) Scheme of the open book esophagus-vagus nerve *in vitro* preparation used for electrophysiological analysis. Teased fibers from the vagus nerve

of *Prox2/Runx3*^{ChR} (*Prox2*^{FlpO}*;Phox2b*^{Cre}*;Ai80*) mice were placed on a recording electrode, and the identity of Prox2/Runx3-positive units expressing channelrhodopsin was identified by light stimulation. Esophageal mechanosensitive receptive fields were found by probing the tissue with a blunt glass rod and then a piezo actuator. **(B)** Representative traces of a vagus nerve fiber responding to mechanical stimuli; the intensity of the mechanical stimulus is indicated below (**Left**, 250 mN; **right**, 0 mN). Note that this fiber also responded to blue light applied to the receptive field, demonstrating that it contained Prox2/Runx3-positive units. **(C)** Decomposition of Prox2/Runx3-positive unit firing patterns revealed two types of mechanosensory neurons that differed in their adaptation properties. The firing of 80% of the recorded Prox2/Runx3-positive units decayed after the end of the stimulus and had a peak of 20Hz (type I, green), whereas in the remaining 20% firing decayed during the stimulus and had a peak of 7Hz (type II, red). **(D)** Quantification of the proportion of Prox2/Runx3-positive units (30/30) among all mechanosensitive units in the esophagus; note that all mechanosensitive fibers were Prox2/Runx3-positive units, n=6 mice. Data are represented as mean ± SEM **(C)** or mean ± SD **(D)**. All the experiments shown in this figure were performed by Dr. Pierre-Louis Ruffault in the laboratory of Prof. Dr. Gary Lewin.

For this, *Prox2/Runx3*^{ChR} (*Prox2*^{FlpO}*;Phox2b*^{Cre}*;Ai80*) mice that express channelrhodopsin specifically in Prox2/Runx3 vagal neurons were used (Daigle *et al.*, 2018). Neurons were classified as Prox2/Runx3-positive or -negative based on whether or not they fired action potentials in response to blue light (Figure 32B). Firing patterns evoked by light and mechanical stimuli had similar magnitude and kinetics (Figure 32B). Analysis of single unit responses to mechanical stimuli revealed two distinct response patterns. The majority of the Prox2/Runx3-positive mechanoreceptors (80%) showed sustained firing of up to 20Hz during mechanical stimulation, and firing frequency slowly returned to baseline after the end of the stimulation (we call these type I esophageal receptors, Figure 32C). The remaining 20% showed peak firing of around 7Hz that rapidly returned to baseline before the end of the stimulus (we call these type II esophageal receptors, Figure 32C). Interestingly, all mechanically sensitive neurons tested in the thoracic and abdominal esophagus responded to blue light (30/30 neurons, n = 6 mice), indicating that Prox2/Runx3-positive neurons are the sole vagal mechanoreceptors at these sites (Figure 32D). In summary, Prox2/Runx3-positive neurons form esophageal IGLEs and function as low-threshold mechanoreceptors. These neurons segregate into an abundant type I and a less abundant type II receptor that differ in their adaptation rates, and peak firing frequency.

In addition, we used an *in vitro* vagus-stomach preparation (Figure 33A), and administered physiological volumes of saline (0.1-0.3 ml) as a mechanical stimulus to distend the stomach (Kim et al., 2020; Williams *et al.*, 2016). As in our esophagus prep, neurons were classified as

Prox2/Runx3-positive or -negative based on whether or not they fired action potentials in response to blue light (Figure 33B). Firing patterns evoked by light and mechanical stimuli had similar magnitude and kinetics (Figure 33B).

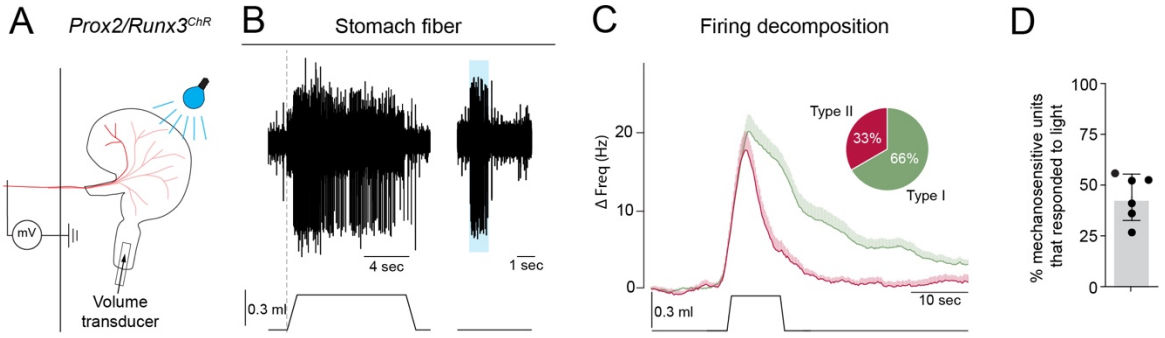

Figure 33. Prox2/Runx3 neurons are gastric mechanoreceptors. (A) Scheme of the stomach-vagus nerve *in vitro* preparation. In order to mimic physiological distension, the stomach was kept intact and a catheter was inserted into the pyloric sphincter. Stomach distension was induced by injecting 0.1, 0.2 or 0.3 ml of a saline solution through the catheter into the stomach. **(B)** Traces recorded from a vagus nerve fiber responding to distention stimuli, i.e. 0.3 ml stimuli, and to light stimulation. **(C)** Decomposition of Prox2/Runx3-positive unit firing patterns revealed two types. All units responded rapidly to stomach distention, but differed in their firing adaptation. Type I units (66%, green) were slowly adapting units that returned to basal activity after stimulus offset. Firing of type II units (33%, red) decayed during the duration of the stimulus. **(D)** Quantification of the proportion of Prox2/Runx3-positive units among all mechanosensitive units in the stomach (55/125, n=6 mice). Data are represented as mean ± SEM **(C)** or mean ± SD **(D)**. All the experiments shown in this figure were performed by Dr. Pierre-Louis Ruffault in the laboratory of Prof. Dr. Gary Lewin.

Closer examination of Prox2/Runx3-positive mechanosensitive firing responses uncovered two distinct types (Figure 33C). While both types increased their firing frequency at the onset of stomach distension, they differed in their adaptation properties. Type I gastric receptors continued firing while the stomach was distended and only returned to basal activity after the stomach had emptied, while type II gastric receptors reduced their firing frequency and returned to basal activity even while the stomach was still distended (Figure 33C). Around half of all distention-sensitive neurons were light-sensitive and thus corresponded to Prox2/Runx3-positive neurons (55/125 neurons, n = 6 mice; Figure 33D). Together, our *in vitro* studies demonstrate that Prox2/Runx3-positive gastric vagal neurons are mechanosensitive. Type I gastric receptors appear to detect static stretch or volume, and type II receptors the dynamic changes in stretch or tension. All of the electrophysiology experiments described in this section (4.9.) were performed by Pierre-Louis

Ruffault (postdoctoral fellow in AG C. Birchmeier) using equipment in the laboratory of Gary Lewin.

4.10. Ablation of Prox2/Runx3 vagal neurons results in esophageal dysmotility

We used a similar intersectional genetic strategy as the one described above to express the diphtheria toxin receptor (DTR) in Prox2/Runx3 neurons (*Prox2^{FlpO};Phox2b^{Cre};Tau$^{ds\text{-}DTR}$*, hereafter called *Prox2/Runx3$^{ds\text{-}DTR}$* mice) (Britz *et al.*, 2015). DTR expressing neurons were ablated by injecting diphtheria toxin (DT), and the ablation efficacy and specificity was determined using smFISH and IF two weeks after DT injection (Figure 34).

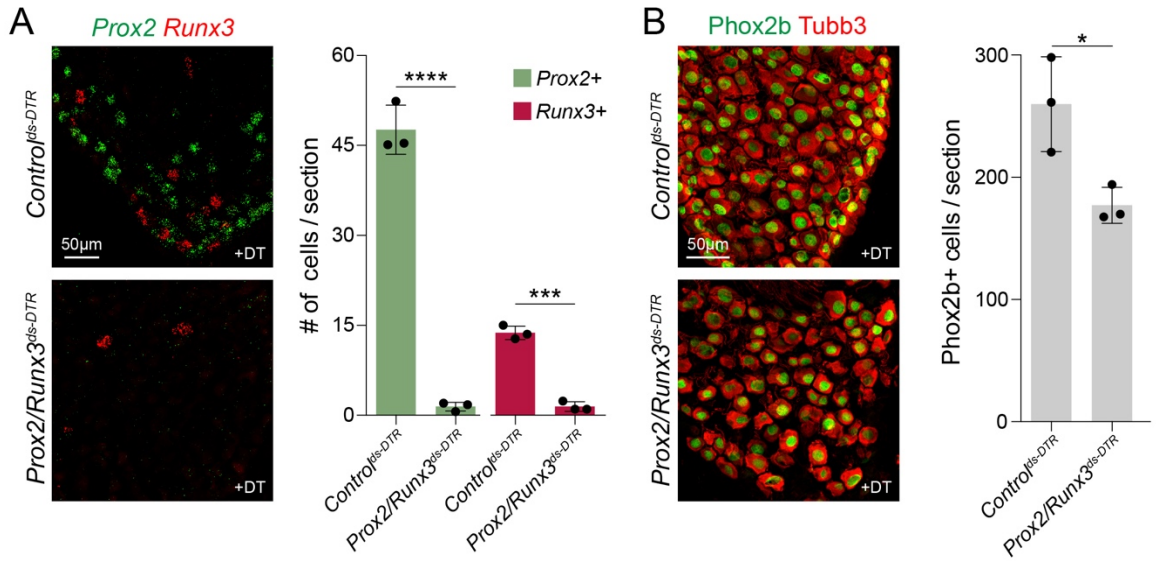

Figure 34. Successful ablation of Prox2/Runx3 vagal neurons. (A) Representative smFISH images **(left)** against *Prox2* (green) and *Runx3* (red) mRNA in adult *Control$^{ds\text{-}DTR}$* (**top**, *Prox2^{FlpO};Tau$^{ds\text{-}DTR}$*) and *Prox2/Runx3$^{ds\text{-}DTR}$* (**bottom**, *Prox2^{FlpO};Phox2b^{Cre};Tau$^{ds\text{-}DTR}$*) mice 14 days after DT administration. The number of *Prox2*+ and *Runx3*+ neurons before and after ablation are quantified on the right, n=3. The number of *Prox2*+ neurons per section decreased from 47.6±4.1 in *Control$^{ds\text{-}DTR}$* to 1.5±0.7 in *Prox2/Runx3$^{ds\text{-}DTR}$* mice (p<0.0001), while the number of *Runx3*+ neurons per section decreased from 13.8±1.1 in *Control$^{ds\text{-}DTR}$* to 1.5±0.8 in *Prox2/Runx3$^{ds\text{-}DTR}$* mice (p=0.0001). **(B)** Representative immunofluorescence images **(left)** against Phox2b (green) and Tubb3 (red) in adult *Control$^{ds\text{-}DTR}$* (**top**) and *Prox2/Runx3$^{ds\text{-}DTR}$* (**bottom**) mice 14 days after DT administration. The number of Phox2b+ neurons before and after ablation are quantified on the right, n=3. The number of Phox2b+ neurons per section was 260.0±38.8 in *Control$^{ds\text{-}DTR}$* and 177.2±14.7 in *Prox2/Runx3$^{ds\text{-}DTR}$* mice (p=0.0259). Data are represented as mean ± SD, *p<0.05, ***p<0.001, ****p<0.0001, unpaired two-tailed t-test.

As the DTR receptor is only expressed after the removal of both lox-flanked and frt-flanked stop cassettes, DT-treated *Prox2*^{FlpO}*;Tau*$^{ds\text{-}DTR}$ animals were used as controls (called *Control*$^{ds\text{-}DTR}$). This showed that 97±3% and 90±5% of *Prox2*+ and *Runx3*+ neurons, respectively, were ablated in the vagal ganglia of *Prox2/Runx3*$^{ds\text{-}DTR}$ animals (Figure 34A).

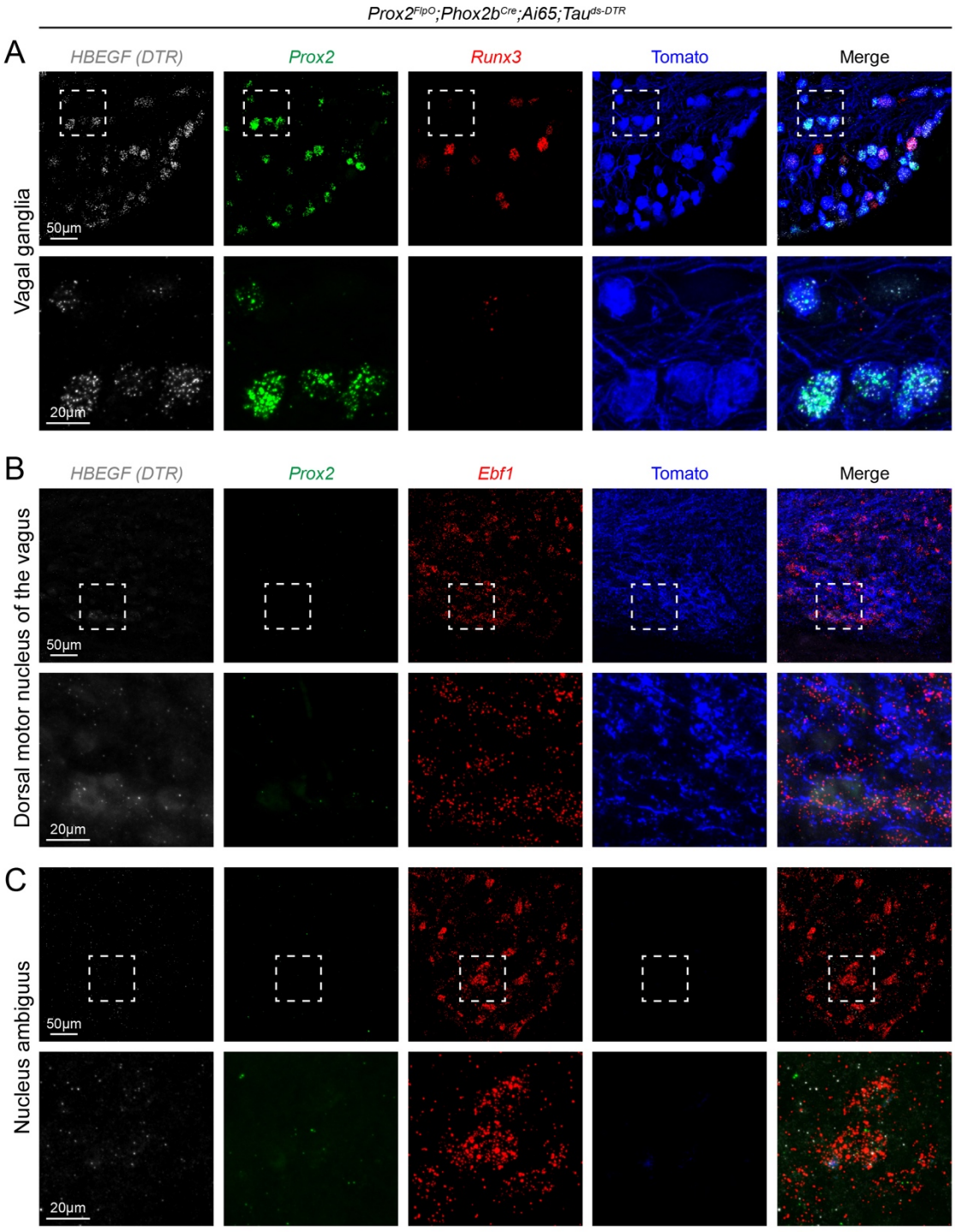

Figure 35. *DTR* (*HBEGF*) expression in the vagal ganglia and hindbrain of *Prox2/Runx3*$^{ds\text{-}DTR}$ animals. (A) RNAscope analysis of vagal ganglia using probes specific for *DTR* (*HBEGF*, white), *Prox2* (green), *Runx3* (red); tdTomato was detected using immunohistology and is shown in blue. Dotted boxes are shown magnified below. tdTomato+ vagal neurons express either *Prox2* or *Runx3* together with *DTR (HBEGF)*. **(B)** RNAscope analysis of the dorsal motor nucleus of the vagus using probes specific for *DTR* (*HBEGF*, white), *Prox2* (green), *Ebf1* (red); tdTomato was detected using immunohistology and is shown in blue. Dotted boxes are shown magnified below. tdTomato+ vagal neurons project to the nucleus of the solitary tract and dorsal motor nucleus of the vagus as shown in Figures 13 and 24. Although some dorsal motor nucleus of the vagus neurons express *Ebf1*, there is no expression of *Prox2* or *DTR (HBEGF)*. **(C)** RNAscope analysis of the nucleus ambiguus using probes specific for *DTR* (*HBEGF*, white), *Prox2* (green), *Ebf1* (red); tdTomato was detected using immunohistology and is shown in blue. Dotted boxes are shown magnified below. There are no tdTomato+ vagal neuron projections to the nucleus ambiguus as shown in Figure 13. Although some nucleus ambiguus neurons express *Ebf1,* there is no expression of *Prox2* or *DTR (HBEGF)*.

The scRNAseq data showed that Prox2/Runx3 neurons represent around 30% of all Phox2b+ vagal neurons. In accordance, 32±6% of Phox2b+ neurons were ablated after DT injection (Figure 34B).

As an additional control, we tested for the expression of the diphtheria toxin receptor (*HBEGF*) in the dorsal motor nucleus of the vagus, nucleus ambiguus and vagal ganglia in *Prox2/Runx3*$^{ds\text{-}DTR}$ (*Prox2*^{FlpO}*;Phox2b*^{Cre}*;Ai65;Tau*$^{ds\text{-}DTR}$) mice (Figure 35). Many tdTomato+ cells (blue) were found in the vagal ganglia, where they co- expressed *Prox2* (green) or *Runx3* (red) together with *HBEGF* (white) mRNA (Figure 35A, dotted boxes are shown magnified below). However, we did not find any expression of either *Prox2* (green) or *HBEGF* (white) in the dorsal motor nucleus of the vagus or in the nucleus ambiguus (Figure 35B,C, dotted boxes are shown magnified below). As in Figure 16, no hindbrain neurons were tdTomato+, although you can see tdTomato+ projections from Prox2/Runx3 vagal neurons to the NTS and DMV (Figure 35B). Note that we used the transcription factor *Ebf1* to label neurons in the DMV and NA (Muller et al., 2003; Pattyn et al., 2000). We conclude that in *Prox2/Runx3*$^{ds\text{-}DTR}$ animals the diphtheria toxin receptor was only expressed in Prox2/Runx3 neurons, and not in hindbrain motor nuclei such as the DMV or NA where Prox2 is not expressed.

Following administration of DT, the animals' weights were monitored daily, which revealed that *Prox2/Runx3*$^{ds\text{-}DTR}$, but not *Control*$^{ds\text{-}DTR}$ mice, rapidly lost weight in the first five days post ablation (Figure 36A). *Prox2/Runx3*$^{ds\text{-}DTR}$ animals received a high caloric diet and daily saline injections after ablation, which helped to stabilize their weight loss at about -12% of the starting weight (Figure 36A). In order to examine the role of Prox2/Runx3 neurons in swallowing

we performed VFSS 2 days before and 19 days after ablation (see Figure 36B for an experimental timeline, and Videos 1 and 2) (Lever *et al.*, 2015).

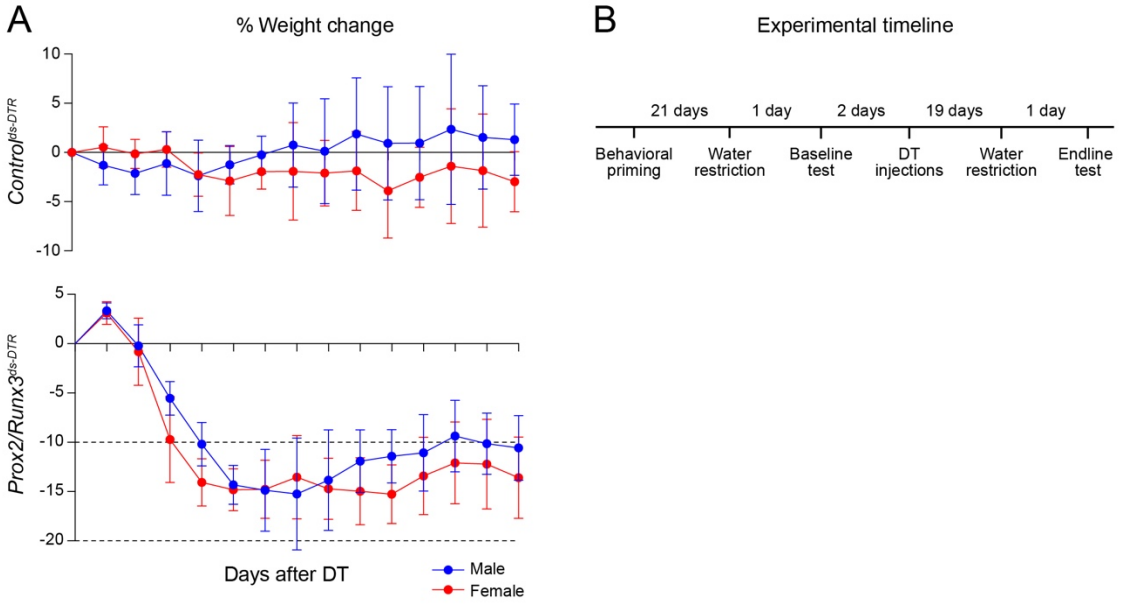

Figure 36. Ablation of Prox2/Runx3 neurons leads to a reduction in bodyweight. (A) Graph showing the weight change in *Control*$^{ds\text{-}DTR}$ (*Prox2*^{FlpO};*Tau*$^{ds\text{-}DTR}$, **top)** and *Prox2/Runx3*$^{ds\text{-}DTR}$ (*Prox2*^{FlpO};*Phox2b*^{Cre};*Tau*$^{ds\text{-}DTR}$ animals, **bottom)** mice for 14 days following DT administration. **(B)** Outline of the experimental timeline.

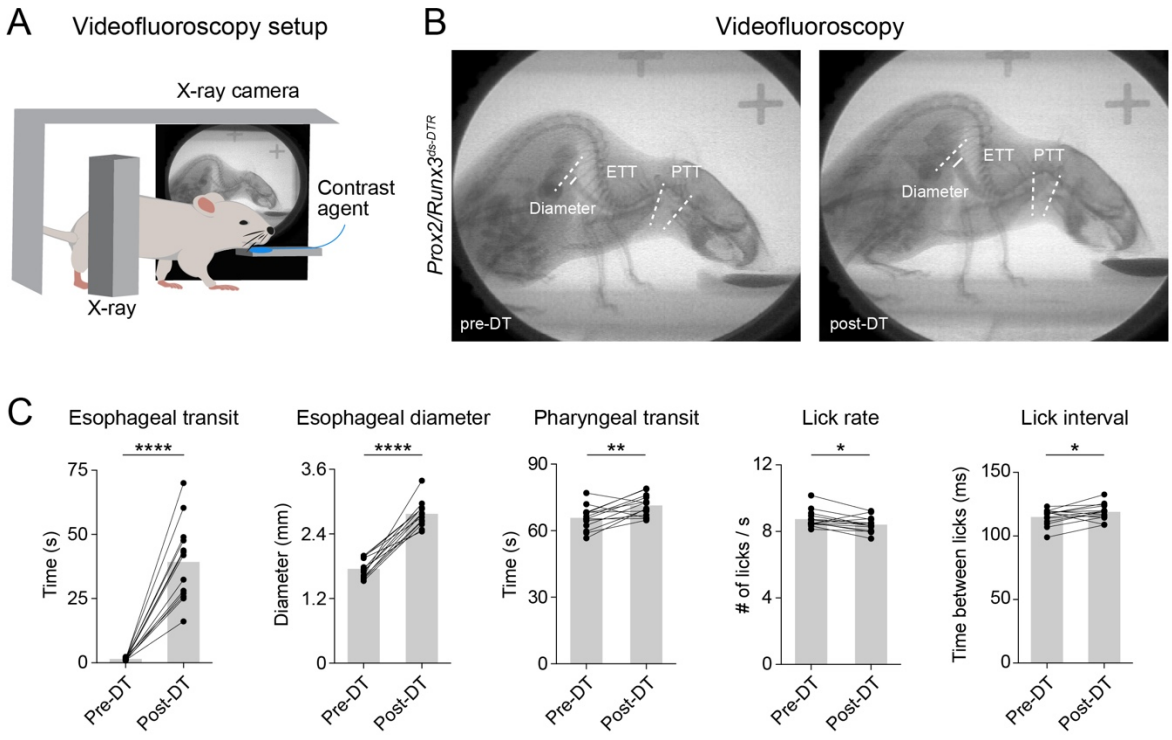

Figure 37. Ablation of Prox2/Runx3 neurons impairs esophageal motility in freely behaving animals. (A) Schema of the videofluoroscopy setup. **(B)** Single frame X-ray images from videofluoroscopy videos taken from one *Prox2/Runx3*$^{ds\text{-}DTR}$ mouse before (*Prox2*^{FlpO}*;Phox2b*^{Cre}*;Tau*$^{ds\text{-}DTR}$, pre-DT, **left**) and after (post-DT, **right**) DT administration. Dotted white lines show the bolus traveling distance used to determine pharyngeal transit time (PTT) and esophageal transit time (ETT). Solid white line shows the site used to measure the esophageal diameter. **(C)** Esophageal transit time increased from an average of 1.5±0.5s to 39.3±15.4s after ablation, p<0.0001. Esophageal diameter increased from an average of 1.7±0.2mm to 2.8±0.2mm after ablation, p<0.0001. Pharyngeal transit time increased from an average of 65.8±5.3ms to 71.3±4.8ms after ablation, p=0.0051. Lick rate decreased from an average of 8.7±0.5licks/s to 8.4±0.5licks/s after ablation, p=0.0176. Lick interval increased from an average of 114.9±6.3ms to 118.9±6.4ms after ablation, p=0.0335, n=13-14. Data are represented as mean ± SD, *p<0.05, **p<0.01, ***p<0.001, ****p<0.0001, paired two-tailed t-test. VFSS experiments were performed in the Lever laboratory at the University of Missouri School of Medicine together with Dr. Teresa Lever and Kate Osman.

VFSS involves placing awake, freely behaving mice in a small chamber where they have access to liquid contrast agent. The contrast agent is placed in front of a miniaturized, low-energy fluoroscope that records x-ray movies of the drinking bouts (Figure 37A). VFSS allows for the recording and subsequent analysis of many swallowing parameters and related orofacial parameters (Figure 37B). The esophageal transit time of a liquid bolus increased from an average of 1.5±0.4 seconds to 39.3±15.4 seconds after ablation (Figure 37C). Additionally, the liquid bolus was frequently retained in the esophagus, flowed in an orad direction to re-enter the pharynx, and in some cases resulted in projectile regurgitation from the mouth (Video 3). These aberrant esophageal bolus flow behaviors were never observed before ablation. This was accompanied by megaesophagus, with the average diameter of their abdominal esophagus increasing from an average of 1.7±0.2 mm before ablation to 2.8±0.2 mm after ablation (Figure 37C). Moreover, numerous examples of aerophagia were observed after ablation (Video 4). In addition, pharyngeal transit time was increased, whereas lick rate and lick interval were slightly decreased and increased, respectively (Figure 37C).

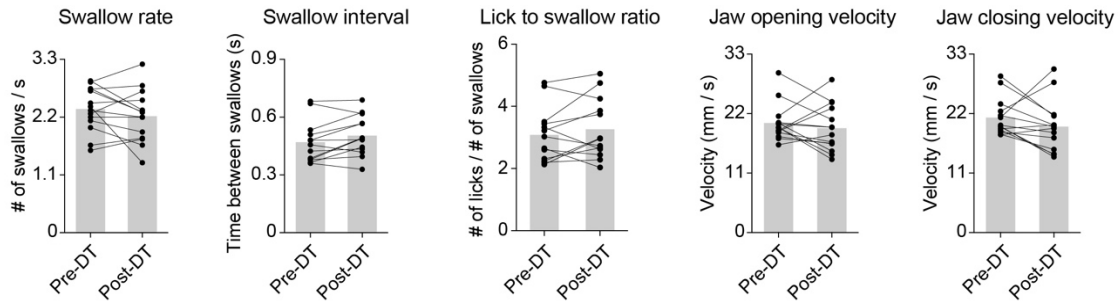

Figure 38. Oropharyngeal swallow-related behaviors were unaffected after Prox2/Runx3 vagal neuron ablation. Many oropharyngeal swallow-related behaviors were unaffected after Prox2/Runx3 ablation. Swallow rate (2.4±0.4swallows/s to 2.2±0.5swallows/s), swallow interval (0.5±0.1s to 0.5±0.1s), lick to swallow ratio (3.1±0.9 # of licks / # of swallows to 3.3±1.0 # of licks / # of swallows), jaw opening velocity (20.3±3.4mm/s to 19.3±4.3mm/s) and jaw closing velocity (21.3±3.4mm/s to 19.6±4.8mm/s) were all unaffected, n =13-14. Data are represented as mean ± SD, paired two-tailed t-test. One animal (#5697) was removed as an outlier from the Swallow interval and Lick to swallow ratio plots, as it failed the Grubbs' test with alpha=0.01. VFSS experiments were performed in the Lever laboratory at the University of Missouri School of Medicine together with Dr. Teresa Lever and Kate Osman.

All other parameters related to the biomechanics of swallowing (swallow rate, swallow interval, lick to swallow ratio, jaw opening/closing velocity) were unaffected (Figure 38). In summary, we observed severe deficits in ingestion after the ablation of Prox2/Runx3 neurons that were assigned to esophageal dysmotility. I performed all of the VFSS experiments together with Kate Osman and Dr. Teresa Lever in the Lever laboratory at the University of Missouri School of Medicine.

In summary, we used genetically guided anatomical tracing and optogenetic tools to show that three vagal sensory neuronal subtypes that express *Prox2* and *Runx3* innervate the esophagus and stomach with regionalized specificity.

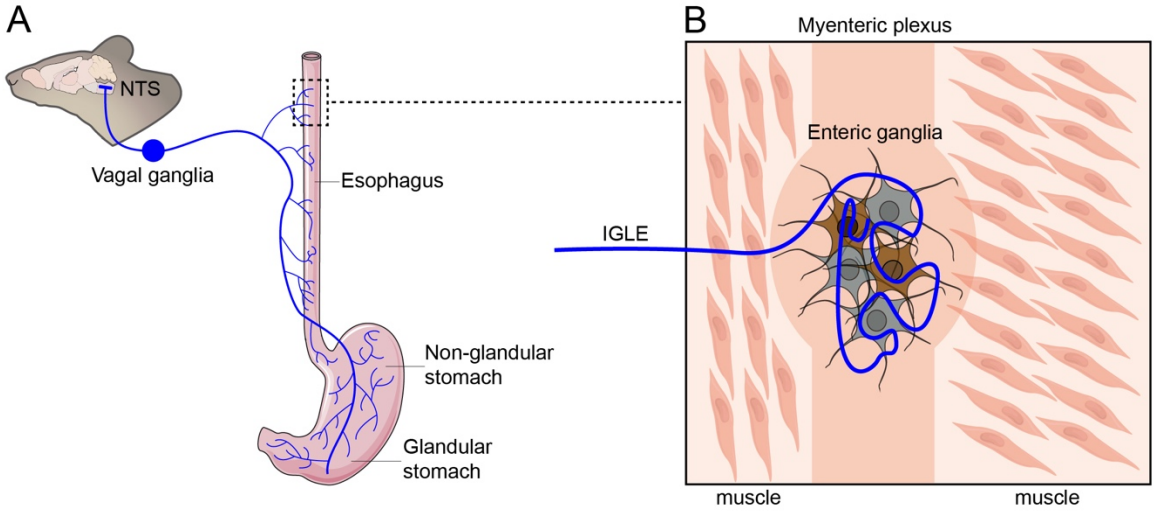

C

Supercluster	Subtype	Mouse lines	Marker genes	Preferred organ	Ending	Properties	Function
Prox2	MM1	*Prox2/Runx3^{Tom}*	*Prox2+, Piezo2+, Rbp4+, Glp1r+, Gata3-*	Non-glandular stomach	IGLE	Low-threshold, slowly adaptating	Stomach accomodation?
Prox2	MM2	*Prox2/Runx3^{Tom}*	*Prox2+, Piezo2+, Grm5+, Glp1r-*	Esophagus	IGLE	Low-threshold, slowly adapting	Esophageal peristalsis
Runx3	MM8	*Prox2/Runx3^{Tom} Runx3^{Tom}*	*Runx3+, Prox2^{low}, Piezo2+, Adra2a+, Glp1r+*	Glandular stomach	IGLE	Low-threshold, quickly adapting	Stomach emptying?

Figure 39. Summary. (A) Scheme of MM1, MM2 and MM8 vagal neurons and their targets in the upper gastrointestinal tract. Illustrations were adapted from bioicons.com (digestive-system-exploded, Servier; smooth-muscle-fiber, Servier; neuron, DBCLS) and scidraw.io (Mouse Brain Silhouette, Ann Kennedy) and licensed under CC-BY 3.0 and CC-BY 4.0. **(B)** Scheme of an MM2 IGLE contacting an esophageal enteric ganglion. Note that both excitatory (gray) and inhibitory (brown) esophageal motor neurons are contacted by the IGLE. **(C)** Table summarizing the characteristics of MM1, MM2 and MM8 vagal neurons. Indicated are the mouse lines used to label the neuronal subtypes, marker genes used to identify them, the preferred organ innervated by the neuronal subtypes, their mechanosensitive properties, and their putative functions in digestive physiology.

All three subtypes form IGLEs on enteric ganglia and function as low threshold mechanoreceptors, but display different adaptation properties (See Figure 39 for a summary). We refer to these subtypes as MM1, MM2 and MM3 and define their molecular characteristics. Moreover, we genetically ablated Prox2/Runx3 neurons, and demonstrate that this resulted in dysphagia due to severe esophageal dysmotility in freely behaving animals. Our results reveal the importance of vagal sensory feedback provided by Prox2/Runx3 neurons in swallowing and esophageal motility.

5. Discussion

Sensory neurons of the vagus nerve survey the mechanical state of the gastrointestinal tract and monitor esophageal and gastric distension. Previous work identified the vagal subtypes that monitor stomach and intestinal stretch (Bai *et al.*, 2019; Williams *et al.*, 2016), and this project set out to study the vagal subtype(s) that monitor esophageal stretch. In order to obtain insight into vagal neuron heterogeneity we first performed scRNA-seq of vagal neurons at P4 and merged our data with two other studies (Bai *et al.*, 2019; Kupari *et al.*, 2019). Our meta-analysis based on these datasets identified 27 transcriptomically unique subtypes of vagal neurons. We leveraged this transcriptomic information to generate a novel mouse strain that allowed us to perform a genetically guided characterization of a large set of putative vagal mechanoreceptors. We used genetic tools for anatomical tracing to show that three vagal sensory neuronal subtypes that express *Prox2* and *Runx3* innervate the esophagus and stomach with regionalized specificity; furthermore, all three subtypes formed IGLEs on enteric ganglia. Additionally, we used a genetic approach to optogenetically target Prox2/Runx3 neurons. This demonstrated that although the three Prox2 and Runx3 subtypes all function as low threshold mechanoreceptors, they displayed unique adaptation properties (See Figure 39 for a summary). Lastly, we genetically ablated Prox2/Runx3 neurons:

this resulted in dysphagia due to severe esophageal dysmotility in freely moving animals. Our results reveal the importance of vagal sensory feedback provided by Prox2/Runx3 neurons in swallowing and food intake.

5.1. Vagal neuron heterogeneity

scRNA-seq has revolutionized neuroscience by shining a light on the extraordinary molecular heterogeneity of neuronal subtypes in the nervous system (Zeisel et al., 2018). Most work using scRNA-seq approaches has been applied to the central nervous system, and when I began my PhD the only peripheral ganglia that had been sequenced were the somatosensory dorsal root ganglia (Li et al., 2016; Usoskin et al., 2015). Thus, the first major undertaking of my PhD project was to perform scRNA-seq on the vagal ganglia in order to uncover the transcriptomic heterogeneity of viscerosensory neurons. In order to isolate vagal cells and to enrich for neurons, we used *VGlut2^{Cre};R26^{nGFP}* mice at postnatal day (P) 4. In such animals >99% of all vagal neurons are labeled by GFP, which had been previously shown by others (Chang et al., 2015; Williams *et al.*, 2016). I performed flow cytometry to sort and isolate GFP+ vagal neurons for sequencing. We sequenced 1536 neurons, of which 1392 neurons passed quality control and were included in the downstream analyses. We used this same mouse strain to count the total number of vagal neurons using lightsheet microscopy and found that each vagal ganglion contains a total of ~5,000 neurons, i.e. a total of ~10,000 vagal neurons per mouse. Thus our sequencing run contained roughly ~15% of the total number of vagal neurons from one mouse, which is an high sampling rate for an scRNA-seq experiment (Anderson and Larson, 2020; Dvoryanchikov et al., 2017; Haque et al., 2017). Thus, we had a ~16% chance of detecting a rare neuronal subtype comprising only 1% of all vagal neurons if the left and right ganglia contained different neurons, and a ~32% chance of detecting the same rare population if the left and right vagal ganglia contained similar neurons. This gave us confidence that our sequencing run would contain all vagal neuron subtypes.

Our initial bioinformatics analysis revealed 22 subtypes of vagal neurons at P4, including 4 subtypes of jugular neurons, 9 subtypes of mechanosensory-like nodose neurons, and 9 subtypes of chemosensory-like nodose neurons. Shortly after we concluded our bioinformatics analysis in 2019, two papers were published that included scRNA-seq data from adult vagal neurons (Bai *et al.*, 2019; Kupari *et al.*, 2019). We applied a novel integration method and combined our data sets with the published ones, to perform a meta-analysis of vagal neurons (Stuart *et al.*, 2019). In

particular, the integration of multiple single cell data sets allows for the discovery of rare subtypes, and increases the robustness of subtype annotation. After integration, the meta-analysis included 4,442 vagal neurons that were organized into 27 subtypes, including 6 subtypes of jugular neurons, 10 subtypes of mechanosensory-like nodose neurons, and 11 subtypes of chemosensory-like nodose neurons. Thus, the meta-analysis allowed us to better resolve vagal neuron heterogeneity and uncovered 5 additional subtypes.

This year, numerous laboratories collaborated to generate a reference atlas of transcriptomic subtypes in the hypothalamus (Steuernagel et al., 2022). Steuernagel and colleagues integrated scRNA-seq data from 18 independent studies of hypothalamic diversity, and after quality control analyzed transcriptomic profiles from 384,925 cells that they organized into 185 subtypes. This meta-analysis identified previously unknown hypothalamic subtypes, harmonized subtype annotation between data-sets to allow for easy and more efficient interpretation, and created a framework that new sequencing data can be added to. Since our analysis other groups have generated scRNA-seq data sets of vagal neurons (Buchanan *et al.*, 2022; Liu *et al.*, 2021; Prescott *et al.*, 2020; Zhao *et al.*, 2022), and it would benefit the field to emulate the work of those studying the hypothalamus and generate a reference atlas for vagal neurons.

In our meta-analysis, neurons from each data set contributed to each subtype. This suggests that all vagal neuron subtypes are already present by early postnatal life. However, a recent preprint compared bulk RNA-seq data from the nodose ganglion at P7 and adults (12 weeks old) and found that roughly 20% of all genes were differentially expressed (McCoy and Kamitakahara, 2022). Pathway analysis revealed that axon guidance signaling and synaptic long-term potentiation were more enriched in the adult, suggesting that after P7 nodose neurons undergo further maturation. Taking this new study into account, it seems that although all transcriptomic subtypes of nodose neurons are present shortly after birth, they continue to mature after the first week of postnatal life.

5.2. Prox2/Runx3 neurons that innervate the esophagus and stomach

Prox2/Runx3 neurons represent the majority (~85%) of all *Piezo2*+ neurons in the nodose ganglion and encompass eight neuronal subtypes. We show here that three of these, the MM1, MM2 and MM8 subtypes, form IGLEs that innervate enteric ganglia in the esophagus and stomach. Comparison of our molecular data with previously published analyses indicate that among vagal Prox2/Runx3 neurons, the MM9 and MM10 subtypes might correspond to neurons

innervating the lung, and MM5 to neurons innervating the larynx (Liu *et al.*, 2021; Prescott *et al.*, 2020) (summarized in Table 2). The assignment of the Prox2/Runx3 neuronal subtypes innervating the heart needs further investigation (Min *et al.*, 2019). We found additional ganglia containing Prox2/Runx3 neurons that were also recombined by our intersectional genetic approach, namely the geniculate and celiac ganglia. Prox2/Runx3 neurons of geniculate ganglia likely innervate taste buds in the tongue (Zaidi and Whitehead, 2006), while Prox2/Runx3 neurons of the celiac ganglia likely innervate blood vessels and/or enteric neurons in the intestine (Miolan and Niel, 1996). Further work is needed to definitively determine the target that these neurons innervate their physiological functions.

Together, the MM2 and MM8 subtypes of Prox2/Runx3 neurons innervate almost all (>95%) esophageal enteric ganglia, with MM2 being by far the more abundant subtype. Despite the morphological similarity of the nerve endings, we were able to distinguish between MM2 and MM8 neurons in our genetically guided neuroanatomical tracing experiments. While both MM2 and MM8 subtypes were labeled in *Prox2/Runx3*^{Tom} animals, only the MM8 subtype was labeled in *Runx3*^{Tom} animals. Thus, by comparing the pattern of tdTomato expression in the esophagus from these two strains, we could identify the projection patterns of the MM2 and MM8 subtypes.

The ablation of the Prox2/Runx3 neurons demonstrated the importance of these neurons in the esophageal phase of swallowing. Specifically, their ablation resulted in a dramatic increase in the transit time of a bolus through the esophagus that was accompanied by megaesophagus. Esophageal peristalsis is part of a complex motor sequence involving the consecutive and stereotypic contractions of pharyngeal and esophageal muscle groups (Kim *et al.*, 2022; Prescott and Liberles, 2022). This intricate sequence of events is controlled by a central pattern generator in the brainstem (Jean, 2001). Deafferentation of the thoracic esophagus in sheep provided early evidence of the importance of vagal sensory feedback in esophageal peristalsis, but the molecular nature of the vagal sensory neurons mediating the essential signals was unknown (Falempin *et al.*, 1986). Our results show that the MM2 and MM8 subtypes of Prox2/Runx3 neurons provide the necessary peripheral feedback for esophageal peristalsis.

Previous work showed that *Glp1r* is specifically expressed in the vagal neurons that form gastric IGLEs (Williams *et al.*, 2016). Here, we identify three neuronal subtypes that innervate the stomach with regional preferences, of which only two (MM1 and MM8) express *Glp1r*. Previous work on Glp1r+ stomach IGLEs revealed that they do not respond uniformly in response to stretch

(Williams *et al.*, 2016). Here, I provide new data showing that Glp1r+ stomach afferents are actually comprised of two transcriptomically unique subtypes that project to distinct areas of the stomach and display different electrophysiological responses to stomach stretch. Thus, gastric IGLEs are more heterogenous than previously recognized. Others described an Oxtr+ subtype of vagal sensory neurons that forms IGLEs on intestinal ganglia (Bai *et al.*, 2019), but intestinal IGLEs are not formed by vagal Prox2/Runx3 neurons, although the MM2 subtype that projects to the esophagus also expresses *Oxtr*. More work is needed to unambiguously define the molecular characteristics of the Oxtr+ vagal subtype that forms intestinal IGLEs. Thus, despite their apparent morphological uniformity, IGLEs in the upper esophagus, stomach and intestine originate from molecularly distinct vagal neuron subtypes.

Although vagal viscerosensory neurons are classically thought of as purely afferent in nature, sensing in the periphery and projecting centrally, there is a growing body of evidence that they might also be efferent (Raab and Neuhuber, 2007). In 1987 Neuhuber performed an electron microscopy analysis of the rat esophagus, and discovered small clear vesicles within the IGLE directly across from enteric neurons. Follow up studies found the presynaptic protein Synaptophysin and VGlut2 within esophageal IGLEs (Neuhuber et al., 2006; Raab and Neuhuber, 2003). Here, I show that Prox2/Runx3 esophageal IGLEs contain elements of the presynaptic machinery using an intersectional genetic approach to drive expression of Synaptophysin-GFP combined with immunofluorescence against Synapsin1 and VGlut2. The co-localization of GFP with Synapsin1 and VGlut2 in the esophagus suggests that Prox2/Runx3 neurons may be efferently connected to cells in the periphery. However, it must be mentioned that a study using antidromic stimulation of vagal afferents did not find a significant increase in c-Fos expression in enteric neurons (Zheng *et al.*, 1997). Thus, the significance of presynaptic machinery in the IGLE is still unknown. It is intriguing that esophageal IGLEs are labeled by their expression of *Grm5*, a metabotropic glutamate receptor (Slattery et al., 2006; Young et al., 2007). Perhaps the IGLE releases glutamate to regulate its own firing in response to certain mechanical stimuli? Enteric ganglia contain more cell types than enteric neurons as they are also populated by glial, immune and endothelial cells (Spencer and Hu, 2020). It may be that IGLEs release glutamate to modulate any of these cell types (Raab and Neuhuber, 2007). As our work shows that IGLEs are intrinsically mechanosensitive, it remains unclear why they innervate enteric neurons rather than mechanically active cells like smooth muscle. They might perhaps exert an efferent effect by releasing glutamate

locally. Hopefully future studies will expand our knowledge of the relationship between IGLEs and their local environment in the digestive tract, solving the mystery of why IGLEs innervate enteric ganglia.

5.3. Electrophysiological properties of Prox2/Runx3 neurons innervating the upper gastrointestinal tract

The electrophysiological studies described in this thesis were performed by a postdoctoral fellow in the laboratory, Dr. Pierre-Louis Ruffault, who recorded vagal fibers isolated from *Prox2/Runx3*^{ChR} mice that were generated by Elijah Lowenstein. Dr. Ruffault used *ex vivo* vagus nerve-stomach and vagus nerve-esophagus preparations to record from vagal fibers that respond to light and mechanical stimuli, i.e. mechanical probing of the esophagus or stomach inflation. Previous analyses of gastrointestinal mechanoreceptors distinguished electrophysiological responses to stretch, tension and mechanical probing, uncovering both muscular and mucosal mechanoreceptors in various species (Kim *et al.*, 2022; Page and Blackshaw, 1998; Page *et al.*, 2002; Zagorodnyuk and Brookes, 2000; Zagorodnyuk *et al.*, 2003). The use of specific optogenetic tools allowed us to analyze a small subset of morphologically and molecularly defined neurons and to determine their electrophysiological properties. Prox2/Runx3 neurons represent all vagal *Piezo2*+ neurons innervating the stomach. Nevertheless, only about half of all mechanoreceptors that respond to stomach distention correspond to Prox2/Runx3 neurons, demonstrating that Piezo2-negative gastric mechanoreceptors exist. In the somatosensory system, genetic ablation of *Piezo2* leads to the loss or reduced mechanosensitivity of both rapidly and slowly adapting low threshold mechanoreceptors (Murthy et al., 2018; Ranade et al., 2014; Woo et al., 2014). Work involving the genetic deletion of Piezos in vagal sensory neurons revealed their function in the control of breathing and blood pressure (Nonomura et al., 2017; Zeng et al., 2018). Further studies are required to address the precise role of *Piezo2* in the Prox2/Runx3 neurons innervating the gastrointestinal tract, and to uncover the identity of the Prox2/Runx3-negative vagal gastric mechanoreceptors. Prox2/Runx3 neurons also express many other genes that have been shown to be involved in mechanosensation. For example, Prox2/Runx3 neurons express ASIC1, ablation of which has been shown to increase gastric emptying (Page et al., 2004; Page et al., 2005). Thus, the exact mechanosensory channel(s) used by Prox2/Runx3 and other neuronal types to detect stomach stretch is open.

In accordance with the molecular and anatomical data, our electrophysiological experiments distinguished various Prox2/Runx3 mechanoreceptive subtypes. The esophageal type I and type II low threshold mechanoreceptors possess distinct adaptation properties, with type I receptors adapting more slowly than type II receptors. Type I outnumbered type II mechanoreceptors four to one. MM2 are the most abundant Prox2/Runx3 neuronal subtype innervating the esophagus. We therefore propose that MM2 neurons correspond to esophageal type I mechanoreceptors, and MM8 to type II receptors. It is possible that the signals detected by the MM2 and MM8 neurons encode distinct aspects of esophageal distension. Esophageal distension mediates reflexes that result in contraction of the upper esophageal sphincter, and these differentially respond to slow and fast esophageal distention (Lang, 2009; Lang et al., 2001). Here, we analyzed the consequences of simultaneously ablating MM2 and MM8 subtypes, but it would be interesting to dissect the relative contributions of the two different subtypes to esophageal reflexes in future studies.

Prox2/Runx3 mechanoreceptors in the stomach also differed in their adaptation properties. Both, gastric and esophageal type I receptors displayed similar properties and were slowly adapting. We propose that the gastric type I receptors correspond to MM1, whereas we assign the esophageal type I receptor to the transcriptionally related MM2 subtype. Further, esophageal and gastric type II receptors display similar adaption properties, and our data suggests that these correspond to the MM8 subtype. This is also supported by a recent study that recorded calcium activity in vagal neurons during stomach/esophagus distension and found that a group of neurons called Group C display a slowly adapting response. Group C neurons contain *Piezo2+Glp1r+Rbp4+* and *Piezo2+Grm5+Slit2+* subtypes that appear to correspond to the Prox2+ MM1 and MM2 subtypes, the proposed type I mechanoreceptors that we describe here (Zhao *et al.*, 2022).

The slowly adapting MM1 and faster adapting MM8 gastric IGLE subtypes are regionally specialized, preferentially innervating the non-glandular and glandular stomach, respectively. These portions of the stomach have different functional roles during digestion (Janssen *et al.*, 2011). During feeding, the ingested material collects in the non-glandular stomach that acts as a food reservoir and slowly expands in a process known as gastric accommodation. Fast peristaltic contractions then mechanically break down the ingested material in the glandular stomach (Janssen *et al.*, 2011). Based on their regional specificity and functional responses, we hypothesize that the

slowly adapting MM1 type I mechanoreceptors specialize to detect the volume changes that occur in the non-glandular stomach during gastric accommodation, while the fast adapting MM8 type II mechanoreceptors detect phasic stretch that accompanies peristaltic contractions in the glandular stomach. The genetic ablation strategy used here affected all three neuronal subtypes (MM1, MM2 and MM8) that end as IGLEs in the esophagus and stomach. Our videofluoroscopy data show boli entering and leaving the stomach, as well stomach contractions, after the ablation of Prox2/Runx3 neurons. However, the experimental setup lacked sufficient resolution for accurate quantification of gastric contractions and emptying. The current gold standard for diagnosing gastric paresis in patients is gastric emptying scintigraphy (Grover et al., 2019; Hasler, 2011; Ora et al., 2019). It may be possible to use this method in the future to study gastric motility after ablation of Prox2/Runx3 neurons in our ablation mouse model (Bennink et al., 2003).

5.4. Neuronal control of esophageal motility

Abnormal esophageal motility is present in a heterogeneous class of disorders of frequently unknown etiology (Kahrilas et al., 2015). Hereditary, autoimmune, and infectious factors, as well as nervous system degeneration are all suggested to cause or contribute to this pathology (Boeckxstaens et al., 2014). In humans, VFSS are used to diagnose and monitor swallowing dysfunction (Martin-Harris and Jones, 2008). Recent efforts have adapted VFSS for use in rodents (Lever *et al.*, 2015; Mueller *et al.*, 2022; Welby *et al.*, 2020). Here, we used VFSS to analyze mice in which we eliminated Prox2/Runx3 neurons, the ablation of which revealed marked esophageal dysmotility. Our histological and retrograde tracing studies assign the regulation of esophageal motility to the Prox2/Runx3 neuronal subtypes MM2 and MM8 that form IGLEs along the entire rostro-caudal axis of the esophagus. Further, the meta-analysis reported here provides detailed information on genes expressed in these neuronal subtypes, and can be mined for the identification of potential drug targets. This might be useful to specifically modulate the vagal sensory neurons that control esophageal peristalsis with the goal to ameliorate motility disorders.

In addition to the vagal sensory arm that provides feedback needed for esophageal peristalsis, the sensorimotor circuit controlling esophageal motility includes the hindbrain central pattern generator in the nucleus of the solitary tract (NTS), as well as visceromotor effector neurons located in hindbrain motor nuclei, in particular the nucleus ambiguus (Coverdell et al., 2022; Goyal and Chaudhury, 2008; Jean, 2001; Kim *et al.*, 2022; Spencer and Hu, 2020). Our intersectional

genetic approach relying on *Prox2^{FlpO};Phox2b^{Cre}* specifically affects the sensory arm, but not the NTS or hindbrain motor nuclei (see Figures 16, 35).

Prox2/Runx3 vagal neurons also innervate the larynx and might thus participate in the pharyngeal phase of swallowing. Further, Prox2/Runx3 geniculate neurons innervate the tongue and their ablation might affect lick rate. The ablation of Prox2/Runx3 neurons had extremely pronounced effects on the esophageal phase of swallowing (~2500% increase in transit time), compared to the comparatively mild effects on the pharyngeal phase (~8% increase in transit time) and lick rates (~4% decrease), whereas swallow rate and swallow interval were unchanged. Whether the mild changes in the pharyngeal transit time and lick rate are directly caused by the loss of Prox2/Runx3 neurons innervating the larynx or tongue, or indirectly by esophageal immobility remains to be determined.

The Prox2/Runx3 vagal sensory neurons that we characterized project to several defined neuronal types in the NTS, and form synaptic boutons on Pou3f1+ neurons in the central nucleus of the NTS. Further analyses are needed to unambiguously show that Pou3f1+ neurons are direct synaptic targets of Prox2/Runx3 vagal sensory neurons. Esophageal afferents are known to project to neurons of previously uncharacterized identity in the central NTS, which in turn project to esophageal motor neurons in the nucleus ambiguus (Altschuler et al., 1989). We suggest that the Pou3f1+ neurons in the central NTS are well positioned to play a key role in esophageal function.

6. Relevance and outlook

All scientific undertakings open up as many questions as they answer, and this thesis is no different. My work uncovered the molecular identity of two subtypes of Prox2/Runx3 vagal neurons that project to the esophagus. Although both subtypes end as IGLEs and are low-threshold mechanoreceptors, they differ in their electrophysiological characteristics and projection patterns, i.e. the two subtypes preferentially innervate particular areas of the esophagus. The simultaneous ablation of both subtypes caused marked esophageal dysmotility and megaesophagus, highlighting their crucial roles in esophageal peristalsis. But the individual role of each subtype remains to be elucidated. Beyond their broad innervation preferences along the rostro-caudal axis of the esophagus, do they interact with different cell types in the enteric ganglia? Do they detect different types of mechanical forces in the esophageal wall? The generation of new Cre-lines (e.g. *Grm5^{Cre}* or *Adra2a^{Cre}*) in combination with the newly generated *Prox2^{FlpO}* line described here would give

specific genetic access to label, activate and ablate MM2 or MM8, respectively, and open the door to dissecting out the individual roles of these esophageal mechanoreceptors.

Another major unanswered question is what is the transcriptomic identity and physiological role of IMAs? While both intersectional genetic strategies used in this work labeled rare IMAs in the stomach, IMAs around the lower esophageal and pyloric sphincters were only labeled in *Prox2^{FlpO};Phox2b^{Cre};Ai65* animals. Although we tried to perform retrograde labeling from the lower esophageal sphincter to label IMAs, due to technical limitations we were unable to limit the injection to the sphincter, and in every case the tracer spread to the neighboring stomach. Based on our histological analyses it seems as though there are at least two distinct transcriptomic types of IMAs in the upper gastrointestinal tract, Prox2+ or Runx3+ stomach IMAs and Prox2+ lower esophageal sphincter IMAs. Hopefully future research will pick up this problem and shine a light on the identity and function of this enigmatic vagal neuron type.

Vagal mechanoreceptors play key roles in maintaining bodily homeostasis, from baroreceptors that detect blood pressure, to neurons that detect lung or stomach stretch (Prescott and Liberles, 2022; Umans and Liberles, 2018). The first key advance of this doctoral thesis is the unambiguous demonstration that the neuronal circuit controlling esophageal motility absolutely depends on feedback from vagal sensory neurons. Previous experiments that suggested this were based on rather unspecific methods, i.e. blunt dissection of the vagus nerve or nodose ganglia and swallowing analysis under anesthesia (Falempin *et al.*, 1986). Vagus nerve transection also interferes with the function of the motor arm of the reflex circuit, and anesthesia affects esophageal peristalsis, thus complicating the interpretation of the results. The second key finding is that I was able to pinpoint the molecular identity of the responsible vagal sensory neurons. I show that the Prox2/Runx3 vagal mechanoreceptor subtypes MM2 and MM8 detect esophageal mechanical stimuli and are required for esophageal motility. This work adds to the growing body of literature of vagal mechanoreceptors that detect stretch in the gastrointestinal system, in particular Glp1r+ and Oxtr+ afferents that detect stomach and intestinal stretch, respectively (Bai *et al.*, 2019; Williams *et al.*, 2016). Each of these neuronal subtypes expresses distinct receptors, many of which can be manipulated by pharmacology. Future researchers can explore the molecular data on the identity of vagal neurons that sense stretch to uncover potential avenues for the stimulation or inhibition of peristalsis and for the treatment of gastrointestinal disorders.

7. References

Abe, T., Kiyonari, H., Shioi, G., Inoue, K., Nakao, K., Aizawa, S., and Fujimori, T. (2011). Establishment of conditional reporter mouse lines at ROSA26 locus for live cell imaging. Genesis *49*, 579-590. 10.1002/dvg.20753.

Altschuler, S.M., Bao, X.M., Bieger, D., Hopkins, D.A., and Miselis, R.R. (1989). Viscerotopic representation of the upper alimentary tract in the rat: sensory ganglia and nuclei of the solitary and spinal trigeminal tracts. J Comp Neurol *283*, 248-268. 10.1002/cne.902830207.

Anderson, C.B., and Larson, E.D. (2020). Single Cell Transcriptional Profiling of Phox2b-Expressing Geniculate Ganglion Neurons. bioRxiv, 812578. 10.1101/812578.

Aslam, M., and Vaezi, M.F. (2013). Dysphagia in the elderly. Gastroenterol Hepatol (N Y) *9*, 784-795.

Ayer-Le Lievre, C.S., and Le Douarin, N.M. (1982). The early development of cranial sensory ganglia and the potentialities of their component cells studied in quail-chick chimeras. Dev Biol *94*, 291-310. 10.1016/0012-1606(82)90349-9.

Aziz, Q., Fass, R., Gyawali, C.P., Miwa, H., Pandolfino, J.E., and Zerbib, F. (2016). Functional Esophageal Disorders. Gastroenterology. 10.1053/j.gastro.2016.02.012.

Baetge, G., and Gershon, M.D. (1989). Transient catecholaminergic (TC) cells in the vagus nerves and bowel of fetal mice: relationship to the development of enteric neurons. Dev Biol *132*, 189-211. 10.1016/0012-1606(89)90217-0.

Bai, L., Mesgarzadeh, S., Ramesh, K.S., Huey, E.L., Liu, Y., Gray, L.A., Aitken, T.J., Chen, Y., Beutler, L.R., Ahn, J.S., et al. (2019). Genetic Identification of Vagal Sensory Neurons That Control Feeding. Cell *179*, 1129-1143 e1123. 10.1016/j.cell.2019.10.031.

Bear, M.F., Connors, B.W., and Paradiso, M.A. (2015). Neuroscience: Exploring the Brain, 4 Edition (Jones and Bartlett Pub. Inc.).

Begbie, J., Ballivet, M., and Graham, A. (2002). Early steps in the production of sensory neurons by the neurogenic placodes. Mol Cell Neurosci *21*, 502-511. 10.1006/mcne.2002.1197.

Bennink, R.J., De Jonge, W.J., Symonds, E.L., van den Wijngaard, R.M., Spijkerboer, A.L., Benninga, M.A., and Boeckxstaens, G.E. (2003). Validation of gastric-emptying scintigraphy of solids and liquids in mice using dedicated animal pinhole scintigraphy. J Nucl Med *44*, 1099-1104.

Bentivoglio, M., Kuypers, H.G., Catsman-Berrevoets, C.E., Loewe, H., and Dann, O. (1980). Two new fluorescent retrograde neuronal tracers which are transported over long distances. Neurosci Lett *18*, 25-30. 10.1016/0304-3940(80)90208-6.

Berthoud, H.R., Blackshaw, L.A., Brookes, S.J., and Grundy, D. (2004). Neuroanatomy of extrinsic afferents supplying the gastrointestinal tract. Neurogastroenterol Motil *16 Suppl 1*, 28-33. 10.1111/j.1743-3150.2004.00471.x.

Berthoud, H.R., Kressel, M., Raybould, H.E., and Neuhuber, W.L. (1995). Vagal sensors in the rat duodenal mucosa: distribution and structure as revealed by in vivo DiI-tracing. Anat Embryol (Berl) *191*, 203-212. 10.1007/BF00187819.

Berthoud, H.R., and Patterson, L.M. (1996). Anatomical relationship between vagal afferent fibers and CCK-immunoreactive entero-endocrine cells in the rat small intestinal mucosa. Acta Anat (Basel) *156*, 123-131. 10.1159/000147837.

Berthoud, H.R., and Powley, T.L. (1992). Vagal afferent innervation of the rat fundic stomach: morphological characterization of the gastric tension receptor. J Comp Neurol *319*, 261-276. 10.1002/cne.903190206.

Boeckxstaens, G.E., Zaninotto, G., and Richter, J.E. (2014). Achalasia. Lancet *383*, 83-93. 10.1016/S0140-6736(13)60651-0.

Britsch, S., Goerich, D.E., Riethmacher, D., Peirano, R.I., Rossner, M., Nave, K.A., Birchmeier, C., and Wegner, M. (2001). The transcription factor Sox10 is a key regulator of peripheral glial development. Genes Dev *15*, 66-78. 10.1101/gad.186601.

Britz, O., Zhang, J., Grossmann, K.S., Dyck, J., Kim, J.C., Dymecki, S., Gosgnach, S., and Goulding, M. (2015). A genetically defined asymmetry underlies the inhibitory control of flexor-extensor locomotor movements. Elife *4*. 10.7554/eLife.04718.

Bronner-Fraser, M. (2002). Molecular analysis of neural crest formation. J Physiol Paris *96*, 3-8. 10.1016/s0928-4257(01)00074-2.

Brookes, S.J., Spencer, N.J., Costa, M., and Zagorodnyuk, V.P. (2013). Extrinsic primary afferent signalling in the gut. Nat Rev Gastroenterol Hepatol *10*, 286-296. 10.1038/nrgastro.2013.29.

Browning, K.N., and Travagli, R.A. (2014). Central nervous system control of gastrointestinal motility and secretion and modulation of gastrointestinal functions. Compr Physiol *4*, 1339-1368. 10.1002/cphy.c130055.

Buchanan, K.L., Rupprecht, L.E., Kaelberer, M.M., Sahasrabudhe, A., Klein, M.E., Villalobos, J.A., Liu, W.W., Yang, A., Gelman, J., Park, S., et al. (2022). The preference for sugar over sweetener depends on a gut sensor cell. Nat Neurosci *25*, 191-200. 10.1038/s41593-021-00982-7.

Castelucci, P., Robbins, H.L., and Furness, J.B. (2003). P2X(2) purine receptor immunoreactivity of intraganglionic laminar endings in the mouse gastrointestinal tract. Cell Tissue Res *312*, 167-174. 10.1007/s00441-003-0715-3.

Caterina, M.J., Schumacher, M.A., Tominaga, M., Rosen, T.A., Levine, J.D., and Julius, D. (1997). The capsaicin receptor: a heat-activated ion channel in the pain pathway. Nature *389*, 816-824. 10.1038/39807.

Chang, R.B., Strochlic, D.E., Williams, E.K., Umans, B.D., and Liberles, S.D. (2015). Vagal Sensory Neuron Subtypes that Differentially Control Breathing. Cell *161*, 622-633. 10.1016/j.cell.2015.03.022.

Coppola, E., Rallu, M., Richard, J., Dufour, S., Riethmacher, D., Guillemot, F., Goridis, C., and Brunet, J.F. (2010). Epibranchial ganglia orchestrate the development of the cranial neurogenic crest. Proc Natl Acad Sci U S A *107*, 2066-2071. 10.1073/pnas.0910213107.

Cordes, S.P. (2001). Molecular genetics of cranial nerve development in mouse. Nat Rev Neurosci *2*, 611-623. 10.1038/35090039.

Coste, B., Mathur, J., Schmidt, M., Earley, T.J., Ranade, S., Petrus, M.J., Dubin, A.E., and Patapoutian, A. (2010). Piezo1 and Piezo2 are essential components of distinct mechanically activated cation channels. Science *330*, 55-60. 10.1126/science.1193270.

Coverdell, T.C., Abraham-Fan, R.J., Wu, C., Abbott, S.B.G., and Campbell, J.N. (2022). Genetic encoding of an esophageal motor circuit. Cell Rep *39*, 110962. 10.1016/j.celrep.2022.110962.

Crist, J., Gidda, J.S., and Goyal, R.K. (1984). Characteristics of "on" and "off" contractions in esophageal circular muscle in vitro. Am J Physiol *246*, G137-144. 10.1152/ajpgi.1984.246.2.G137.

D'Amico-Martel, A., and Noden, D.M. (1983). Contributions of placodal and neural crest cells to avian cranial peripheral ganglia. Am J Anat *166*, 445-468. 10.1002/aja.1001660406.

D'Autreaux, F., Coppola, E., Hirsch, M.R., Birchmeier, C., and Brunet, J.F. (2011). Homeoprotein Phox2b commands a somatic-to-visceral switch in cranial sensory pathways. Proc Natl Acad Sci U S A *108*, 20018-20023. 10.1073/pnas.1110416108.

Daigle, T.L., Madisen, L., Hage, T.A., Valley, M.T., Knoblich, U., Larsen, R.S., Takeno, M.M., Huang, L., Gu, H., Larsen, R., et al. (2018). A Suite of Transgenic Driver and Reporter Mouse Lines with Enhanced Brain-Cell-Type Targeting and Functionality. Cell *174*, 465-480 e422. 10.1016/j.cell.2018.06.035.

Dempsey, B., Sungeelee, S., Bokiniec, P., Chettouh, Z., Diem, S., Autran, S., Harrell, E.R., Poulet, J.F.A., Birchmeier, C., Carey, H., et al. (2021). A medullary centre for lapping in mice. Nat Commun *12*, 6307. 10.1038/s41467-021-26275-y.

Dorsky, R.I., Moon, R.T., and Raible, D.W. (1998). Control of neural crest cell fate by the Wnt signalling pathway. Nature *396*, 370-373. 10.1038/24620.

Dvoryanchikov, G., Hernandez, D., Roebber, J.K., Hill, D.L., Roper, S.D., and Chaudhari, N. (2017). Transcriptomes and neurotransmitter profiles of classes of gustatory and somatosensory neurons in the geniculate ganglion. Nat Commun *8*, 760. 10.1038/s41467-017-01095-1.

Ertekin, C., and Aydogdu, I. (2003). Neurophysiology of swallowing. Clin Neurophysiol *114*, 2226-2244. 10.1016/s1388-2457(03)00237-2.

Espinosa-Medina, I., Jevans, B., Boismoreau, F., Chettouh, Z., Enomoto, H., Muller, T., Birchmeier, C., Burns, A.J., and Brunet, J.F. (2017). Dual origin of enteric neurons in vagal Schwann cell precursors and the sympathetic neural crest. Proc Natl Acad Sci U S A *114*, 11980-11985. 10.1073/pnas.1710308114.

Falempin, M., Madhloum, A., and Rousseau, J.P. (1986). Effects of vagal deafferentation on oesophageal motility and transit in the sheep. J Physiol *372*, 425-436. 10.1113/jphysiol.1986.sp016017.

Faure, L., Wang, Y., Kastriti, M.E., Fontanet, P., Cheung, K.K.Y., Petitpre, C., Wu, H., Sun, L.L., Runge, K., Croci, L., et al. (2020). Single cell RNA sequencing identifies early diversity of sensory neurons forming via bi-potential intermediates. Nat Commun *11*, 4175. 10.1038/s41467-020-17929-4.

Fode, C., Gradwohl, G., Morin, X., Dierich, A., LeMeur, M., Goridis, C., and Guillemot, F. (1998). The bHLH protein NEUROGENIN 2 is a determination factor for epibranchial placode-derived sensory neurons. Neuron *20*, 483-494. 10.1016/s0896-6273(00)80989-7.

Fontaine-Perus, J., Chanconie, M., and Le Douarin, N.M. (1988). Developmental potentialities in the nonneuronal population of quail sensory ganglia. Dev Biol *128*, 359-375. 10.1016/0012-1606(88)90298-9.

Fox, E.A., Phillips, R.J., Martinson, F.A., Baronowsky, E.A., and Powley, T.L. (2000). Vagal afferent innervation of smooth muscle in the stomach and duodenum of the mouse: morphology and topography. J Comp Neurol *428*, 558-576. 10.1002/1096-9861(20001218)428:3<558::aid-cne11>3.0.co;2-m.

Fox, E.A., Phillips, R.J., Martinson, F.A., Baronowsky, E.A., and Powley, T.L. (2001). C-Kit mutant mice have a selective loss of vagal intramuscular mechanoreceptors in the forestomach. Anat Embryol (Berl) *204*, 11-26. 10.1007/s004290100184.

Frazure, M.L., Brown, A.D., Greene, C.L., Iceman, K.E., and Pitts, T. (2021). Rapid activation of esophageal mechanoreceptors alters the pharyngeal phase of swallow: Evidence for inspiratory activity during swallow. PLoS One *16*, e0248994. 10.1371/journal.pone.0248994.

Garcia-Castro, M.I., Marcelle, C., and Bronner-Fraser, M. (2002). Ectodermal Wnt function as a neural crest inducer. Science *297*, 848-851. 10.1126/science.1070824.

Goyal, R.K., and Chaudhury, A. (2008). Physiology of normal esophageal motility. J Clin Gastroenterol *42*, 610-619. 10.1097/MCG.0b013e31816b444d.

Grover, M., Farrugia, G., and Stanghellini, V. (2019). Gastroparesis: a turning point in understanding and treatment. Gut *68*, 2238-2250. 10.1136/gutjnl-2019-318712.

Guthrie, S. (2007). Patterning and axon guidance of cranial motor neurons. Nat Rev Neurosci *8*, 859-871. 10.1038/nrn2254.

Han, W., and de Araujo, I.E. (2021). Dissection and surgical approaches to the mouse jugular-nodose ganglia. STAR Protoc *2*, 100474. 10.1016/j.xpro.2021.100474.

Haney, M.M., Sinnott, J., Osman, K.L., Deninger, I., Andel, E., Caywood, V., Mok, A., Ballenger, B., Cummings, K., Thombs, L., and Lever, T.E. (2019). Mice Lacking Brain-Derived Serotonin Have Altered Swallowing Function. Otolaryngol Head Neck Surg *161*, 468-471. 10.1177/0194599819846109.

Haque, A., Engel, J., Teichmann, S.A., and Lonnberg, T. (2017). A practical guide to single-cell RNA-sequencing for biomedical research and clinical applications. Genome Med *9*, 75. 10.1186/s13073-017-0467-4.

Haring, M., Fatt, M., and Kupari, J. (2020). Protocol to Prepare Single-Cell Suspensions from Mouse Vagal Sensory Ganglia for Transcriptomic Studies. STAR Protoc *1*, 100030. 10.1016/j.xpro.2020.100030.

Hashimshony, T., Senderovich, N., Avital, G., Klochendler, A., de Leeuw, Y., Anavy, L., Gennert, D., Li, S., Livak, K.J., Rozenblatt-Rosen, O., et al. (2016). CEL-Seq2: sensitive highly-multiplexed single-cell RNA-Seq. Genome Biol *17*, 77. 10.1186/s13059-016-0938-8.

Hasler, W.L. (2011). Gastroparesis: pathogenesis, diagnosis and management. Nat Rev Gastroenterol Hepatol *8*, 438-453. 10.1038/nrgastro.2011.116.

Hinkel, C.J., Sharma, R., Thakkar, M.M., Takahashi, K., Hopewell, B.L., and Lever, T.E. (2016). Neural Mechanisms Contributing to Dysphagia in Mouse Models. Otolaryngol Head Neck Surg *155*, 303-306. 10.1177/0194599816640261.

Horl, D., Rojas Rusak, F., Preusser, F., Tillberg, P., Randel, N., Chhetri, R.K., Cardona, A., Keller, P.J., Harz, H., Leonhardt, H., et al. (2019). BigStitcher: reconstructing high-resolution image datasets of cleared and expanded samples. Nat Methods *16*, 870-874. 10.1038/s41592-019-0501-0.

Ichikawa, H., De Repentigny, Y., Kothary, R., and Sugimoto, T. (2006). The survival of vagal and glossopharyngeal sensory neurons is dependent upon dystonin. Neuroscience *137*, 531-536. 10.1016/j.neuroscience.2005.08.081.

Iggo, A. (1955). Tension receptors in the stomach and the urinary bladder. J Physiol *128*, 593-607. 10.1113/jphysiol.1955.sp005327.

Ikeya, M., Lee, S.M., Johnson, J.E., McMahon, A.P., and Takada, S. (1997). Wnt signalling required for expansion of neural crest and CNS progenitors. Nature *389*, 966-970. 10.1038/40146.

Janig, W. (1996). Neurobiology of visceral afferent neurons: neuroanatomy, functions, organ regulations and sensations. Biol Psychol *42*, 29-51. 10.1016/0301-0511(95)05145-7.

Janssen, P., Vanden Berghe, P., Verschueren, S., Lehmann, A., Depoortere, I., and Tack, J. (2011). The role of gastric motility in the control of food intake. Aliment Pharmacol Ther *33*, 880-894. 10.1111/j.1365-2036.2011.04609.x.

Janssens, J., De Wever, I., Vantrappen, G., and Hellemans, J. (1976). Peristalsis in smooth muscle esophagus after transection and bolus deviation. Gastroenterology *71*, 1004-1009.

Jean, A. (1984). Brainstem organization of the swallowing network. Brain Behav Evol *25*, 109-116. 10.1159/000118856.

Jean, A. (2001). Brain stem control of swallowing: neuronal network and cellular mechanisms. Physiol Rev *81*, 929-969. 10.1152/physrev.2001.81.2.929.

Jessen, K.R., and Mirsky, R. (2005). The origin and development of glial cells in peripheral nerves. Nat Rev Neurosci *6*, 671-682. 10.1038/nrn1746.

Kaelberer, M.M., Buchanan, K.L., Klein, M.E., Barth, B.B., Montoya, M.M., Shen, X., and Bohorquez, D.V. (2018). A gut-brain neural circuit for nutrient sensory transduction. Science *361*. 10.1126/science.aat5236.

Kaelberer, M.M., Rupprecht, L.E., Liu, W.W., Weng, P., and Bohorquez, D.V. (2020). Neuropod Cells: The Emerging Biology of Gut-Brain Sensory Transduction. Annu Rev Neurosci *43*, 337-353. 10.1146/annurev-neuro-091619-022657.

Kahrilas, P.J., Bredenoord, A.J., Fox, M., Gyawali, C.P., Roman, S., Smout, A.J., Pandolfino, J.E., and International High Resolution Manometry Working, G. (2015). The Chicago Classification of esophageal motility disorders, v3.0. Neurogastroenterol Motil *27*, 160-174. 10.1111/nmo.12477.

Kandel, E.R., Schwartz, J.H., Jessel, T.M., Siegelbaum, S.A., and Hudspeth, A.J. (2013). Principles of neural science, 5th Edition (McGraw-Hill).

Kastriti, M.E., and Adameyko, I. (2017). Specification, plasticity and evolutionary origin of peripheral glial cells. Curr Opin Neurobiol *47*, 196-202. 10.1016/j.conb.2017.11.004.

Kim, D.Y., Heo, G., Kim, M., Kim, H., Jin, J.A., Kim, H.K., Jung, S., An, M., Ahn, B.H., Park, J.H., et al. (2020). A neural circuit mechanism for mechanosensory feedback control of ingestion. Nature *580*, 376-380. 10.1038/s41586-020-2167-2.

Kim, M., Heo, G., and Kim, S.Y. (2022). Neural signalling of gut mechanosensation in ingestive and digestive processes. Nat Rev Neurosci *23*, 135-156. 10.1038/s41583-021-00544-7.

Kloepper, A., Arnold, J., Ruffolo, A., Kinealy, B., Haxton, C., Nichols, N., Takahashi, K., and Lever, T.E. (2020). An Experimental Swallow Evoked Potential Protocol to Investigate the Neural Substrates of Swallowing. OTO Open *4*, 2473974X20913542. 10.1177/2473974X20913542.

Koch, S.C., Acton, D., and Goulding, M. (2018). Spinal Circuits for Touch, Pain, and Itch. Annu Rev Physiol *80*, 189-217. 10.1146/annurev-physiol-022516-034303.

Kronecker H., M.S. (1883). Der Schluckmechanismus, seine Erreggnung und seine Hemmung. Arch Anat Physiol. Physiol Abt, 328–360.

Kubin, L., Alheid, G.F., Zuperku, E.J., and McCrimmon, D.R. (2006). Central pathways of pulmonary and lower airway vagal afferents. J Appl Physiol (1985) *101*, 618-627. 10.1152/japplphysiol.00252.2006.

Kuhlbrodt, K., Herbarth, B., Sock, E., Hermans-Borgmeyer, I., and Wegner, M. (1998). Sox10, a novel transcriptional modulator in glial cells. J Neurosci *18*, 237-250.

Kulkarni, S., Micci, M.A., Leser, J., Shin, C., Tang, S.C., Fu, Y.Y., Liu, L., Li, Q., Saha, M., Li, C., et al. (2017). Adult enteric nervous system in health is maintained by a dynamic balance between neuronal apoptosis and neurogenesis. Proc Natl Acad Sci U S A *114*, E3709-E3718. 10.1073/pnas.1619406114.

Kupari, J., Haring, M., Agirre, E., Castelo-Branco, G., and Ernfors, P. (2019). An Atlas of Vagal Sensory Neurons and Their Molecular Specialization. Cell Rep *27*, 2508-2523 e2504. 10.1016/j.celrep.2019.04.096.

Kwong, K., Kollarik, M., Nassenstein, C., Ru, F., and Undem, B.J. (2008). P2X2 receptors differentiate placodal vs. neural crest C-fiber phenotypes innervating guinea pig lungs and esophagus. Am J Physiol Lung Cell Mol Physiol *295*, L858-865. 10.1152/ajplung.90360.2008.

Lang, I.M. (2009). Brain stem control of the phases of swallowing. Dysphagia *24*, 333-348. 10.1007/s00455-009-9211-6.

Lang, I.M., Medda, B.K., and Shaker, R. (2001). Mechanisms of reflexes induced by esophageal distension. Am J Physiol Gastrointest Liver Physiol *281*, G1246-1263. 10.1152/ajpgi.2001.281.5.G1246.

Lawrentjew, B.I. (1929). Experimentell-morphologische Studien uber den feineren Bau des autonomen Nervensystems. II. Uber den Aufbau der Ganglien der Speiserohre nebst einigen

Bemerkungen uber das Vorkommen und die Verteilung zweier Arten von Nervenzellen im autonomen Nervensystem. Z. Mikrosk. Anat. Forsch., 233-262.

Le Douarin, N.M. (1986). Cell line segregation during peripheral nervous system ontogeny. Science *231*, 1515-1522. 10.1126/science.3952494.

Lechner, S.G., and Lewin, G.R. (2009). Peripheral sensitisation of nociceptors via G-protein-dependent potentiation of mechanotransduction currents. J Physiol *587*, 3493-3503. 10.1113/jphysiol.2009.175059.

Lee, H.Y., Kleber, M., Hari, L., Brault, V., Suter, U., Taketo, M.M., Kemler, R., and Sommer, L. (2004). Instructive role of Wnt/beta-catenin in sensory fate specification in neural crest stem cells. Science *303*, 1020-1023. 10.1126/science.1091611.

Levanon, D., Bernstein, Y., Negreanu, V., Bone, K.R., Pozner, A., Eilam, R., Lotem, J., Brenner, O., and Groner, Y. (2011). Absence of Runx3 expression in normal gastrointestinal epithelium calls into question its tumour suppressor function. EMBO Mol Med *3*, 593-604. 10.1002/emmm.201100168.

Levanon, D., Bettoun, D., Harris-Cerruti, C., Woolf, E., Negreanu, V., Eilam, R., Bernstein, Y., Goldenberg, D., Xiao, C., Fliegauf, M., et al. (2002). The Runx3 transcription factor regulates development and survival of TrkC dorsal root ganglia neurons. EMBO J *21*, 3454-3463. 10.1093/emboj/cdf370.

Lever, T.E., Braun, S.M., Brooks, R.T., Harris, R.A., Littrell, L.L., Neff, R.M., Hinkel, C.J., Allen, M.J., and Ulsas, M.A. (2015). Adapting human videofluoroscopic swallow study methods to detect and characterize dysphagia in murine disease models. J Vis Exp. 10.3791/52319.

Li, C.L., Li, K.C., Wu, D., Chen, Y., Luo, H., Zhao, J.R., Wang, S.S., Sun, M.M., Lu, Y.J., Zhong, Y.Q., et al. (2016). Somatosensory neuron types identified by high-coverage single-cell RNA-sequencing and functional heterogeneity. Cell Res *26*, 967. 10.1038/cr.2016.90.

Li, H., Kentish, S.J., Wittert, G.A., and Page, A.J. (2018). Apelin modulates murine gastric vagal afferent mechanosensitivity. Physiol Behav *194*, 466-473. 10.1016/j.physbeh.2018.06.039.

Liu, Y., Diaz de Arce, A.J., and Krasnow, M.A. (2021). Molecular, anatomical, and functional organization of lung interoceptors. bioRxiv, 2021.2011.2010.468116. 10.1101/2021.11.10.468116.

Ma, Q., Chen, Z., del Barco Barrantes, I., de la Pompa, J.L., and Anderson, D.J. (1998). neurogenin1 is essential for the determination of neuronal precursors for proximal cranial sensory ganglia. Neuron *20*, 469-482. 10.1016/s0896-6273(00)80988-5.

Madisen, L., Garner, A.R., Shimaoka, D., Chuong, A.S., Klapoetke, N.C., Li, L., van der Bourg, A., Niino, Y., Egolf, L., Monetti, C., et al. (2015). Transgenic mice for intersectional targeting of neural sensors and effectors with high specificity and performance. Neuron *85*, 942-958. 10.1016/j.neuron.2015.02.022.

Madisen, L., Zwingman, T.A., Sunkin, S.M., Oh, S.W., Zariwala, H.A., Gu, H., Ng, L.L., Palmiter, R.D., Hawrylycz, M.J., Jones, A.R., et al. (2010). A robust and high-throughput Cre reporting and characterization system for the whole mouse brain. Nat Neurosci *13*, 133-140. 10.1038/nn.2467.

Martin-Harris, B., and Jones, B. (2008). The videofluorographic swallowing study. Phys Med Rehabil Clin N Am *19*, 769-785, viii. 10.1016/j.pmr.2008.06.004.

Mazzone, S.B., and Undem, B.J. (2016). Vagal Afferent Innervation of the Airways in Health and Disease. Physiol Rev *96*, 975-1024. 10.1152/physrev.00039.2015.

McCoy, M.E., and Kamitakahara, A.K. (2022). Ontogeny and Trophic Factor Sensitivity of Gastrointestinal Projecting Vagal Sensory Cell Types. bioRxiv, 2022.2007.2004.498754. 10.1101/2022.07.04.498754.

Mercado-Perez, A., and Beyder, A. (2022). Gut feelings: mechanosensing in the gastrointestinal tract. Nat Rev Gastroenterol Hepatol *19*, 283-296. 10.1038/s41575-021-00561-y.

Min, S., Chang, R.B., Prescott, S.L., Beeler, B., Joshi, N.R., Strochlic, D.E., and Liberles, S.D. (2019). Arterial Baroreceptors Sense Blood Pressure through Decorated Aortic Claws. Cell Rep *29*, 2192-2201 e2193. 10.1016/j.celrep.2019.10.040.

Miolan, J.P., and Niel, J.P. (1996). The mammalian sympathetic prevertebral ganglia: integrative properties and role in the nervous control of digestive tract motility. J Auton Nerv Syst *58*, 125-138. 10.1016/0165-1838(95)00128-x.

Morin, X., Cremer, H., Hirsch, M.R., Kapur, R.P., Goridis, C., and Brunet, J.F. (1997). Defects in sensory and autonomic ganglia and absence of locus coeruleus in mice deficient for the homeobox gene Phox2a. Neuron *18*, 411-423. 10.1016/s0896-6273(00)81242-8.

Mueller, M., Thompson, R., Osman, K.L., Andel, E., DeJonge, C.A., Kington, S., Stephenson, Z., Hamad, A., Bunyak, F., Nichols, N.L., and Lever, T.E. (2022). Impact of Limb Phenotype on Tongue Denervation Atrophy, Dysphagia Penetrance, and Survival Time in a Mouse Model of ALS. Dysphagia. 10.1007/s00455-022-10442-4.

Muller, M., Jabs, N., Lorke, D.E., Fritzsch, B., and Sander, M. (2003). Nkx6.1 controls migration and axon pathfinding of cranial branchio-motoneurons. Development *130*, 5815-5826. 10.1242/dev.00815.

Murray, J., Du, C., Ledlow, A., Bates, J.N., and Conklin, J.L. (1991). Nitric oxide: mediator of nonadrenergic noncholinergic responses of opossum esophageal muscle. Am J Physiol *261*, G401-406. 10.1152/ajpgi.1991.261.3.G401.

Murthy, S.E., Dubin, A.E., and Patapoutian, A. (2017). Piezos thrive under pressure: mechanically activated ion channels in health and disease. Nat Rev Mol Cell Biol *18*, 771-783. 10.1038/nrm.2017.92.

Murthy, S.E., Loud, M.C., Daou, I., Marshall, K.L., Schwaller, F., Kuhnemund, J., Francisco, A.G., Keenan, W.T., Dubin, A.E., Lewin, G.R., and Patapoutian, A. (2018). The mechanosensitive ion channel Piezo2 mediates sensitivity to mechanical pain in mice. Sci Transl Med *10*. 10.1126/scitranslmed.aat9897.

Narayanan, C.H., and Narayanan, Y. (1980). Neural crest and placodal contributions in the development of the glossopharyngeal-vagal complex in the chick. Anat Rec *196*, 71-82. 10.1002/ar.1091960108.

Neuhuber, W.L. (1987). Sensory vagal innervation of the rat esophagus and cardia: a light and electron microscopic anterograde tracing study. J Auton Nerv Syst *20*, 243-255. 10.1016/0165-1838(87)90153-6.

Neuhuber, W.L., Raab, M., Berthoud, H.R., and Worl, J. (2006). Innervation of the mammalian esophagus. Adv Anat Embryol Cell Biol *185*, 1-73, back cover.

Nishijima, I., and Ohtoshi, A. (2006). Characterization of a novel prospero-related homeobox gene, Prox2. Mol Genet Genomics *275*, 471-478. 10.1007/s00438-006-0105-0.

Niu, X., Liu, L., Wang, T., Chuan, X., Yu, Q., Du, M., Gu, Y., and Wang, L. (2020). Mapping of Extrinsic Innervation of the Gastrointestinal Tract in the Mouse Embryo. J Neurosci *40*, 6691-6708. 10.1523/JNEUROSCI.0309-20.2020.

Nonidez, J.F. (1946). Afferent nerve endings in the ganglia of the intermuscular plexus of the dog's oesophagus. J Comp Neurol *85*, 177-189. 10.1002/cne.900850204.

Nonomura, K., Woo, S.H., Chang, R.B., Gillich, A., Qiu, Z., Francisco, A.G., Ranade, S.S., Liberles, S.D., and Patapoutian, A. (2017). Piezo2 senses airway stretch and mediates lung inflation-induced apnoea. Nature *541*, 176-181. 10.1038/nature20793.

Ora, M., Nazar, A.H., Parashar, A., Kheruka, S., and Gambhir, S. (2019). Gastric Emptying Scintigraphy: Beyond Numbers - An Observational Study to Differentiate between Various Etiologies and a Step toward Personalized Management. Indian J Nucl Med *34*, 194-200. 10.4103/ijnm.IJNM_55_19.

Page, A.J., and Blackshaw, L.A. (1998). An in vitro study of the properties of vagal afferent fibres innervating the ferret oesophagus and stomach. J Physiol *512 (Pt 3)*, 907-916. 10.1111/j.1469-7793.1998.907bd.x.

Page, A.J., Brierley, S.M., Martin, C.M., Martinez-Salgado, C., Wemmie, J.A., Brennan, T.J., Symonds, E., Omari, T., Lewin, G.R., Welsh, M.J., and Blackshaw, L.A. (2004). The ion channel ASIC1 contributes to visceral but not cutaneous mechanoreceptor function. Gastroenterology *127*, 1739-1747. 10.1053/j.gastro.2004.08.061.

Page, A.J., Brierley, S.M., Martin, C.M., Price, M.P., Symonds, E., Butler, R., Wemmie, J.A., and Blackshaw, L.A. (2005). Different contributions of ASIC channels 1a, 2, and 3 in gastrointestinal mechanosensory function. Gut *54*, 1408-1415. 10.1136/gut.2005.071084.

Page, A.J., Martin, C.M., and Blackshaw, L.A. (2002). Vagal mechanoreceptors and chemoreceptors in mouse stomach and esophagus. J Neurophysiol *87*, 2095-2103. 10.1152/jn.00785.2001.

Paintal, A.S. (1954). The response of gastric stretch receptors and certain other abdominal and thoracic vagal receptors to some drugs. J Physiol *126*, 271-285. 10.1113/jphysiol.1954.sp005208.

Pattyn, A., Hirsch, M., Goridis, C., and Brunet, J.F. (2000). Control of hindbrain motor neuron differentiation by the homeobox gene Phox2b. Development *127*, 1349-1358. 10.1242/dev.127.7.1349.

Pattyn, A., Morin, X., Cremer, H., Goridis, C., and Brunet, J.F. (1997). Expression and interactions of the two closely related homeobox genes Phox2a and Phox2b during neurogenesis. Development *124*, 4065-4075. 10.1242/dev.124.20.4065.

Pattyn, A., Morin, X., Cremer, H., Goridis, C., and Brunet, J.F. (1999). The homeobox gene Phox2b is essential for the development of autonomic neural crest derivatives. Nature *399*, 366-370. 10.1038/20700.

Phillips, R.J., and Powley, T.L. (2000). Tension and stretch receptors in gastrointestinal smooth muscle: re-evaluating vagal mechanoreceptor electrophysiology. Brain Res Brain Res Rev *34*, 1-26. 10.1016/s0165-0173(00)00036-9.

Powley, T.L. (2021). Brain-gut communication: vagovagal reflexes interconnect the two "brains". Am J Physiol Gastrointest Liver Physiol *321*, G576-G587. 10.1152/ajpgi.00214.2021.

Powley, T.L., Hudson, C.N., McAdams, J.L., Baronowsky, E.A., Martin, F.N., Mason, J.K., and Phillips, R.J. (2014). Organization of vagal afferents in pylorus: mechanoreceptors arrayed for high sensitivity and fine spatial resolution? Auton Neurosci *183*, 36-48. 10.1016/j.autneu.2014.02.008.

Powley, T.L., Hudson, C.N., McAdams, J.L., Baronowsky, E.A., and Phillips, R.J. (2016). Vagal Intramuscular Arrays: The Specialized Mechanoreceptor Arbors That Innervate the Smooth Muscle Layers of the Stomach Examined in the Rat. J Comp Neurol *524*, 713-737. 10.1002/cne.23892.

Powley, T.L., Jaffey, D.M., McAdams, J., Baronowsky, E.A., Black, D., Chesney, L., Evans, C., and Phillips, R.J. (2019). Vagal innervation of the stomach reassessed: brain-gut connectome uses smart terminals. Ann N Y Acad Sci *1454*, 14-30. 10.1111/nyas.14138.

Powley, T.L., and Phillips, R.J. (2011). Vagal intramuscular array afferents form complexes with interstitial cells of Cajal in gastrointestinal smooth muscle: analogues of muscle spindle organs? Neuroscience *186*, 188-200. 10.1016/j.neuroscience.2011.04.036.

Powley, T.L., Wang, X.Y., Fox, E.A., Phillips, R.J., Liu, L.W., and Huizinga, J.D. (2008). Ultrastructural evidence for communication between intramuscular vagal mechanoreceptors and interstitial cells of Cajal in the rat fundus. Neurogastroenterol Motil *20*, 69-79. 10.1111/j.1365-2982.2007.00990.x.

Prechtl, J.C., and Powley, T.L. (1990). The fiber composition of the abdominal vagus of the rat. Anat Embryol (Berl) *181*, 101-115. 10.1007/BF00198950.

Prescott, S.L., and Liberles, S.D. (2022). Internal senses of the vagus nerve. Neuron *110*, 579-599. 10.1016/j.neuron.2021.12.020.

Prescott, S.L., Umans, B.D., Williams, E.K., Brust, R.D., and Liberles, S.D. (2020). An Airway Protection Program Revealed by Sweeping Genetic Control of Vagal Afferents. Cell *181*, 574-589 e514. 10.1016/j.cell.2020.03.004.

Raab, M., and Neuhuber, W.L. (2003). Vesicular glutamate transporter 2 immunoreactivity in putative vagal mechanosensor terminals of mouse and rat esophagus: indication of a local effector function? Cell Tissue Res *312*, 141-148. 10.1007/s00441-003-0721-5.

Raab, M., and Neuhuber, W.L. (2007). Glutamatergic functions of primary afferent neurons with special emphasis on vagal afferents. Int Rev Cytol *256*, 223-275. 10.1016/S0074-7696(07)56007-9.

Ranade, S.S., Syeda, R., and Patapoutian, A. (2015). Mechanically Activated Ion Channels. Neuron *87*, 1162-1179. 10.1016/j.neuron.2015.08.032.

Ranade, S.S., Woo, S.H., Dubin, A.E., Moshourab, R.A., Wetzel, C., Petrus, M., Mathur, J., Begay, V., Coste, B., Mainquist, J., et al. (2014). Piezo2 is the major transducer of mechanical forces for touch sensation in mice. Nature *516*, 121-125. 10.1038/nature13980.

Rao, M.S., and Jacobson, M. (2005). Developmental Neurobiology, 4 Edition (Springer US).

Ratcliffe, E.M., Fan, L., Mohammed, T.J., Anderson, M., Chalazonitis, A., and Gershon, M.D. (2011a). Enteric neurons synthesize netrins and are essential for the development of the vagal sensory innervation of the fetal gut. Dev Neurobiol *71*, 362-373. 10.1002/dneu.20869.

Ratcliffe, E.M., Farrar, N.R., and Fox, E.A. (2011b). Development of the vagal innervation of the gut: steering the wandering nerve. Neurogastroenterol Motil *23*, 898-911. 10.1111/j.1365-2982.2011.01764.x.

Ratcliffe, E.M., Setru, S.U., Chen, J.J., Li, Z.S., D'Autreaux, F., and Gershon, M.D. (2006). Netrin/DCC-mediated attraction of vagal sensory axons to the fetal mouse gut. J Comp Neurol *498*, 567-580. 10.1002/cne.21027.

Rinaman, L. (2010). Ascending projections from the caudal visceral nucleus of the solitary tract to brain regions involved in food intake and energy expenditure. Brain Res *1350*, 18-34. 10.1016/j.brainres.2010.03.059.

Rodrigo, J., de Felipe, J., Robles-Chillida, E.M., Perez Anton, J.A., Mayo, I., and Gomez, A. (1982). Sensory vagal nature and anatomical access paths to esophagus laminar nerve endings in myenteric ganglia. Determination by surgical degeneration methods. Acta Anat (Basel) *112*, 47-57. 10.1159/000145496.

Rodrigo, J., Hernandez, J., Vidal, M.A., and Pedrosa, J.A. (1975). Vegetative innervation of the esophagus. II. Intraganglionic laminar endings. Acta Anat (Basel) *92*, 79-100. 10.1159/000144431.

Sanders, K.M., Koh, S.D., and Ward, S.M. (2006). Interstitial cells of cajal as pacemakers in the gastrointestinal tract. Annu Rev Physiol *68*, 307-343. 10.1146/annurev.physiol.68.040504.094718.

Sanders, K.M., and Ward, S.M. (2006). Interstitial cells of Cajal: a new perspective on smooth muscle function. J Physiol *576*, 721-726. 10.1113/jphysiol.2006.115279.

Schlosser, G. (2006). Induction and specification of cranial placodes. Dev Biol *294*, 303-351. 10.1016/j.ydbio.2006.03.009.

Shin, B., Hosokawa, H., Romero-Wolf, M., Zhou, W., Masuhara, K., Tobin, V.R., Levanon, D., Groner, Y., and Rothenberg, E.V. (2021). Runx1 and Runx3 drive progenitor to T-lineage transcriptome conversion in mouse T cell commitment via dynamic genomic site switching. Proc Natl Acad Sci U S A *118*. 10.1073/pnas.2019655118.

Slattery, J.A., Page, A.J., Dorian, C.L., Brierley, S.M., and Blackshaw, L.A. (2006). Potentiation of mouse vagal afferent mechanosensitivity by ionotropic and metabotropic glutamate receptors. J Physiol *577*, 295-306. 10.1113/jphysiol.2006.117762.

Soldatov, R., Kaucka, M., Kastriti, M.E., Petersen, J., Chontorotzea, T., Englmaier, L., Akkuratova, N., Yang, Y., Haring, M., Dyachuk, V., et al. (2019). Spatiotemporal structure of cell fate decisions in murine neural crest. Science *364*. 10.1126/science.aas9536.

Spencer, N.J., and Hu, H. (2020). Enteric nervous system: sensory transduction, neural circuits and gastrointestinal motility. Nat Rev Gastroenterol Hepatol *17*, 338-351. 10.1038/s41575-020-0271-2.

Steuernagel, L., Lam, B.Y.H., Klemm, P., Dowsett, G.K.C., Bauder, C.A., Tadross, J.A., Hitschfeld, T.S., Del Rio Martin, A., Chen, W., de Solis, A.J., et al. (2022). HypoMap-a unified single-cell gene expression atlas of the murine hypothalamus. Nat Metab *4*, 1402-1419. 10.1038/s42255-022-00657-y.

Stoeckel, K., Schwab, M., and Thoenen, H. (1977). Role of gangliosides in the uptake and retrograde axonal transport of cholera and tetanus toxin as compared to nerve growth factor and wheat germ agglutinin. Brain Res *132*, 273-285. 10.1016/0006-8993(77)90421-8.

Stuart, T., Butler, A., Hoffman, P., Hafemeister, C., Papalexi, E., Mauck, W.M., 3rd, Hao, Y., Stoeckius, M., Smibert, P., and Satija, R. (2019). Comprehensive Integration of Single-Cell Data. Cell *177*, 1888-1902 e1821. 10.1016/j.cell.2019.05.031.

Susaki, E.A., Tainaka, K., Perrin, D., Yukinaga, H., Kuno, A., and Ueda, H.R. (2015). Advanced CUBIC protocols for whole-brain and whole-body clearing and imaging. Nat Protoc *10*, 1709-1727. 10.1038/nprot.2015.085.

Suttrup, I., and Warnecke, T. (2016). Dysphagia in Parkinson's Disease. Dysphagia *31*, 24-32. 10.1007/s00455-015-9671-9.

Tassicker, B.C., Hennig, G.W., Costa, M., and Brookes, S.J. (1999). Rapid anterograde and retrograde tracing from mesenteric nerve trunks to the guinea-pig small intestine in vitro. Cell Tissue Res *295*, 437-452. 10.1007/s004410051250.

Travagli, R.A., and Anselmi, L. (2016). Vagal neurocircuitry and its influence on gastric motility. Nat Rev Gastroenterol Hepatol *13*, 389-401. 10.1038/nrgastro.2016.76.

Travagli, R.A., Hermann, G.E., Browning, K.N., and Rogers, R.C. (2006). Brainstem circuits regulating gastric function. Annu Rev Physiol *68*, 279-305. 10.1146/annurev.physiol.68.040504.094635.

Uesaka, T., Young, H.M., Pachnis, V., and Enomoto, H. (2016). Development of the intrinsic and extrinsic innervation of the gut. Dev Biol *417*, 158-167. 10.1016/j.ydbio.2016.04.016.

Umans, B.D., and Liberles, S.D. (2018). Neural Sensing of Organ Volume. Trends Neurosci *41*, 911-924. 10.1016/j.tins.2018.07.008.

Undem, B.J., and Weinreich, D. (2005). Advances in Vagal Afferent Neurobiology (Taylor & Francis).

Usoskin, D., Furlan, A., Islam, S., Abdo, H., Lonnerberg, P., Lou, D., Hjerling-Leffler, J., Haeggstrom, J., Kharchenko, O., Kharchenko, P.V., et al. (2015). Unbiased classification of sensory neuron types by large-scale single-cell RNA sequencing. Nat Neurosci *18*, 145-153. 10.1038/nn.3881.

Vermeiren, S., Bellefroid, E.J., and Desiderio, S. (2020). Vertebrate Sensory Ganglia: Common and Divergent Features of the Transcriptional Programs Generating Their Functional Specialization. Front Cell Dev Biol *8*, 587699. 10.3389/fcell.2020.587699.

Voigt, F.F., Kirschenbaum, D., Platonova, E., Pages, S., Campbell, R.A.A., Kastli, R., Schaettin, M., Egolf, L., van der Bourg, A., Bethge, P., et al. (2019). The mesoSPIM initiative: open-source light-sheet microscopes for imaging cleared tissue. Nat Methods *16*, 1105-1108. 10.1038/s41592-019-0554-0.

Vong, L., Ye, C., Yang, Z., Choi, B., Chua, S., Jr., and Lowell, B.B. (2011). Leptin action on GABAergic neurons prevents obesity and reduces inhibitory tone to POMC neurons. Neuron *71*, 142-154. 10.1016/j.neuron.2011.05.028.

Waise, T.M.Z., Dranse, H.J., and Lam, T.K.T. (2018). The metabolic role of vagal afferent innervation. Nat Rev Gastroenterol Hepatol *15*, 625-636. 10.1038/s41575-018-0062-1.

Wang, J.C., Crosson, T., and Talbot, S. (2022). Analysis of Airway Vagal Neurons. Methods Mol Biol *2506*, 297-314. 10.1007/978-1-0716-2364-0_21.

Wang, Y.B., de Lartigue, G., and Page, A.J. (2020). Dissecting the Role of Subtypes of Gastrointestinal Vagal Afferents. Front Physiol *11*, 643. 10.3389/fphys.2020.00643.

Wank, M., and Neuhuber, W.L. (2001). Local differences in vagal afferent innervation of the rat esophagus are reflected by neurochemical differences at the level of the sensory ganglia and by different brainstem projections. J Comp Neurol *435*, 41-59. 10.1002/cne.1192.

Wefers, B., Bashir, S., Rossius, J., Wurst, W., and Kuhn, R. (2017). Gene editing in mouse zygotes using the CRISPR/Cas9 system. Methods *121-122*, 55-67. 10.1016/j.ymeth.2017.02.008.

Welby, L., Caudill, H., Yitsege, G., Hamad, A., Bunyak, F., Zohn, I.E., Maynard, T., LaMantia, A.S., Mendelowitz, D., and Lever, T.E. (2020). Persistent Feeding and Swallowing Deficits in a Mouse Model of 22q11.2 Deletion Syndrome. Front Neurol *11*, 4. 10.3389/fneur.2020.00004.

Williams, E.K., Chang, R.B., Strochlic, D.E., Umans, B.D., Lowell, B.B., and Liberles, S.D. (2016). Sensory Neurons that Detect Stretch and Nutrients in the Digestive System. Cell *166*, 209-221. 10.1016/j.cell.2016.05.011.

Woo, S.H., Ranade, S., Weyer, A.D., Dubin, A.E., Baba, Y., Qiu, Z., Petrus, M., Miyamoto, T., Reddy, K., Lumpkin, E.A., et al. (2014). Piezo2 is required for Merkel-cell mechanotransduction. Nature *509*, 622-626. 10.1038/nature13251.

Young, R.L., Page, A.J., O'Donnell, T.A., Cooper, N.J., and Blackshaw, L.A. (2007). Peripheral versus central modulation of gastric vagal pathways by metabotropic glutamate receptor 5. Am J Physiol Gastrointest Liver Physiol *292*, G501-511. 10.1152/ajpgi.00353.2006.

Zagorodnyuk, V.P., and Brookes, S.J. (2000). Transduction sites of vagal mechanoreceptors in the guinea pig esophagus. J Neurosci *20*, 6249-6255.

Zagorodnyuk, V.P., Chen, B.N., and Brookes, S.J. (2001). Intraganglionic laminar endings are mechano-transduction sites of vagal tension receptors in the guinea-pig stomach. J Physiol *534*, 255-268. 10.1111/j.1469-7793.2001.00255.x.

Zagorodnyuk, V.P., Chen, B.N., Costa, M., and Brookes, S.J. (2003). Mechanotransduction by intraganglionic laminar endings of vagal tension receptors in the guinea-pig oesophagus. J Physiol *553*, 575-587. 10.1113/jphysiol.2003.051862.

Zaidi, F.N., and Whitehead, M.C. (2006). Discrete innervation of murine taste buds by peripheral taste neurons. J Neurosci *26*, 8243-8253. 10.1523/JNEUROSCI.5142-05.2006.

Zeisel, A., Hochgerner, H., Lonnerberg, P., Johnsson, A., Memic, F., van der Zwan, J., Haring, M., Braun, E., Borm, L.E., La Manno, G., et al. (2018). Molecular Architecture of the Mouse Nervous System. Cell *174*, 999-1014 e1022. 10.1016/j.cell.2018.06.021.

Zeng, W.Z., Marshall, K.L., Min, S., Daou, I., Chapleau, M.W., Abboud, F.M., Liberles, S.D., and Patapoutian, A. (2018). PIEZOs mediate neuronal sensing of blood pressure and the baroreceptor reflex. Science *362*, 464-467. 10.1126/science.aau6324.

Zhao, Q., Yu, C.D., Wang, R., Xu, Q.J., Dai Pra, R., Zhang, L., and Chang, R.B. (2022). A multidimensional coding architecture of the vagal interoceptive system. Nature *603*, 878-884. 10.1038/s41586-022-04515-5.

Zheng, H., Lauve, A., Patterson, L.M., and Berthoud, H.R. (1997). Limited excitatory local effector function of gastric vagal afferent intraganglionic terminals in rats. Am J Physiol *273*, G661-669. 10.1152/ajpgi.1997.273.3.G661.

Zou, D., Silvius, D., Fritzsch, B., and Xu, P.X. (2004). Eya1 and Six1 are essential for early steps of sensory neurogenesis in mammalian cranial placodes. Development *131*, 5561-5572. 10.1242/dev.01437.

8. Appendix

8.1. Table 1. Recombination sites of Prox2/Runx3 neurons.

Location	Ganglia	Mouse line	Recombined neurons
Hindbrain	locus coeruleus	*Prox2/Runx3^{Tom}*	0/1983 neurons, n=3
		Runx3^{Tom}	0/2791 neurons, n=3
	Nucleus ambiguus	*Prox2/Runx3^{Tom}*	0/592 neurons, n=3
		Runx3^{Tom}	0/377 neurons, n=3
	Dorsal motor nucleus of the vagus	*Prox2/Runx3^{Tom}*	0/2114 neurons, n=3
		Runx3^{Tom}	0/2554 neurons, n=3
Upper digestive tract	Esophagus enteric ganglia	*Prox2/Runx3^{Tom}*	0/419 neurons, n=3
		Runx3^{Tom}	0/276 neurons, n=3
	Stomach enteric ganglia	*Prox2/Runx3^{Tom}*	0/3462 neurons, n=3
		Runx3^{Tom}	0/3199 neurons, n=3
Sympathetic ganglia	Celiac ganglion	*Prox2/Runx3^{Tom}*	613/4098 neurons, n=3
		Runx3^{Tom}	8/4132 neurons, n=3
	Superior cervical ganglia	*Prox2/Runx3^{Tom}*	1/4474 neurons, n=3
		Runx3^{Tom}	4/6534 neurons, n=3
	Stellate ganglia	*Prox2/Runx3^{Tom}*	4/3015 neurons, n=3
		Runx3^{Tom}	5/6567 neurons, n=3
	Sympathetic chain ganglia	*Prox2/Runx3^{Tom}*	3/2436 neurons, n=3
		Runx3^{Tom}	1/4341 neurons, n=3
Spinal afferents	Dorsal root ganglia	*Prox2/Runx3^{Tom}*	0/17049 neurons, n=3
		Runx3^{Tom}	191/14092 neurons, n=3
Other	Geniculate ganglia	*Prox2/Runx3^{Tom}*	238/1588 neurons, n=3
		Runx3^{Tom}	56/1342 neurons, n=3

Neurons in the hindbrain, enteric ganglia in the upper digestive tract, sympathetic, geniculate and dorsal root ganglia were analyzed for recombination by analyzing tdTomato expression in both *Prox2/Runx3^{Tom}* and *Runx3^{Tom}* animals. Indicated are the locations/ganglia examined, the mouse lines used, and the total number of recombined neurons counted across 3 animals.

8.2. Table 2. Innervation targets of Prox2/Runx3 neurons.

Ganglion	Target	cell type	Subtype	Marker genes	Reference
Vagal	Esophagus	Enteric ganglia	MM2	*Prox2+, Piezo2+, Grm5+, Glp1r-*	This work.
	Stomach (non-glandular)	Enteric Ganglia	MM1	*Prox2+, Piezo2+, Glp1r+, Rbp4+, Gata3-*	This work; Williams et al., 2016.
	Stomach (glandular)	Enteric ganglia	MM8	*Runx3+, Prox2^{low}, Piezo2+, Glp1r+, Adra2a+*	This work; Williams et al., 2016.
	Larynx	Quadrangular membrane, mucosa, laryngeal taste buds	MM5	*Runx3+, Slc18a3+, Pappa2+, P2ry1+, Piezo2-*	Prescott et al., 2020.
	Lung	Bronchi smooth muscle	MM10	*Piezo2+, Lmcd1+, Sntg2+, Car2+, Slc17a7+*	Liu et al., 2021.
		Neuroepithelial bodies	MM9	*Piezo2+, Calb1+, Asic3+, Mafb+*	Liu et al., 2021.
	Heart	Aortic arch; Aorta	?	*Mc4r+, Agtr1a+*	Min et al., 2019; Zhao et al., 2022.
Geniculate	Tongue	Taste buds	---	---	---
Celiac	Intestine	---	---	---	---

Prox2/Runx3 neurons originating in the vagal, geniculate and celiac ganglia innervate the indicated target organs and cell types/tissue. Listed are the names of vagal neuron subtype (for the nomenclature see Figure 9) and genes used here as markers to identify the subtypes. Previous work that characterized the vagal neuronal subtypes in depth are indicated in the references.

8.3. List of publications

Lowenstein ED, Misios A, Ruffault PL, Birchmeier C. Molecular characterization of nodose ganglia development reveals a novel population of Phox2b+ glial progenitors. *In preparation*.

Lowenstein ED, Ruffault PL, Misios A, Osman KL, Li H, Thompson R, Song K, Dietrich S, Li X, Vladimirov N, Brunet JF, Woehler A, Zampieri N, Kühn R, Jia S, Lewin GR, Rajewsky N, Lever T, Birchmeier C. Prox2+ and Runx3+ Neurons Regulate Esophageal Motility. *In revision*.

Xia Y, Cui K, Alonso A, Lowenstein ED, Hernandez-Miranda LR. Transcription factors regulating the specification of brainstem respiratory neurons. Front. Mol. Neurosci. 2022 Nov 29.

Dietrich S, Company C, Song K, Lowenstein ED, Riedel L, Birchmeier C, Gargiulo G, Zampieri N. Molecular identity of proprioceptor subtypes innervating different muscle groups in mice. Nat Commun. 2022 Nov 11;13(1):6867.

Pelz L, Dossou L, Kompier N, Jüttner R, Siemonsmeier G, Meyer N, Lowenstein ED, Lahmann I, Ketternmann H, Birchmeier C, Rathjen FG. The IgCAM BT-IgSF (IgSF11) is essential for connexin43-mediated astrocyte-astrocyte and ependymal cell-cell coupling. Biorxiv. 2022 June.

Lowenstein ED, Cui K, Hernandez-Miranda LR. Regulation of early cerebellar development. FEBS J. 2022 Mar 9. doi: 10.1111/febs.16426.

Lowenstein ED*, Rusanova A*, Stelzer J, Hernaiz-Llorens M, Schroer AE, Epifanova E, Bladt F, Isik EG, Buchert S, Jia S, Tarabykin V, Hernandez-Miranda LR. Olig3 regulates early cerebellar development. Elife. 2021 Feb 16;10:e64684.
*Denotes co-first authors.

Kim M, Franke V, Brandt B, Lowenstein ED, Schöwel V, Spuler S, Akalin A, Birchmeier C. Single-nucleus transcriptomics reveals functional compartmentalization in syncytial skeletal muscle cells. Nat Commun. 2020 Dec 11;11(1):6375.

Fitzpatrick CJ, Jagannathan L, Lowenstein ED, Robinson TE, Becker JB, Morrow JD. Single prolonged stress decreases sign-tracking and cue-induced reinstatement of cocaine-seeking. Behav Brain Res. 2019 Feb 1;359:799-806.

Lowenstein ED. “Diversity in the lab makes me a better scientist.” *Scientific American* January 2019: 8. Print.

Xiong J, Jiang X, Ditsiou A, Gao Y, Sun J, Lowenstein ED, Huang S, Khaitovich P. Predominant patterns of splicing evolution on human, chimpanzee and macaque evolutionary lineages. Hum Mol Genet. 2018 Apr 15;27(8):1474-1485

Lowenstein ED. “I love preprints.” *Scientific American Blog*, Springer Nature, 18 March 2018, https://blogs.scientificamerican.com/observations/i-love-preprints/.